INTERFACIAL COUPLING BETWEEN IMMISCIBLE POLYMERS: FLOW ACCELERATES REACTION AND IMPROVES ADHESION

A DISSERTATION
SUBMITTED TO THE FACULTY OF THE GRADUATE SCHOOL
OF THE UNIVERSITY OF MINNESOTA
BY

JIE SONG

IN PARTIAL FULFILLMENT OF THE REQUIREMENTS
FOR THE DEGREE OF
DOCTOR OF PHILOSOPHY

CHRISTOPHER W. MACOSKO

OCTOBER 2011

Acknowledgements

I am truly grateful to numerous people who have helped and encouraged me for my doctoral study at the University of Minnesota.

First of all, I want to express my sincere gratitude to my advisor Professor Chris Macosko for his guidance and support over the years. I am fortunate and proud to be a member of his research group. He offered me all the possible opportunities and freedom to learn and grow. He has always been a great example of passionate and inspiring person to me. I would also like to thank Professor Timothy Lodge, Professor David Morse and Professor Marc Hillmyer for reviewing my thesis work and becoming thesis defense committee members.

I am indebted to many colleagues that I have met during my stay at the University of Minnesota. Dr. David Giles has helped me with rheometry and other polymer characterization techniques. Former group members Dr. Patrick Lee, Dr. Ling Zhang and Dr. Hyunwoo Kim trained me on polymer processing and related principles. Former post doctor Dr. Shingo Kobayashi was a great synthetic chemistry teacher. The discussions with Dr. Randy Ewoldt are always inspiring and cheerful. Many staff members in the University of Minnesota Characterization Facility have made their expertise an extraordinary asset to me.

This thesis would not be possible without financial supports from The Dow Chemical Company and the University Doctoral Dissertation Fellowship. My interactions with the scientists and engineers from Dow has been a truly pleasure. I am grateful for the continuous support from Dr. Craig Silvis, Dr. Ashish Batra and Dr. Manu Rego.

It was a great pleasure for me to spend last five years with wonderful friends in this department. Spending time with former and current group members Carlos Lopez-Barron, Zhengxi Zhu, Dawud Tan, Suqin Tan, Chris Thurber, Aaron Hedegaard, Jing Han, Yuqiang Qian, Luca Martinetti, Milana Trifkovic, Kirby Liao, Zaifei Wang, and Issam Ismail made my lab life very enjoyable. I found working with three hard-working undergraduate students (Josh Kube, Wanli Hu and Adam Baker) very valuable experience. I also enjoyed sharing the office with other polymer group members. I should

not forget delivering my appreciation to helpful administrative staff in the department of chemical engineering and materials science.

I would also like to take this opportunity to express my sincere appreciation and love to my parents, mother-in-law and my uncle's family. I would not have finished my long study journey without their support and love. Finally but certainly most important, I want to express my sincere thanks and love to my wife, Na, for being a constant source of support and encouragement, and for giving me all the love.

Dedication

To my family and friends

Abstract

As the workhorses of the plastics industry, polyolefins are consumed in the largest volume of all types of polymers. Despite their wide use, polyolefins suffer from poor adhesion and compatibility with other polar polymers due to their intrinsic low polarity and lack of functional groups.

The first goal of this study is to enhance interfacial adhesion between polyolefins with other polymers through coupling reaction of functional polymers. We have used functional polyethylenes with maleic anhydride, hydroxyl, primary and secondary amino groups grafted through reactive extrusion. Functional polyolefins dramatically improved the performance of polyolefins, including adhesion, compatibility, hardness and scratch resistance, and greatly expand their applications.

The second goal is to understand the factors affecting adhesion. We systematically investigated two categories of parameters. One is molecular: the type and incorporation level of functional groups. The other is processing condition: die design in extruders, reaction time and temperature. The interfacial adhesion was measured with the asymmetric dual cantilever beam test and T-peel test. The extent of reaction was quantified through measuring anchored copolymers via X-ray photoelectron spectroscopy. A quantitative correlation between adhesion and coupling reaction was developed.

A coextruded bilayer system with coupling reaction at interfaces was created to clarify the processing flow effects on the kinetics of coupling reactions. For the reaction between maleic anhydride modified polyethylene and nylon 6, the reaction rate during coextrusion through a fishtail die with compressive/extensional flow was strikingly almost two orders of magnitude larger than that through a constant thickness die without compressive flow. The latter reaction rate was close to that of quiescent lamination. We attribute the reaction acceleration through the fishtail die to the large deformation rate under the compressive/extensional flow condition. The deformation generated stretched chains leading to complimentary functional groups exposed to each other and forcing reactive species to overcome the interfacial diffusion barrier. We also found reaction

acceleration through a fishtail die for the coupling of functional PE with thermoplastic polyurethane. This work illustrates that enhancing the compressive/extensional flow during polymer processing may create opportunities for increasing adhesion and designing new reactions and products.

Table of Contents

Appendix

List of Tables

List of Figures

CHAPTER 1
Introduction

1.1 MOTIVATION AND GOALS

Polyolefins, including polyethylene (PE), polypropylene (PP), poly(alpha-alkene), ethylene-propylene elastomer (EPR), and ethylene-propylene-diene rubber (EPDM), are the most widely used commercial polymers, with over 53 billion pounds[1] US production, or around 60% of the total polymers.[2] Owing to their remarkable resistance to harsh chemical environment and a wide range of physical properties, polyolefins are found in a variety of applications including food packaging, high strength fibers, building materials, and automotive exterior parts. Despite their wide spread use, polyolefins suffer from relatively poor adhesion and compatibility with more polar polymeric materials due to their intrinsic low polarity and lack of reactive functional groups. [1-5]

Adhesion can be enhanced by adding an adhesion promoter that is capable of staying at the interface and entangling with both sides. This kind of "stitching"[3-5] can be created by adding premade block copolymers or forming copolymers *in situ* via coupling reactions at polymer-polymer interfaces. Premade copolymers tend to embed in the bulk phases, reducing the concentration of copolymers available in interfaces. Interfacial coupling reactions have some advantages: 1) most of the copolymers formed stay at the interface; 2) coupling reactions can link many homopolymer pairs for which the complementary block copolymer synthesis is not readily available.

For interfacial adhesion and coupling reactions, much of the fundamental work has been focused on glassy polymers. The adhesion involving semicrystalline polymers has been less well understood. In practice, there is much interest in combination of properties by adhesion between PE, which has high elasticity and low cost, and other thermoplastics, for example, thermoplastic polyurethane (TPU), which is known for high impact strength, abrasion resistance, and paintability. This research is motivated to improve adhesion by using interfacial coupling reaction. Moreover, in practice it is

desirable to improve adhesion by using low amounts of functional PE, due in large part to its higher cost. We will blend functional PE with PE and investigate adhesion between this blend with TPU as well.

The focus of this study is to enhance interfacial adhesion between polyolefins with other polymers through coupling reaction of functional polymers. Two categories of parameters influencing interfacial adhesion will be explored. One is molecular, including type and incorporation level of functional groups,[6] and chain architecture of functional polymers.[7] The other is processing, including die design in extruders, reaction time and temperature. A quantitative correlation between interfacial adhesion and coupling reaction will be developed and can be used to optimize the adhesion strength. A coextruded bilayer system with/without coupling reaction at interfaces was created to clarify processing flow effects. We will also show that functional polyolefins can dramatically improve the performance of polyolefins, including adhesion, compatibility, hardness and scratch resistance, and greatly expand the applications of polyolefins.

1.2 BACKGROUND

1.2.1 Functionalization of polyolefins

The functionalization of polyolefins is a useful methodology to chemically convert these extremely important commodities into value-added polymers with additional properties, such as adhesion, dyeability, paintability, wettability, and compatibility that are not characteristic of the starting macromolecules with a paraffin structure. The incorporation of only a few mole percent of functional groups into polyolefins can alter their properties without compromising the desired properties of the parent materials.[8-10] A tremendous amount of work has been done on the modification of polyolefins to incorporate functional groups. For example, free radical grafting of maleic anhydride is widely practiced in industry to functionalize PEs and PPs.[11-14]

Different ways of functionalizing and characterizing polyolefins are reviewed by Boaen et al.[8] The functionalization strategies include (a) direct copolymerization of normal olefins with monomers containing functional side groups, (b) copolymerization of

olefins with functional groups shielded during polymerization and subsequent de-protection, (c) copolymerization with monomers bearing substituents with latent reactivity and subsequent functionalization, and (d) post-polymerization functionalization of a polyolefin. Over the decades, polymer chemists and engineers have been trying to functionalize polyolefins through solution phase synthesis schemes and also reactive extrusion.[11-14] While some success has been achieved, the fundamental research problem of how to selectively and controllably place polar functional groups along the backbone of polyolefins is still largely unsolved.[15]

We plan to attack this problem on two interconnected fronts. We will explore the modification of polyolefin substrates using reactive extrusion suitable for alkane functionalization reactions. We will also investigate the influence of these modifications to key properties of the polyolefin substrates especially adhesion.

1.2.2 Adhesion between immiscible polymers

Most commercial polymer blends or multilayer products achieve their desired properties by combining the advantages of different polymers. However, adhesion between two immiscible polymers is usually very weak because there is little entanglement across the interface.[16-18] When two polymers are mixed together, due to the large molecular weight, entropy change of mixing, ΔS_{mix} is negligible. ΔH_{mix} is usually positive and accordingly ΔG_{mix} is positive, if there are no specific intermolecular interactions like hydrogen bonding. Most polymer blends are thermodynamically immiscible, resulting in a narrow interfacial width (a_I) and little penetration of polymer chains from one polymer to the other.

$$a_I = \frac{2b}{\sqrt{6\chi}} \qquad \text{(Equation 1.1)}$$

Here, χ is the Flory-Huggins interaction parameter and b is the statistical segmental length. The thickness of an interface between immiscible polymers is proportional to $\chi^{-1/2}$. As the miscibility of the polymer pair becomes worse, χ will increase and the

interface will become thinner. Most polymer pairs are immiscible and the interface between them is narrow according to Equation 1.1. The narrow interface leads to a low entanglement density across the interface, which results in a weak adhesion between polymers.

A substantial amount of effort has been made on adhesion between immiscible polymers over the last two decades. Brown et al.[19-21] have shown that the adhesion between immiscible polymers is usually very weak because there is little entanglement across the interface. Adhesion can be enhanced by adding a compatibilizer that is capable of staying at the interface and entangling with both sides. This kind of "stitching"[3-5] can be created by at least three methods: 1) adding premade block copolymers; 2) adding a tie layer, a third polymer which is at least partially miscible in each of the immiscible polymers; 3) forming copolymers *in situ* via coupling reactions at polymer-polymer interfaces. Premixed copolymers[22-24] tend to form micelles and embed in the bulk phases. This decreases the efficiency of premade block copolymers as compatibilizers. While a tie layer can interact with both of the immiscible polymers and "glue" them together, an extra layer and investment on infrastructure are always required.

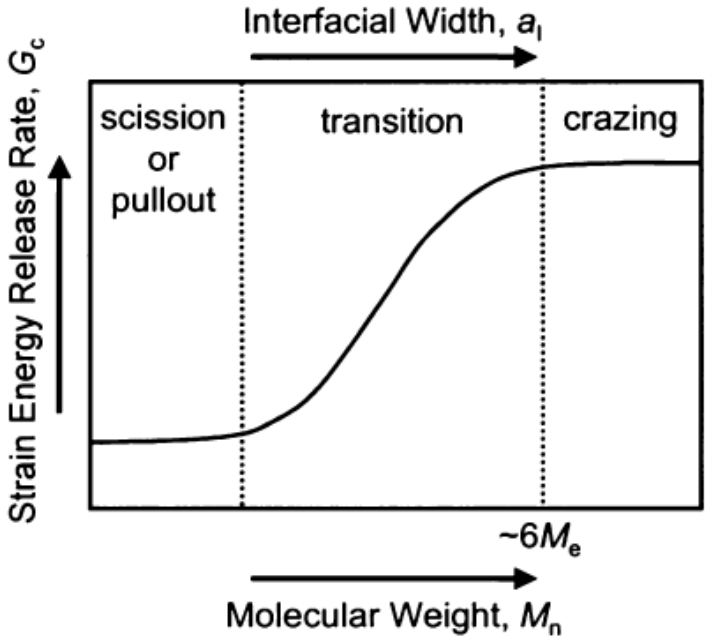

Figure 1.1 Mechanism of adhesion between glassy polymers. (Adapted from Cole et al.[4])

In situ coupling reactions[7,18,25-29] involve two immiscible polymers with complementary functional groups that can react to form block or graft copolymers. Most of the copolymers formed stay at the interface, instead of forming micelles in the homopolymer phase. *In situ* reaction is desirable from a material and economic point of view compared with adding pre-made block copolymers and adding tie layers, because functional polymers can be less expensive and *in situ* reaction can couple homopolymers for which block copolymers cannot be easily made based on regular synthesis routes.

Intermolecular entanglements occur in the interfacial layer defined in Equation 1.1. In most glassy polymeric systems different failure mechanisms dominate as shown in Figure 1.1: chain scission, chain pullout, and crazing.[30] As the interfacial width increases by changing χ, for example by random copolymerization, there is a transition from polymer chain scission or pullout to crazing. The same trends apply with increasing molecular weight at fixed χ and fixed composition of the two immiscible polymers.[31] For semi-crystalline polymers, different processing conditions may result in different types of morphology and degree of crystallinity near the interface, and hence influence adhesion mechanisms. Two adhesion/fracture mechanisms have been identified: adhesive failure at the interface and cohesive failure between polymer chains.[32] The dependence of adhesion on different parameters will be explained by these two mechanisms. Characterization of the cleaved surfaces will provide information on the understanding of fracture mechanisms.

1.2.3 Factors controlling interfacial coupling reactions

Chemistry effects

In order to understand the reaction kinetics at polymer interfaces, it is critical to know the reactivity of the complementary functional groups first. For example, Orr et al.[33] investigated the reactivities of complementary functional groups in polymer melts.

Homogeneous reactions were studied by blending PS chains with stoichiometric amounts of different functional groups. It was found that the reactivity of these functional groups followed the order: aliphatic amine/anhydride > aromatic amine/anhydride > acid/epoxy > acid/oxazoline > aliphatic amine/epoxy > aromatic amine/epoxy > hydroxyl/anhydride ~hydroxyl/acid > acid/amine. A very encouraging discovery was that coupling between terminal aliphatic amine and terminal cyclic anhydride could achieve complete conversion within thirty seconds. The fast reaction rate between aliphatic amines and cyclic anhydrides is one of the reasons why we utilized this reaction in melt blending in Chapter 2 and 4.

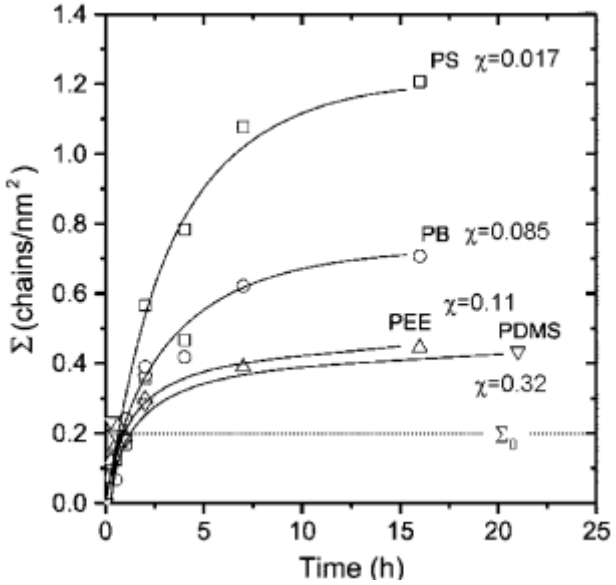

Figure 1.2 Interfacial copolymer coverage versus time for coupling reaction of anhydride grafted PMMA with complementary functional polymers at flat interfaces. (Adapted from Jeon et al.[34])

Miscibility of polymers

Reactive compatibilization involves the coupling reaction of polymers with complementary functional groups occurs in the interfacial region of the two immiscible polymers. The interfacial thickness for immiscible polymer is usually between 5-50 nm.

The thickness of the interfacial layer varies depending on the miscibility of the two polymers. The interfacial layer acts as a reaction zone for the coupling reaction. The variable thickness means the reactor volume for the coupling reaction changes with the miscibility of the two polymers. Therefore, the coupling reaction rate should depend on the miscibility of the polymers. In Figure 1.2, different polymers with complementary functionalities were annealed with anhydride grafted PMMA. For all the polymers, the χ value between the annealed polymer with PMMA decreases in the sequence: PDMS > PEE > PB >PS, indicating that the interfacial thickness increases from PDMS to PS. It can be seen from the figure that interfacial coverage increases with interfacial thickness due to better miscibility.

Processing effects

Although many aspects of reactive blending have been investigated by using quiescent bilayers including reactivity,[33] architecture,[7] molecular weight,[35] and concentration of functional polymers,[26] reaction kinetics under flow still remains a big challenge. The common wisdom for reactions between *small molecules* under flow is that external mass transfer increases the reaction rate by increasing concentration of reactive species, without affecting reaction mechanism and transition states at a certain temperature. However, for reactions between *macromolecules* under flow, the kinetics is more complicated.

Jeon et al.[34] found that flow affects the interfacial reaction tremendously, resulting in a rate constant over 1000 times higher in heterogeneous melt blending than that in the static bilayer film. Based on Orr's results, the rate constant of the same coupling reaction in homogeneous blending is even ~20 times higher than heterogeneous mixing.

It should be noted that a significant amount of interface was generated during mixing, the large difference observed in rate constant seemed reasonable. However, after normalizing by interfacial area, the rate constant under mixing was still ~300 times higher than that at static interfaces. Apparently, besides interfacial area generation, the complex flow under mixing also changed reaction kinetics significantly.

It is generally difficult to study the effects of flow on macromolecules reactions during mixing because interfacial area generation and flow patterns are always convoluted and hard to isolate. Yet the influence of interfacial area generation can be separated from the influence of flow by coextrusion,[36-38] a process in which two or more polymer layers are combined and extruded simultaneously. Coextrusion provides an ideal model system for studying interfacial phenomena as the amount of interface is well defined.

Although inter-diffusion,[39] reaction,[18] and slip at polymer–polymer interface[36,37] have been explored, there are very few studies that investigate how the interfacial reaction and adhesion depend on the flow conditions during processing. For example, under coextrusion conditions, Zhang et al.[18] determined that the coupling reaction of amine terminal polystyrene (PS-NH_2)/anhydride terminal poly(methyl methacrylate) (PMMA-anh-anth) was as rapid as that under mixing and was up to 1000 times faster than that under quiescent annealing.

While Zhang et al. determined reaction acceleration through coextrusion with well-defined interfaces, several flow patterns were still convoluted in multi-layer coextrusion and there was lack of understanding on the interfacial area generation in coextrusion. We will show in this research that we can eliminate shear flow by bilayer coextrusion and we have developed methods to deconvolute the generation of copolymers and interfacial area generation.

1.3 OVERVIEW OF THESIS

To achieve the goal of enhancing and controlling adhesion of polyolefins with other polymers, four aspects have been probed: functionalization of polyolefins, kinetics of coupling reactions at immiscible interfaces, correlation between adhesion promotion and coupling reactions, processing flow effects on reaction kinetics/ adhesion. All these issues were systematically studied in Chapter 2-7.

In Chapter 2, in an effort to improve the adhesion property of polyolefins, primary and secondary amino-functionalized PEs were synthesized. The primary one was

synthesized from commercially available maleic anhydride-modified polyethylene (PE-*g*-MA) by reaction with mono-tert-butoxycarbonyl-protected diamine, followed by deprotection. Secondary amino-functionalized PE was synthesized by reactive extrusion of PE-*g*-MA with a primary-secondary diamine. The amino-functionalized polymers showed drastically improved adhesive strength toward thermoplastic polyurethanes (TPU) as compared to the parent PE-*g*-MA.

In Chapter 3, we blended maleic anhydride (MA), hydroxyl (OH), and secondary amine (NHR) functionalized PEs into non-modified PE. We bonded these PEs to TPU via lamination and coextrusion. Amine functionalized PE showed dramatic adhesion improvement even at 1 wt % in the blends. The development of adhesion in coextrusion was much faster in comparison with lamination at the same temperature. This difference was attributed to the extensional and compressive flow in coextrusion overcoming the diffusion barrier at the interface and forcing reactive species to penetrate into the interface.

Chapter 4 continued to study the processing flow effect on the kinetics of interfacial coupling reaction. The reaction rate through a fishtail die was, strikingly, two orders of magnitude larger than that through a constant thickness die. The latter rate was close to quiescent lamination. This result is consistent with Chapter 3. We attribute the reaction acceleration through the fishtail die to the large deformation rate under the compressive/extensional flow condition. The deformation generated stretched chains leading to complimentary functional groups exposed to each other and forcing reactive species to overcome the interfacial diffusion barrier.

Chapter 5 and 6 explored the efficiency of functional polyolefins as compatibilizers for polyolefin/polar polymer blends. In Chapter 5, maleic anhydride grafted polyethylene was used to compatibilize olefin block copolymer with TPU. Paint adhesion to polyolefin was significantly improved by blending TPU. The mechanism of paint adhesion was examined by studying blend morphologies near paint/polymer interface and the surface composition of substrates. In Chapter 6, improvements in hardness, modulus, scratch resistance, particle dispersion and adhesion were observed for

blends of functional poly(propylene-*co*-ethylene) (PPE)/PMMA compared to non-modified PPE.

In Chapter 7, adhesion between PE and various PPs, including propylene ethylene random copolymers and impact modified PP, was investigated. It should be noted that there was no chemical reaction occurring at the interface. Cooling rate, flow rate ratio and draw down speed influenced interfacial adhesion. Materials composition, specifically percentage of ethylene, determines the compatibility of the PP materials with PE and hence interfacial adhesion. AFM and TEM images revealed roughened interfaces for samples with strong adhesion.

CHAPTER 2

Amine Grafted Polyethylene for Improved Adhesion

2.1 OVERVIEW

In an effort to improve the adhesion property of polyolefins, by using reactive extrusion primary and secondary amino-functionalized polyethylenes were synthesized. The primary one was synthesized from commercially available maleic anhydride-modified polyethylene (PE-*g*-MA) by reaction with mono-tert-butoxycarbonyl-protected diamine, N-(tert-butoxycarbonyl)-1,6-diaminohexane (*t*BocHMDA) followed by deprotection with trifluoroacetic acid. Secondary amino-functionalized polyethylenes were synthesized by reactive extrusion of PE-*g*-MA with a primary-secondary diamine. The structures of amino-functionalized polyethylenes were characterized by NMR and IR spectroscopies. The amino-functionalized polymers showed drastically improved adhesive strength toward thermoplastic polyurethanes (TPU) as compared to the parent PE-*g*-MA.

2.2 INTRODUCTION

As the workhorses of the plastics industry, polyolefins are consumed in the largest volume of all types of polymers. In addition to being easily processed, a wide range of physical properties and produced using highly efficient catalysis, polyolefins are remarkably stable toward harsh chemical environments. This is due in large part to the resistance of polyolefins (essentially macromolecular alkanes) to chemical modification/degradation. They are found in a variety of applications including food packaging, high strength fibers, building materials, and automotive exterior parts.

However, despite their wide spread use, polyolefins suffer from relatively poor adhesion and compatibility with more polar polymeric materials, due to their intrinsic low polarity and lack of functional groups along the chain.

It is generally difficult to modify pololefins by incorporating functional groups into alkane substrates primarily due to the strength of their carbon-carbon and carbon-hydrogen bonds. However, it has been proven that the incorporation of even a few mole percent of functional groups can lead to dramatically improved adhesion characteristics and compatibility of polyolefins with other polymers.[8] Over the decades, polymer chemists have been trying to achieve this goal through solution phase synthesis schemes. While some success has been achieved, solution phase synthesis has the intrinsic disadvantage of usage of solvents, long reaction time and relatively high costs due to the usage of solvents and development of catalysts.

Reactive extrusion,[11,14,40,41] an alternative process of functionalizing polyolefins, involves the synthesis of materials by a melt phase reaction in an extruder. The advantages of synthesizing polyolefin graft copolymers by reactive extrusion[40] as opposed to alternative solution phase technologies include: little or no use of solvents, simple product isolation, short reaction times, continuous process, and relatively low infrastructure costs. In this chapter, we set out to incorporate a primary-secondary diamine onto maleic anhydride grafted PE by using reactive extrusion. We will also incorporate primary and secondary amines into PE without cross-linking by reacting commercially available maleic anhydride grafted PE with mono-protected diamine modifiers followed by deprotection to liberate the corresponding primary amines. As discussed in Chapter 1, this research is motivated by the desire to improve adhesion between PE with other polymers. In practice it is desirable to improve adhesion by using low amount of functional PE due in large part to the relative higher cost of functional PE than PE. We will show that adhesion between PE and thermoplastic polyurethane (TPU) could be improved dramatically by blending a small amount of functional PE that we made.

2.3 EXPERIMENTAL

2.3.1Materials

Ethylene/1-octene random copolymer (ENGAGE™ 8200), PE, was provided by The Dow Chemical Company. This copolymer has 7.3 mol% octene with a melt flow rate (MFR) of 5.0 dg/min and density of 0.870 g/cm^3. The anhydride-functionalized ethylene/1-octene copolymer (AMPLIFY™ GR 216), PE-*g*-MA, was prepared by free radical grafting of maleic anhydride onto a different grade ethylene/1-octene copolymer with the same percentage of octane in the melt using continuous reactive extrusion described in detail elsewhere.[42] This ethylene/1-octene copolymer (ENGAGE™8407) has 7.3-7.7 mol% octene with a melt flow rate (MFR) of 30 dg/min and density of 0.870 g/cm^3. The MFR of PE-*g*-MA was ~1.3 g/10 min and the anhydride content was determined to be 0.8 wt% by a calibrated FT-IR analytical method. 0.8 wt% corresponds to about one succinic anhydride group per 1000 -CH_2- units on the polyolefin backbone.

TPU (Avalon® 70 AE) with polyester soft segments was provided by Huntsman Polyurethanes. It has a number average molecular weight of 77.5 kg/mol and PDI 1.7 based on polystyrene standards (EasiCal PS-2, Polymer Laboratories) as determined by size exclusion chromatography (SEC, Waters 717 Plus HPLC Autosampler) at room temperature using tetrahydrofuran (THF) as a mobile phase. Key properties of PEs and TPU are listed in Table 2.1. TPU pellets were dried overnight in a conventional static oven at approximately 70 ℃ to remove residual moisture before compression molding.

The shear modulus and viscosities of PE and all the functionalized PEs were measured at 180 ^{o}C under N_2 atmosphere by a strain controlled rotational rheometer (ARES, TA Instruments) using 25 mm parallel plates.

2.3.1.1 Synthesis of primary amino-functionalized PE (PE-*g*-NH_2) via reactive extrusion

Synthesis of PE-g-NHtBoc by reactive extrusion

PE-*g*-MA and *t*BocHMDA were mixed by melt blending in a DACA Mixer, a vertical co-rotating twin screw extruder with a recirculation channel. For all batches, 4 g PE-*g*-

MA was added into the compounder and mixed for 3 minutes, then 2-3 equivalents (MA/NH_2) of *t*BocHMDA sealed in a premade PE-*g*-MA bag was added and allowed to react at a screw speed of 75 rpm under nitrogen. Then the samples were extruded for about 3 minutes and cooled down to room temperature.

Table 2.1 Notations for the starting chemicals used in this study.

Polymer	M_n ($kg.mol^{-1}$)	PDI	f_n [b]	Structure	Supplier
PE	70.5	2.5	-	Copolymer of ethylene and octene (7.3 mol% octene)	Dow[a] (ENGAGE 8200)
PE-*g*-MA[c]	67	3.0	5.4	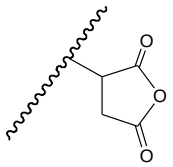	Dow (AMPLIFY™ GR 216)
TPU[d]	86	2.4	154	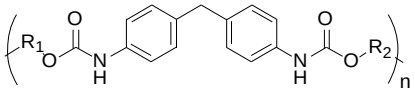	Huntsman (Avalon70AE)
*t*BocHMDA[e]	-	-	-	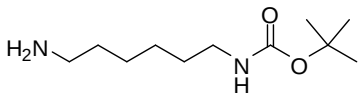	Shingo Kobayashi
EEDA	-	-	-	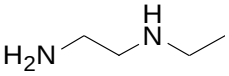	Aldrich

[a] For all the polymers provide by The Dow Chemical Company, Mn, PDI, f_n data came from the supplier.

[b] Average number of functional groups per chain based on Mn. Carbamate groups are

counted for TPU.

[c] Maleic anhydride(MA) grafted polyethylene.

[d] R_1, R_2 = aliphatic ester.

[e] *t*Boc = t-Butoxycarbonyl.

Acid deprotection of PE-g-NHtBoc

About 4 g of extruded PE-*g*-NH*t*Boc was dissolved in about 150 mL benzene at 85 ^{o}C. 10 mL TFA (trifluoroacetic acid) was added to the benzene solution and it was refluxed for at least two hours. After the solution was cooled down, it was added dropwise to 1.2 L methanol and the suspension was stirred for one hour. The precipitate was filtered and collected, and then it was dissolved in benzene and precipitated in methanol again. Half saturated $NaHCO_3$ solution was added to methanol until pH became around 7. The polymer was filtered and washed by distilled water several times, and then it was dried in a vacuum oven at room temperature.

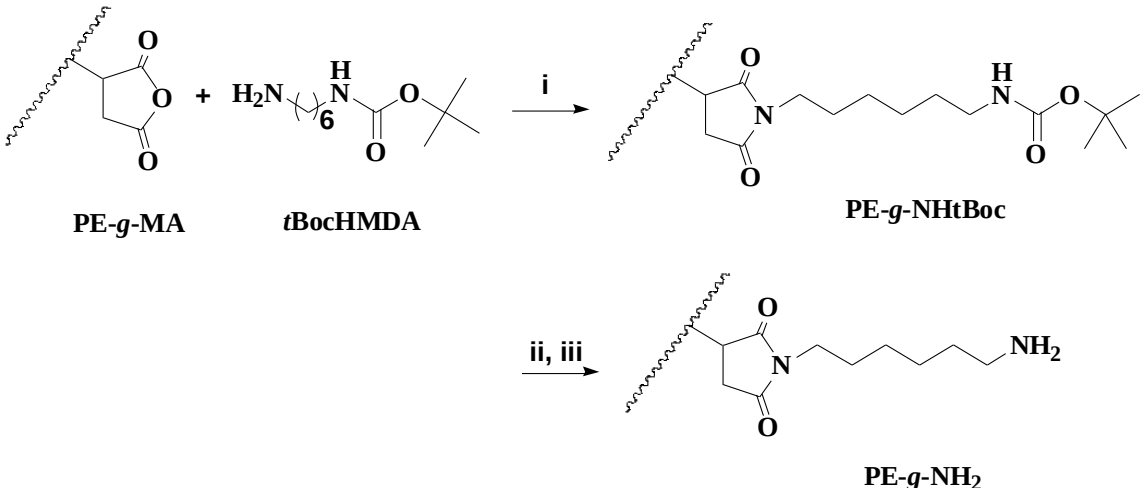

Scheme 2.1 Synthesis route of PE-*g*-NH_2. (i) reactive extrusion, 180 ℃. (ii) TFA, 75 ℃, benzene, 2 h. (iii) precipitation, MeOH/H_2O/$NaHCO_3$, 90 wt % yield. (∿ : PE backbone)

2.3.1.2 Synthesis of secondary amino-functionalized PE (PE-*g*-NHEt) via reactive extrusion

Reactive mixing was performed using an instrumented batch mixer (HAKKE Polylab mixer driven by OS RheoDrive 4, Thermo Electron Corp.) using two counter-rotating roller blades. Secondary amine grafted polyethylene, PE-*g*-NHEt, was synthesized by the reaction between PE-*g*-MA and N-ethylethylenediamine (EEDA). Polymer pellets were added first and mixed for about 2 min at 180 ℃ and rotor speed of 75 rpm. Once the torque settled to a steady value for about 15 seconds, EEDA was added. The amount of diamine added to the polymer melt was calculated based on 0.85 wt % MA groups on the PE backbone. A greater excess of diamine in the reaction mixture was used in an attempt to lower crosslinking.[43] The reactive mixture was then mixed for 5 min at 180 ℃ and a rotor speed of 75 rpm. The resulting functionalized polyolefin was removed from the mixing chamber and allowed to cool at room temperature.

2.3.1.3 Characterization

Determination of $-NH_2$ presence by Kaiser test

Intensive blue color is expected if there is $-NH_2$ group present. This test shows no typical blue color for serine, asparagines, aspartic acid, proline or secondary amine. The procedures are as following:

1. Wash polymers three times with ethanol.
2. Transfer the polymers into a small glass tube and add three drops of each solution (a. Phenol, ~80% in ethanol b. KCN in H_2O/pyridin c. Ninhydrin, 6% in ethanol).
3. Mix well and heat the test tube at 120 ℃ for 5 minutes.

Determination of gel content by solvent extraction

DACA extruded samples PE-*g*-NH*t*Boc were cut into thin pieces, put into a basket made from 335 mesh stainless steel sheet, and immersed into boiling benzene refluxing for at least 20 h. The basket was taken out and dried overnight under vacuum at 85 ^{o}C until constant weight was obtained. The gel content was defined as the ratio of the weight of residual polymer in the basket over the original weight.

Adhesion between PE and TPU with PE-g-X solution coated in between (X= MA, NH_2, NHEt)

In order to test the capabilities of functional PEs as adhesion promoters, they were coated between non-modified PE and TPU films, annealed at 180 ℃ and adhesion between PE and TPU was tested. PE and TPU films (80mm×7.5mm×0.4mm) were prepared by compression molding from pellets at 120 ℃ and 180 ℃ respectively under 2 MPa between two polytetrafluoroethylene (PTFE) coated aluminum foils (Saint-Gobain Performance Plastics). The PE and TPU films were dried in vacuum oven at room temperature and 70^{o}C respectively.

All the functional PEs were dissolved in benzene at 80 ℃ (0.03g/ 13ml), and then the temperature of the solution was lowered to 50 ℃. Premade TPU films were dipped into the solution for 5 seconds and then dried in fume hood. Then coated TPU film and premade PE film were pressed into intimate contact (sandwiched between two PTFE-coated aluminumfoils) and laminated for 100 seconds at 180 ℃ under 0.1 MPa pressure. The bilayer samples were cooled by water to room temperature. The peel tests were performed on a MINIMAT Tensile tester at an extension rate of 0.33 mm/s and a total travel of 50 mm.

Adhesion between TPU and PE-g-X/PE blend (X= MA, OH, NHEt)

PE-*g*-X/PE blends were made by melt mixing in a DACA Mixer. Then PE-*g*-X/PE and TPU films were prepared using compression molding at 180 ℃ under 2 MPa for 3 minutes. Then PE-g-X/PE and TPU films were stacked between two Teflon sheets

and annealed at 180 ℃ under 0.1 MPa. Bilayer specimens were cooled down by water to room temperature. Adhesion between PE-*g*-X/PE and TPU was tested using a Microbionix (LVDI, MTS Systems Corp.) instrument. The instrument had a 5 N load cell and a programmable extension rate. The tests were performed using an extension rate of 1 mm/s and a total travel of 50 mm.

^{1}H NMR

^{1}H NMR were recorded on a Varian INOVA-300 or Varian INOVA-500 spectrometer at room temperature. Benzene-d6 was used for high temperature (70 ℃) NMR measurements. Proton chemical shifts are referenced to residual protons in $CDCl_3$ (7.26 ppm) and benzene-d6 (7.16 ppm). Carbon chemical shifts are referenced to $CDCl_3$ (77.1 ppm).

FTIR Spectroscopy

Polymer films of ~100 μm were prepared by compression molding at 110 ^{o}C under 2 MPa for 3 min and allowed to cool down by water to room temperature. FTIR spectrometer (Magna-IR 760, Nicolet) was used and thirty two scans from 4000 to 650 cm^{-1} with a resolution of 4 cm^{-1} were acquired for each sample.

High Temperature Gel Permeation Chromatography

The PL-GPC 220 integrated high temperature GPC system (Agilent Systems) was used to measure the molecular weights and distribution of PPE materials. Trichlorobenzene (TCB) with 0.0125 wt% of butylated hydroxytoluene (BHT) was used as eluent phase with flow rate 1.0 ml/min at 135 ℃. The data were analyzed against a polystyrene standard calibration using the following Mark-Houwink parameters:[44]

Polystyrene in TCB: $K=12.1\times10^{-5}$ $\alpha=0.707$

Linear polyethylene in TCB: $K=30.1\times10^{-5}$ $\alpha=0.75$

Differential scanning calorimetry (DSC)

Differential scanning calorimetry was performed on a TA DSC Q1000 utilizing an indium standard for temperature calibration. At least 4 mg of sample contained in hermetically sealed aluminum pans were analyzed under N_2 with a 10 ℃/min heating rate. Thermal transition temperatures were determined from the second heating after annealing above the glass transition or melting point for at least 1 min to erase thermal history.

Rheology

Dependence of storage modulus on frequency was analyzed by a dynamic oscillatory rheometer (TA instruments). Samples were compression-molded (Wabash compression molder) at 110 ^{o}C under a pressure of 0.2 MPa for 3 min in 25 mm round disks. Rheological tests were performed with dynamic frequency sweep strain 1 % at 180 ^{o}C.

2.4 RESULTS AND DISCUSSION

2.4.1 Synthesis of PE-*g*-NH_2 and PE-*g*-NHEt

Primary amine grafted PE (PE-*g*-NH_2) was synthesized via reactive extrusion. In order to make primary amine grafted PE, at first hexamethylenediamine (HMDA), primary-primary diamine was used to blend with PE-*g*-MA in DACA mixer at 180 ℃. The reaction between cyclic anhydride and aliphatic primary amine is extremely fast. Orr and coworkers reported that coupling reactions in both homogeneous and heterogeneous polymer blends were found to be complete in ~30 seconds at 180 ℃.[33] Consequently, the grafted maleic anhydride functional groups are expected to be completely converted after 3~5 minutes blending of PE-*g*-MA and small molecule diamine.

Due to the fast reaction of maleic hydride with primary amine, almost 100 % completion of the grafted maleic anhydride was achieved within 5 minutes. By reacting PE-*g*-MA with a primary secondary diamine EEDA, the unequal reactivity of the primary secondary diamine resulted in a grafted secondary amine group and greatly reduced

branching. However, since both amine groups in HMDA can react with MA, a high gel content was obtained even when 10 times of excessive amount of HMDA was used. In order to prevent crosslinking, one end of HMDA was protected by *t*Boc (tert-butoxycarbonyl) group.

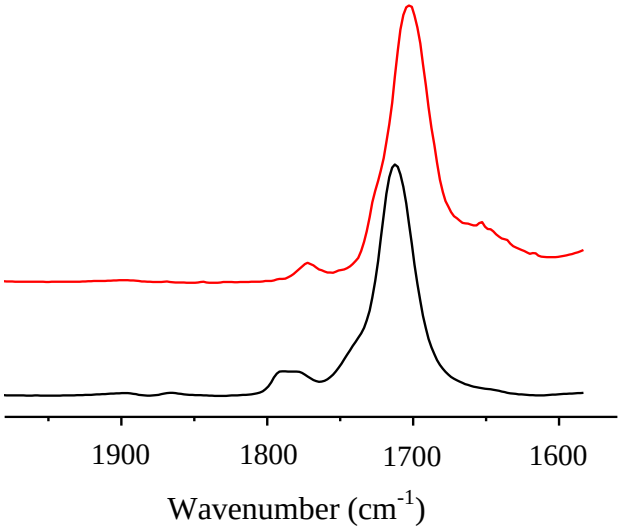

Figure 2.1 FTIR spectra of PE-*g*-NH*t*Boc, the reaction product of PE-*g*-MA and *t*BocHMDA via reactive extrusion at 180 ℃. The upper curve is the spectrum of PE-*g*-NH*t*Boc; the bottom one is for PE-*g*-MA.

Table 2.2 IR absorption bands and designation for PE-*g*-MA and PE-*g*-NH*t*Boc.

Absorption bands (cm^{-1})		Designation
PE-*g*-NH*t*Boc	PE-*g*-MA	
3361	-	N-H stretching of carbamate
-	1789	C=O stretching of succinic anhydride
1772	-	C=O stretching of imide
-	1712	C=O stretching of carboxylic acid
1703	-	C=O stretching of imide
1651	-	C=O stretching of carbamate
1561	-	N-H bending mode of amide

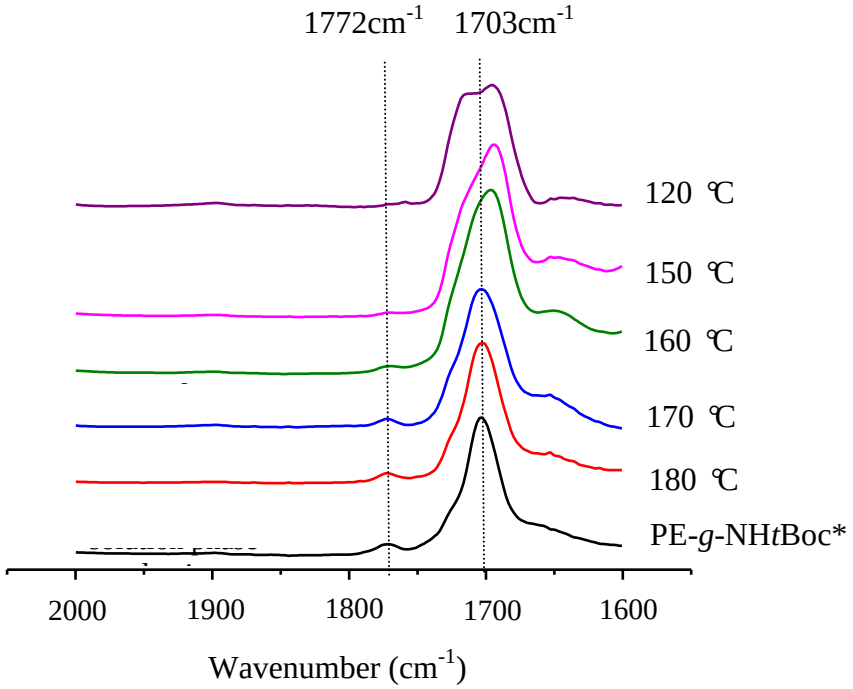

Figure 2.2 FTIR of PE-*g*-NH*t*Boc blended at different temperatures. (*:PE-*g*-NH*t*Boc synthesized from solution phase provided by courtesy of Shingo Kobayashi.[45])

The reaction product of PE-*g*-MA and *t*BocHMDA is referred as PE-*g*-NH*t*Boc. FTIR spectra of PE-*g*-MA and PE-*g*-NH*t*Boc are shown in Figure 2.2. The absorption bands at 1789 cm^{-1} and 1712 cm^{-1} are assigned to be C=O stretching of succinic anhydride and carboxylic acid respectively, which disappeared rapidly within only 5 min in the reaction. The new bands at 1771 cm^{-1} and 1703 cm^{-1} are due to the formation of imide. The experimental conversion data followed the prediction that assumes a complete reaction between primary amine of *t*BocHMDA and succinic anhydride.

For reaction between PE-*g*-MA and *t*BocHMDA in melt blending, as temperature increases, the reaction is driven to completion. However, *t*Boc group will have a higher chance to cleave, which leads to crosslinked product. In order to find the optimum processing temperature, reactive extrusion was carried out at different temperatures. FTIR spectra of products obtained at different temperatures are shown in Figure 2.2. For

products obtained at 170 ℃ and 180 ℃, their FTIR absorption bands have the same peak values with PE-*g*-NH*t*Boc synthesized from solution phase. The structure of PE-*g*-NH*t*Boc obtained from solution phase was verified by ^{1}H NMR and FTIR.[45] At 120 ℃, 150 ℃, and 160 ℃, there are obvious peak shifting due to the incompletion of reaction. Reactions at low temperature had two results: low diffusivity of *t*BocHMDA which would cause the mixing inefficiency of *t*BocHMDA and PE-*g*-MA and incomplete reaction between *t*BocHMDA and maleic anhydride group grafted on polymer backbone.

2.4.2 Determination of gel content by solvent extraction

Gel content values for different polymer samples are shown in Table 2.3. For PE-*g*-MA, when maleic anhydride was grafted onto PE by radical reaction, there was some crosslinking or long chain branching due to side reaction caused by radical pieces. Therefore, the gel content for PE-g-MA was not zero.

Table 2.3 Gel content for polymer samples.

Sample	Composition	Gel Content/%
PE-*g*-MA	-	0.6 ± 0.05
PE-*g*-NH*t*Boc (150 ℃)	MA/*t*BocHMDA =1/3[a]	0.66 ± 0.07
PE-*g*-NH*t*Boc (160 ℃)	MA/*t*BocHMDA =1/3	1.1 ± 0.04
PE-*g*-NH*t*Boc (180 ℃)	MA/*t*BocHMDA =1/3	1.7 ± 0.2
PE-*g*-NH_2 (180 ℃)[c]	MA/HMDA =1/5[b]	62 ± 3
PE-*g*-NH_2 (180 ℃)[c]	MA/HMDA =1/10[b]	29 ± 2
PE-*g*-NH_2 (180 ℃)[d]	MA/HMDA =1/10[b]	1.1 ± 0.05

[a] Molar ratio of MA over *t*BocHMDA.

[b] Molar ratio of MA over total amount of NH_2 in HMDA.

[c] Reactive extrusion products of PE-*g*-MA and HMDA.

[d] Reactive extrusion products of PE-*g*-MA and *t*BocHMDA, then deprotected by trifluoroacetic acid

In order to synthesize primary amine grafted PE, excess amount of HMDA was initially used to blend with PE-*g*-MA at 180 ^{o}C. High gel contents were obtained, 29.4% for MA/HMDA=1/10 and 61.9% for MA/HMDA=1/5. Gel content was decreased by increasing the excess amount of diamine, but even for 10 times equivalent of diamine, the gel content was still too high from a practical perspective.

For the synthesis of PE-*g*-NH*t*Boc via reactive extrusion, one end of diamine small molecule was protected by *t*Boc group, which significantly decreased the gel content, as we expected. In addition, Table 2.3 shows that the gel content increased slightly as processing temperature increased from 150 ^{o}C to 180 ^{o}C. This is presumably due to the thermal deprotection of *t*Boc group. At high temperature, the initially protected amine group may be deprotected and react with MA from another polymer, which leads to crosslinking.

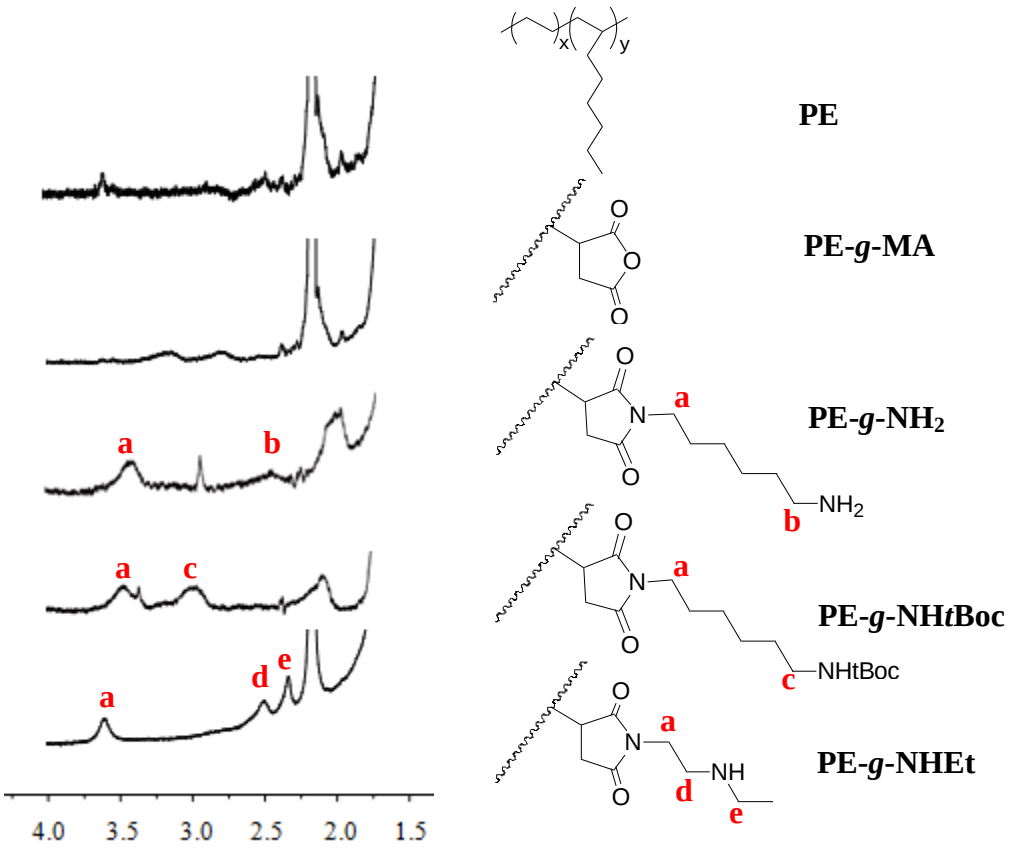

Figure 2.3 Magnified ^{1}H NMR spectra of the non-modified and functionalized polyolefins. The corresponding structures and abbreviations of the polyolefins are presented on the right.

Rheology

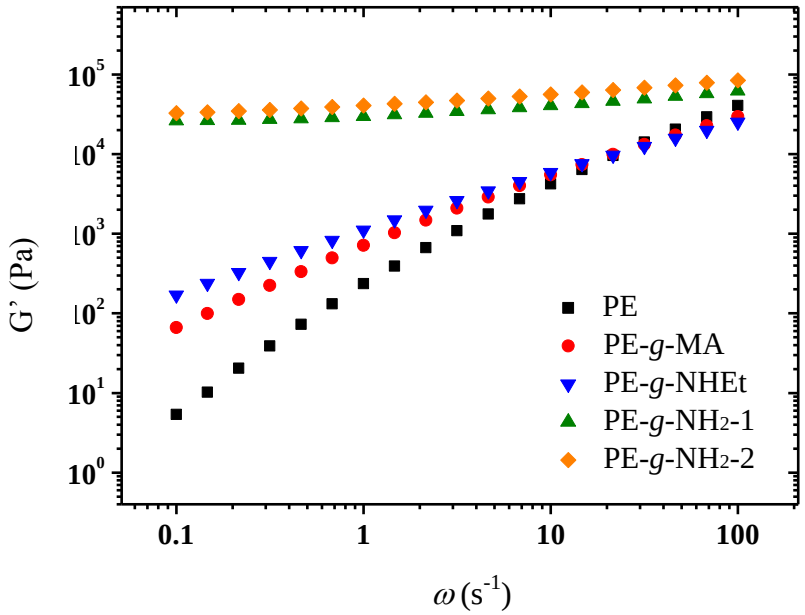

Figure 2.4 Dynamic frequency sweep of PE and functional PEs.
(PE-*g*-NH_2-1: primary amine grafted PE obtained in this research; PE-*g*-NH_2-2: primary amine grafted PE synthesized solely from solution phase.[45])

For dynamic frequency sweep, G' at low frequency is very sensitive to the molecular weight and material structure. PE-*g*-MA was obtained by free radical grafting reaction between PE and maleic anhydride. While this functionalization imparts maleic anhydride into polyethylenes, the process also induces crosslinking. Therefore, there is higher percentage of polymer chains that cannot relax at low frequency region. For PE-*g*-NHEt, primary-secondary diamine was used to react with PE-g-MA to obtain this product. It has been shown that this process could introduce slight crosslinking to the

polymer products, which led to higher value of G' than that of PE-*g*-MA at low frequency. For PE-*g*-NH_2-1and PE-*g*-NH_2-2, there are plateaus for storage moduli of both of them at low frequency, which indicates formation of macroscopic network. This result seems to contradict with the gel contents data obtained. A possible explanation is that although it was easy for PE-*g*-NH_2-1 and PE-*g*-NH_2-2 to reach their gel point during synthesis due to the low value of get point (1/weight-average degree of polymerization), there is still a substantial amount of primary amine grafted PE left. Kobayashi et al.[45] also proved that PE-*g*-NH_2-2 has very little crosslinking from GPC measurement. As the G' curve of PE-*g*-NH_2-1 almost overlapped that of PE-*g*-NH_2-2, we conclude that there was very limited amount of crosslinking, which is consistent with the gel content measurement.

2.4.3 Determination of $-NH_2$ on polymer surface by Kaiser test

Table 2.4 Determination of $-NH_2$ on polymer surface.

Sample	Solution Color	Presence of $-NH_2$
Reagent Solution (No polymer)	Yellow	No
PE	Yellow	No
PE-*g*-MA	Yellow	No
PE-*g*-NH_2	Dark Blue	Yes

Kaiser test is routinely applied qualitatively and quantitatively in solid phase peptide synthesis to monitor the presence of primary amine groups.[46] Intensive blue

color will be generated if there is primary amine group on the polymer surface. Additionally, there will be no typical blue color for serine, asparagines, aspartic acid, proline or secondary amine. As shown in Table 2.4, for PE and PE-*g*-MA, due to the lack of primary amine group, the reagent solution for both polymers showed yellow color, a typical color denoting no existence of amine groups. Dark blue color appeared for PE-*g*-NH_2 indicating the presence of primary amine in the PE-*g*-NH_2 sample we obtained.

2.4.4 Interfacial coverage of copolymers

Molecules containing functional groups for interfacial reaction are found to have a strong tendency to move to interface, resulting in a large concentration gradient near the interface.[47] Since the concentration of urethane linkages is much higher than that of amine group and only the functional groups in the interfacial region with a thickness of several nanometers can react, the primary or secondary amine groups at the interface are instantaneously consumed due to the fast reaction kinetics. Therefore the overall interfacial reaction is limited by the center-of-mass diffusion of the functional PE chains in the matrix of non-functional PE toward the interface.

The NHEt group concentration (C_x, mol/mL) can be calculated from PE-*g*-NHEt concentration in the blend (*w*, in wt%), graft content of PE-g-NHEt (0.55 wt.%), density of PE (0.87 g/cm^3), and molar mass of NHEt (170 g/mol).

$$C_x = \frac{\frac{w \times 1.1\%}{170}}{1/0.87} = 5.6 \times 10^{-5} w \qquad \text{(Equation 2.1)}$$

A characteristic diffusion length (d) during time t is $d = \sqrt{Dt}$. While real numbers of the diffusion coefficient (D) are not readily available, D is on the order of 10^{-11}~10^{-13} cm^2/s for most linear entangled polymers in melt. Therefore, D = 10^{-12} cm^2/s was chosen as an approximation.

The maximum areal density (Σ_{max}, chains/nm^2) of the copolymer from the PE-*g*-NHEt reaction can be estimated:

$$\sum_{max} = \frac{6.02 \times 10^{23} \times C_x d}{10^{14} \times n} \qquad \text{(Equation 2.2)}$$

where n is the average number of functional groups per polymer chain. In the annealing time of 5 min, only the functional PE chains within around 0.2 μm thick layer have a chance to react with urethane linkages at the interface, leading to Σ_{max} of copolymers from the PE-g-NHEt reaction to be 0.16, 0.81, 1.62 chains/nm^2 for w = 1, 5, 10 %, respectively. In order to achieve even higher interfacial coverage, functional group with even higher reactivity is needed. Since NH_2 showed higher reactivity with urethane linkage than NHR, PE-*g*-NH_2 was synthesized. We will compare the efficiency of primary and secondary amino-functionalized PE as adhesion promoters as follows.

2.4.5 Adhesion comparison between PE-*g*-NHEt and PE-*g*-NH_2

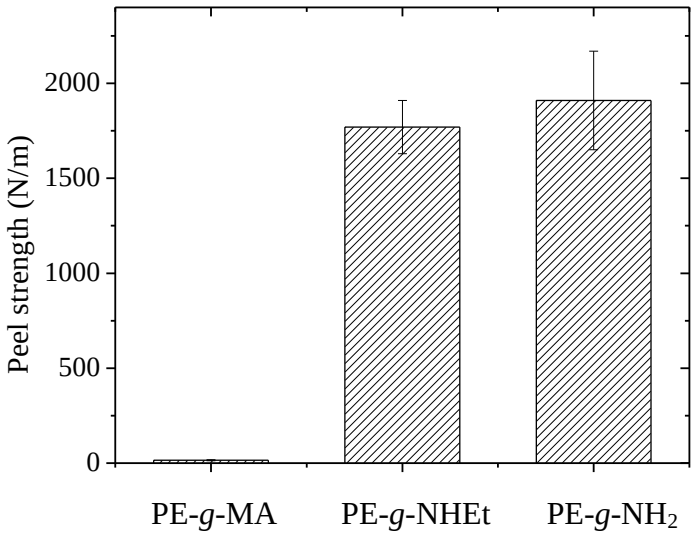

Figure 2.5 Peel strength for adhesion between PE and PE-*g*-X solution coated TPU (X= MA, NHEt, NH_2). Peel strength is defined as the ratio of peeling force over peeling arm width.

Figure 2.5 shows that for adhesion between PE and PE-*g*-X solution coated TPU, PE-*g*-NH_2 and PE-g-NHEt showed much higher peel strength than PE-*g*-MA. This is consistent with the reactivity ranking of functional groups with urethane lingkage (NH_2 >

NHR > MA) as determined by Lu et al.[48] For the same amount of annealing time, higher activity of functional group leads to larger interfacial copolymer coverage hence stronger adhesion. The dependence of adhesion on functional group reactivities will be discussed in detail in the next chapter.

Primary amine group was proven to have higher reactivity than secondary amine with urethane linkage. Therefore, PE-*g*-NH_2 was expected to have better adhesion than PE-*g*-NHEt in our work. However, the difference was not statistically significant. This is likely due to the fact that primary amine groups grafted on polymers would degrade in air, as proved by Ghasemi et al.[49] In this research, PE-*g*-NH_2 was exposed to air for several days, which would cause primary amine groups to degrade to certain degrees. An alternative explanation would be that the high surface energy of primary amine groups made them embed in the polymer matrix, and therefore fewer primary amines came to the interface to react with urethane linkage.

2.5 CONCLUSION

Primary amino functionalized polyethylene (PE-*g*-NH_2) was synthesized from commercially available PE-*g*-MA by reaction with mono *t*Boc protected diamines *t*BocHMDA, followed by deprotection without significant cross-linking. Secondary amino functionalized polyethylene (PE-*g*-NHEt) was synthesized by reactive extrusion of PE-*g*-MA with a primary-secondary diamine. The reactions of the primary amine and anhydride were fast enough to be completed during a typical processing time. The unequal reactivity of the primary secondary diamine resulted in a grafted secondary amine group and greatly reduced branching. The structures of amino functionalized polyethylenes were characterized by NMR and FTIR spectroscopies, Kaiser test, gel content measurement and rheology. Both amino functionalized polymers showed remarkably strong adhesion toward TPU, whereas almost no adhesion was found between TPU and PE homopolymers and only modest improvement with PE-*g*-MA.. There was no significant difference in the adhesive strengths between primary and secondary amino functionalized polyethylenes.

CHAPTER 3

Flow Accelerates Adhesion between Functional Polyethylene and Polyurethane

3.1 OVERVIEW

Polyethylene (PE) has relatively poor adhesion with polar polymeric materials. In an effort to improve the adhesion between PE and thermoplastic polyurethane (TPU), maleic anhydride (MA), hydroxyl (OH), and secondary amine (NHR) functionalized PEs were synthesized via reactive extrusion and blended into non-modified PE. We bonded these PEs to TPU via lamination and coextrusion. To compare the two processes, we determined the interfacial copolymer density Σ considering both advection and interfacial area generation. We found that the development of adhesion in coextrusion was much faster in comparison with lamination at the same temperature. This difference was attributed to the extensional and compressive flow in coextrusion overcoming the diffusion barrier at the interface and forcing reactive species to penetrate into interface. The effects of functional group reactivity and processing variables on adhesion were quantitatively correlated with interfacial copolymer coverage. Amine functionalized PE showed dramatic adhesion improvement even at 1 wt %.

3.2 INTRODUCTION

Adhesion between two immiscible polymers is usually very weak because there is little entanglement across the interface.[16-18] Adhesion can be enhanced by adding a compatibilizer that is capable of staying at the interface and entangling with both sides.

Reproduced in part with permission from J. Song, R. H. Ewoldt, W. Hu, H. C. Silvis and C. W. Macosko, "Flow Accelerates Adhesion Between Functional Polyethylene and Polyurethane", AIChE J. (2011), DOI: 10.1002/aic.12551.

This kind of "stitching"[3-5] can be created by at least three methods: 1) adding premade block copolymers; 2) adding a tie layer, a third polymer which is at least partially miscible in each of the immiscible polymers; 3) forming copolymers *in situ* via coupling reactions at polymer-polymer interfaces. Premade copolymers tend to embed in the bulk phases, reducing the concentration of copolymers available in interfaces. A tie layer always requires a separate layer of a third component. Interfacial coupling reactions, have some advantages over the other two methods: 1) most of the copolymers formed stay at the interface; 2) coupling reactions can link many homopolymer pairs for which the complementary block copolymer synthesis is not available; 3) they also give processing simplicity as there is no need for a third layer.

Most studies of adhesion have focused on glassy or semi-crystalline polymers and only a few involved elastomers.[3-5,16,17] However, in practice, there is much interest in combining the properties of elastomers through adhesion, for example, polyethylene (PE) elastomers which have excellent extensibility, flexibility and low cost, and thermoplastic polyurethanes (TPU) which have high elasticity, abrasion resistance and impact strength. Using the coupling reaction strategy, adhesion to polyurethane substrates can be improved using a polyolefin with functional groups that can react with urethane linkages.[48,50] For example, Lu *et al*. found that adhesion between TPU and polypropylene (PP) was greatly promoted by secondary amine-functionalized PP, whereas almost no adhesion was found between TPU and PP homopolymers and only modest improvement with maleic anhydride functionalized PP.[43]

In this research, we grafted maleic anhydride (MA), hydroxyl (OH) and secondary amine (NHR) functional groups onto ethylene/1-octene random copolymers through a continuous reactive extrusion process. We measured the peel strength of the functional PEs bonded to TPU through lamination and coextrusion. Our goal is to understand the effects of reactivity of functional groups and processing variables on adhesion. We compare lamination and coextrusion at the same reaction time and temperature and, remarkably, we find coextrusion builds adhesion faster.

3.3 EXPERIMENTAL

3.3.1 Materials

Ethylene/1-octene random copolymer (ENGAGE^{TM}8200), LLDPE-1, was provided by The Dow Chemical Company. This copolymer has 7.3 mol% octene with a melt flow rate (MFR) of 5.0 dg/min as measured by ASTM D 1238 and density of 0.870 g/cm^3 as measured by ASTM D 792. The anhydride-functionalized ethylene/1-octene copolymer (PE-MA) was prepared by free radical grafting of maleic anhydride onto another ethylene/1-octene copolymer LLDPE-2 (ENGAGE™8407) in the melt using continuous reactive extrusion described in detail elsewhere.[42] This ethylene/1-octene copolymer (ENGAGE™8407) has 7.3-7.7 mol% octene with a melt flow rate (MFR) of 30 dg/min and density of 0.870 g/cm^3. The MFR of PE-MA was ~5 g/10 min and the anhydride content was determined to be 0.75 wt% by a calibrated FT-IR analytical method. 0.75 wt% corresponds to about one succinic anhydride group per 1000 -CH_2- units on the polyolefin backbone. The hydroxy- and amino-functional analogs were then prepared directly from PE-MA by reactive extrusion with 2-aminoethanol and N-methyl-1,3-propanediamine as described by [42]. The relative concentrations of OH and NHR functionalities, N-(2-hydroxyethyl)-succinimide and N-(3-(N-methylamino)-1-propyl)-succinimide were 1.08 wt% and 1.28 wt%, respectively, based on complete conversion of the anhydride to functionalized imide as determined using FT-IR spectroscopy (anhydride C=O at 1790 cm^{-1}; imide C=O at 1705 cm^{-1}). Due to crosslinking side reactions, the MFR dropped to ~5 g/10min after grafting with maleic anhydride, however, the density and octene content were essentially unchanged. Conversion of MA to OH or NHR did not alter the MFR any further. The structures of LLDPE-1 and functional PEs are given in Figure 3.1.

TPU (Avalon® 70 AE) with polyester soft segments was provided by Huntsman Polyurethanes. It has a number average molecular weight of 77.5 kg/mol and PDI 1.7 based on polystyrene standards (EasiCal PS-2, Polymer Laboratories) as determined by size exclusion chromatography (SEC, Waters 717 Plus HPLC Autosampler) at room

temperature using tetrahydrofuran (THF) as a mobile phase. Key properties of PEs and TPU are listed in Table 3.1.

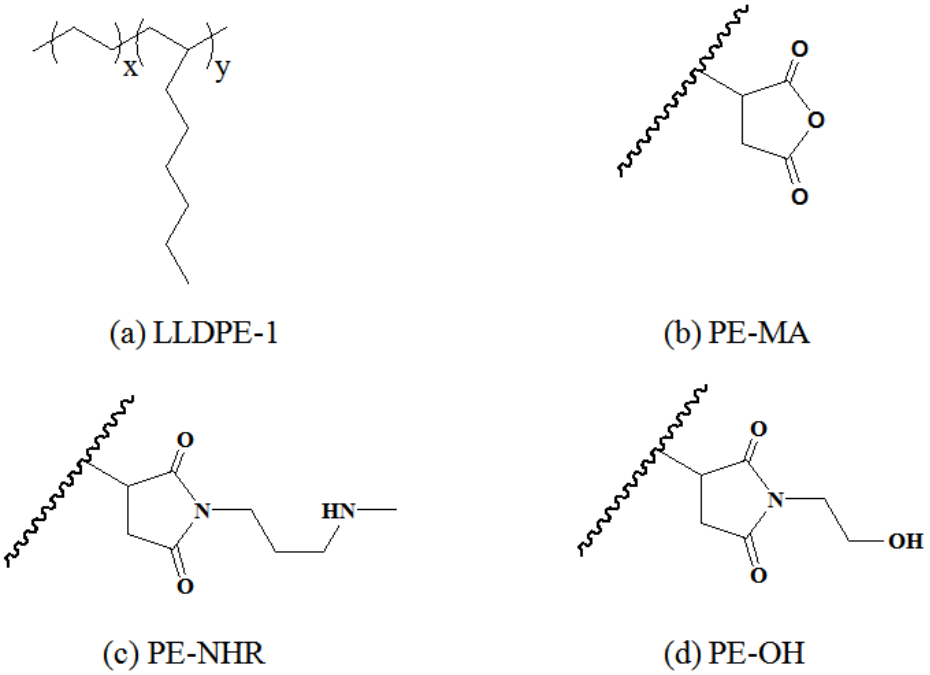

(a) LLDPE-1 (b) PE-MA

(c) PE-NHR (d) PE-OH

Figure 3.1 Structures of the functional polyethylenes used in this study. (a): LLDPE-1 (ethene/1-octene random copolymer; x/y=93/7); (b): Succinimide grafted polyethylene (PE-MA); (c):N-(3-(N-methylamino)-1-propyl)-succinimide grafted polyethylene (PE-NHR); (d): N-(2-hydroxyethyl)-succinimide grafted polyethylene (PE-OH). Wiggly chains in (b), (c), (d) represent ethene/1-octene random copolymer backbones.

Table 1. Key properties of PEs and TPU

	LLDPE-1	PE-MA	PE-OH	PE-NHR	TPU
T_m (°C)	67	66	67	67	152
Crystallinity (%)	9.4	8.3	8.8	8.5	-
Density (g/cm^3)	0.87	0.87	0.87	0.87	1.21
Viscosity[a] (Pa·s)	7.1×10^2	-	-	-	9.4×10^2

a: Dynamic viscosity at frequency equal to the apparent wall shear rate at the die exit, 50/s.

TPU pellets were dried overnight in a conventional static oven at approximately 70 ℃ to remove residual moisture before compression molding and coextrusion. The viscosities were measured at 180 °C under N_2 atmosphere by a strain controlled rotational rheometer (ARES, TA Instruments) using 25 mm parallel plates. Differential scanning calorimetry (DSC) measurements were performed with TA Instruments DSC Q1000. Approximately 10 mg of dry polymers were loaded into non-hermetic aluminum pans. DSC scans were performed at the rate of 10 °C/min from -100 to 250 °C. Melting temperature was determined from the first scanning cycle using TA Instruments Universal Analysis 2000 software. Dynamic viscosity values at 180 ℃ for TPU and all the functional PE/LLDPE-1 blends were similar, within ± 10%, over the frequency range 10-100 rad/s.

3.3.2 Melt blending

LLDPE-1 and functional PEs were blended with a 16 mm co-rotating twin-screw extruder (Prism Engineering, Staffordshire, England) at 100 rpm. This extruder has a length-to-diameter ratio of 25 and five temperature control zones and a mixing screw configuration with three kneading elements and one backflow element.[51] The barrel temperatures from hopper to die exit were set at 100 ℃, 130 ℃, 165 ℃, 180 ℃, and 180 ℃. The extruded functional PE/LLDPE-1 strand was cooled in an ice water bath and pelletized. All samples were dried at ambient condition for at least one week before use.

3.3.3 Lamination and T-peel test

Functional PE/LLDPE-1 and TPU films (80mm×7.5mm×0.4mm) were prepared by compression molding from pellets at 120℃ and 180 ℃ respectively under 2 MPa between two polytetrafluoroethylene (PTFE) coated aluminum foils (Saint-Gobain Performance Plastics). Functional PE/LLDPE-1 and TPU films were dried in vacuum oven at room temperature and 70^{o}C respectively. After drying under vacuum, TPU and functional PE/LLDPE-1 films were pressed into intimate contact sandwiched within two PTFE coated aluminum foils and annealed for various time at 180 ℃ under 0.1 MPa within a rectangular mold (80mm×7.5mm×0.75mm).

Immediately after annealing, bilayer samples were quenched by plunging into ice water. The edges of bilayer samples were trimmed with a razor blade and T-peel tests were conducted 24 hours after lamination. A MINIMAT tensile tester (Rheometric Scientific) with an extension rate of 1 mm/s was used to peel the bilayer. Peel strength was defined as the ratio of the median plateau value of peeling force (F) over peeling arm width (b). At least three samples were tested for each experimental measurement and the mean values as well as the standard deviations were calculated. To generate more flow during melt lamination, a pair of thicker layers (0.6 mm instead of 0.4mm) were squeezed down to 0.75mm.

3.3.4 Coextrusion

The functional PE/LLDPE-1 and TPU bilayer samples were prepared by coextrusion at 180 ℃ through dies shown schematically in Figure 3.2. TPU was delivered by a single-screw extruder to a gear pump (Zenith PEP-II), which controlled the flow rate to the feedblock. Compounded functional PE/LLDPE-1 pellets were fed by the 16 mm twin-screw extruder. Functional PE/LLDPE-1 and TPU were extruded at equal flow rate. A detailed description of the coextrusion line can be found in the literature.[18,39,52,53] Based on the continuity equation, melt velocity in the coextrusion dies can be deduced from the chill roll speed and film thickness. At a total flow rate of 38.4 cm^3/min as determined from calibrated gear pumps, the average linear velocity of the

polymer melt in the die land was about 10 mm/sec. Thus, the residence time in the sheeting die and die land was less than 10 sec. Upon exiting the die land, bilayer films were drawn by chill rolls at 4 ℃. The temperature of molten polymer was measured by an infrared thermometer (Omega Engineering, Inc.). The die exit has dimension of 50mm×1.2mm. The thickness of bilayer samples varied from 0.4mm to 1 mm depending on take-up velocities of the chill rolls. T-peel tests on coextruded films were conducted by using the same procedure as described in the previous section.

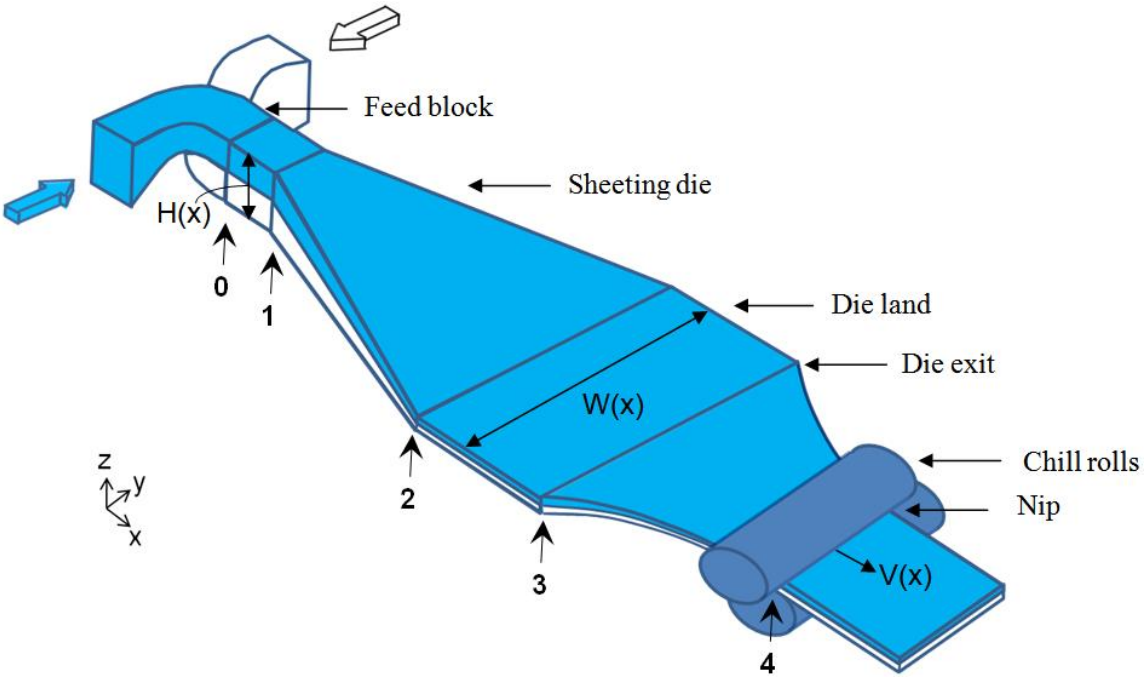

Figure 3.2 Schematic of polymer melt flowing through the coextrusion die followed by draw down from the die exit by the chill rolls.

3.4 RESULTS AND DISCUSSION

3.4.1 Lamination

A typical plot of peel strength versus crosshead displacement is shown in Figure 3.3. During a T-peel test, one end of a bilayer specimen is fixed while the other end is pulled away at 180^o by a moving grip at a constant velocity. Peel strength was determined by taking the average of all F/b values starting from the onset of peeling. In Figure 3.4, adhesion strength, F/b, is plotted versus functional group type, functional PE content and annealing time for laminated bilayers.

Lu *et al*. have shown that at high temperature the urethane linkage in TPU dissociates to generate isocyanate, which can react with various functional groups.[48] Since functional groups are randomly distributed along the backbones of the functional PEs, the coupling reaction between TPU and functional PEs are expected to form graft copolymers. In order to better understand adhesion properties of functional PEs, the reaction rate between chain coupling is expressed in terms of Σ, the number of copolymer chains per interfacial area:

$$\Sigma = \nu t \qquad \text{(Equation 3.1)}$$

where ν is the effective two-dimensional coupling reaction rate in the interface (chains/s/m^2), t is reaction time (s). Σ can be evaluated from a T-peel test.

In a T-peel test, G_a, the fracture energy per unit crack propagation length, can be calculated by using the following energy analysis:[54,55]

$$G_a = \frac{F}{b}(1 + \varepsilon_a - \cos\theta) - h\int_0^{\varepsilon_a} \sigma d\varepsilon - G_{db} \qquad \text{(Equation 3.2a)}$$

where F is peeling force, b is the peeling arm width, h is the peeling arm thickness, ε_a is strain in the peeling arms, θ is peeling angle (90^o for T-peel test), σ is the stress at the cross-section of the peeling arm, and G_{db} is bending energy. G_{db} is negligible for the thin flexible films made from the low modulus elastomers used in this research. When there is negligible change on peeling arm width, $\frac{F}{b}\varepsilon_a \approx h\int_0^{\varepsilon_a} \sigma d\varepsilon$. Based on this analysis,

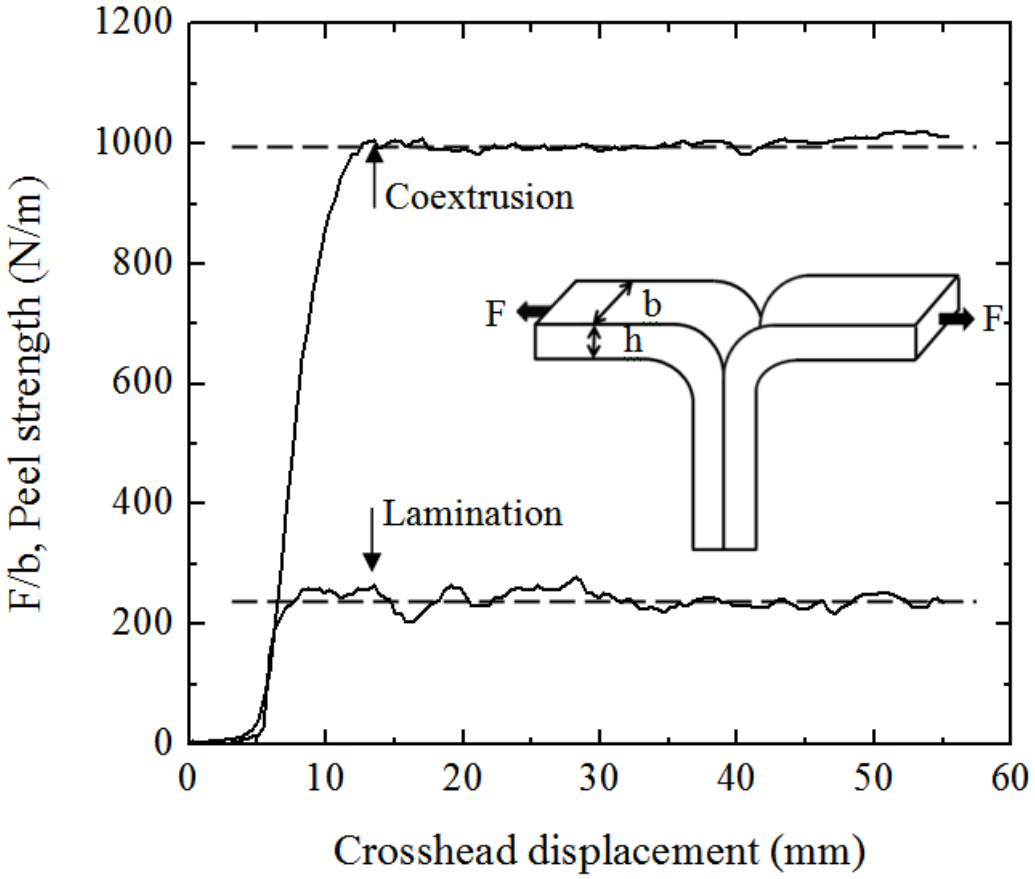

Figure 3.3 Peel strength, F/b, vs. crosshead displacement for T-peel tests of 3 wt% PE-NHR /TPU bilayers. Dashed line represents the median plateau values of bilayers with 30 seconds reaction time for lamination and residence time of 10 seconds for coextrusion. A schematic drawing of the T-peel test is also shown where b and h denote the peel arm width and thickness respectively, and F is the peeling force.

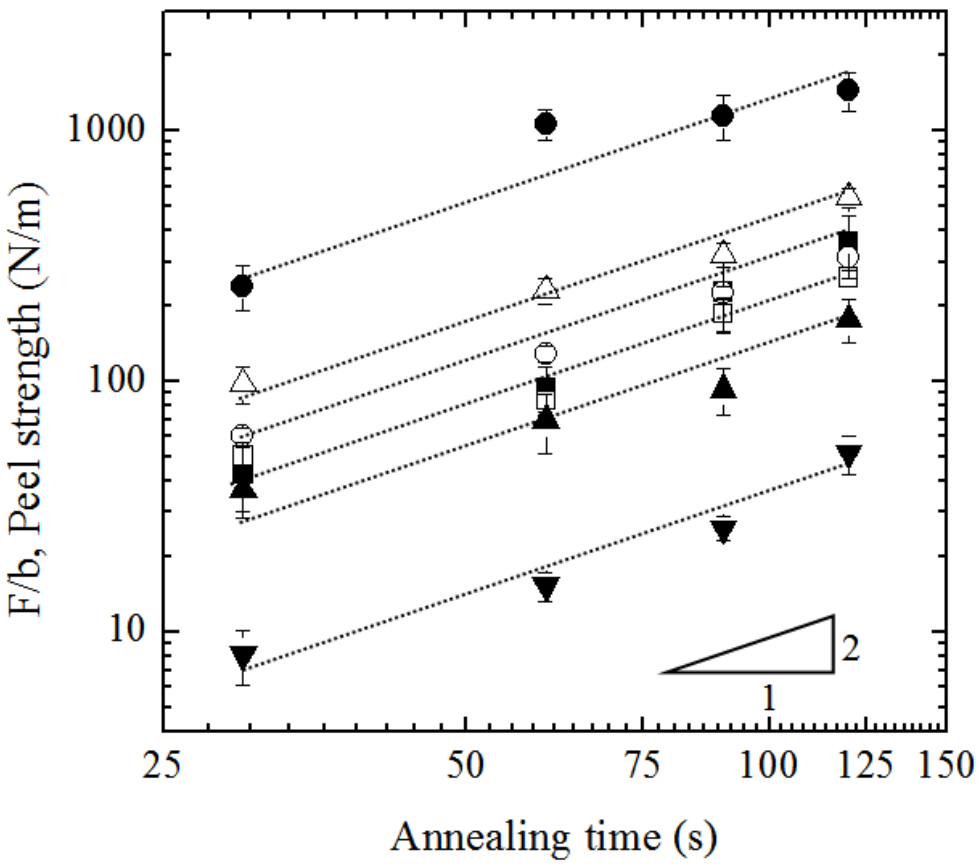

Figure 3.4 Peel strength, F/b, of laminated bilayers vs. content of incorporated functional PE and annealing time. ■, ●:1 and 3wt% PE-NHR; ▼, ▲: 3 and 10 wt% PE-OH; □, ○, △:10, 20 and 30 wt% PE-MA. Error bars represent standard deviation of three to six tests. The solid lines are used to guide the eye.

Equation 3.2a simplifies to $G_a = \frac{F}{b}$. G_a can be related to G_c, the critical energy release rate,[56] which is the intrinsic material toughness, by

$G_a = G_c(1+\Phi(\dot{\varepsilon}, T))$ (Equation 3.2b)

where Φ is a function of peeling rate $\dot{\varepsilon}$, and temperature T. Combining Equation 3.2a and 2b gives

$\frac{F}{b} = G_c(1+\Phi(\dot{\varepsilon}, T))$ (Equation 3.3)

Thus when T-peel tests are conducted at constant peeling rate $\dot{\varepsilon}$ and temperature T, F/b is proportional to G_c.

In Figure 3.4 for the same type of functional PE, peel strength, F/b, increased with the amount of functional PE and annealing time. Log peel strength (F/b) vs. log annealing time has a slope of ~2. Since by Equation 3.1 areal density of chains, Σ, is proportional to reaction time, t, then F/b is proportional to Σ^2. Therefore, F/b values can be used to monitor copolymer conversion at the polymer-polymer interface. Then Equation 3.3 gives that G_c is proportional to Σ^2. G_c is a linear function of Σ if the interface failure occurs by simple chain scission or chain pull-out without any extensive plastic deformation, while it scales with Σ^2 if the applied interfacial stress is sufficient to activate plastic deformation of a small volume at the crack tip.[17,57] For elastomers, G_c includes the energy to break the intrinsic interfacial bonding and also the energy dissipated locally ahead of the peel front at the crack tip.[55] Clearly, the grafted copolymers generated via coupling between TPU and functional PEs were able to entangle across their interfaces and provide high adhesion strength. When peel strength value F/b exceeded 500 N/m, plastic deformation of peeling arms was observed. Although there is no simple relationship correlating peel strength F/b and critical energy release rate G_c when there is significant plastic deformation,[58,59] it is the increase of chain density Σ that leads to increased peel strength.

To understand the effect of reactive species concentration on interfacial coupling reaction rate, we varied the concentration of functional PEs. ν, reaction rate in the interface, as defined in Equation 3.1, can be determined as follows:

$$\nu = kC_X^a \lambda \qquad \text{(Equation 3.4)}$$

where k is the usual three-dimensional reaction rate coefficient, C_X is the volumetric density of grafted functional groups at the interface, a is the reaction order, λ is the coexistence thickness at the interface (the effective distance over which the reactive groups can interact). The bulk concentration of urethane groups is at least 100 times higher than that of grafted functional groups on functional PEs. Therefore, urethane concentration can be considered constant and C_X is the concentration of functional groups on the PEs. $F/b \sim \Sigma^2$ gives $F/b \sim \nu^2$ such that we correlate peel strength with reaction rate. We found that the reaction order, a, was 0.95 for NHR, close to first order which might be expected for bimolecular collisions with a large excess of one reactant. However a decreased to 0.78 for OH and 0.45 for MA. These lower reaction orders may be due to the fact that the initial concentration of reactive species is higher in OH and MA grafted PE blends in contrast to NHR. This could lead to a more crowded interface making it more difficult for reactive species to penetrate into the interface.[60]

Almost no adhesion was found between PE and TPU. Among different functional PEs, moderate improvement was achieved by adding MA and OH modified PEs. Surprisingly, peel strength with only 3 wt% PE-NHR increased dramatically to F/b~1000 N/m within only 60 s annealing time, indicating a fast reaction between urethane linkages and secondary amine groups.

3.4.2 Coextrusion

Figure 3.5 shows that for coextruded bilayer samples, peel strength decreased with drawdown ratio, the ratio of velocity of polymer at the nip point of chill rolls over velocity of polymer at the die exit. The interfacial copolymer density, Σ, is calculated in order to understand the effect of drawdown on adhesion.

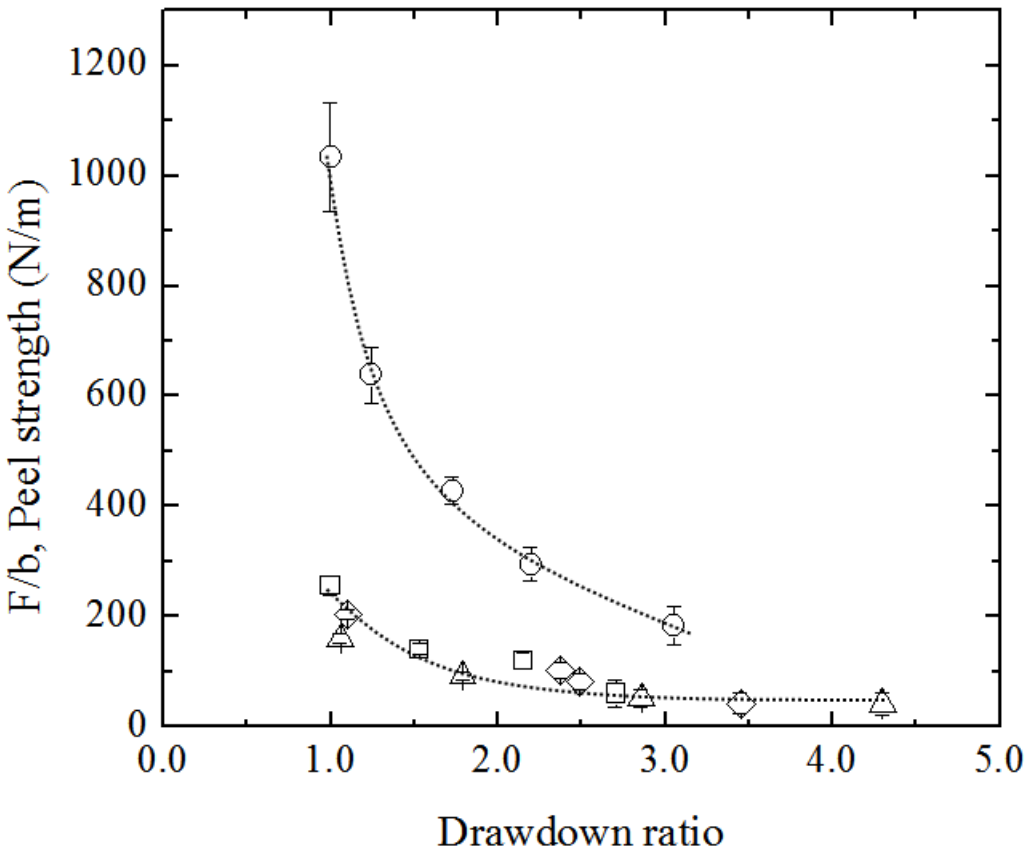

Figure 3.5 Peel strength vs. drawdown ratio for adhesion achieved by coextrusion at total volumetric flow rate Q = 38.4 cm^3/min. □, ○:1 and 3 wt% PE-NHR, △: 10wt% PE-OH, ◇:20wt% PE-MA. The solid line is used to guide the eye.

To calculate Σ, the region where reaction occurred must be determined. Figure 3.2 shows that the two molten streams started contacting each other at the beginning of the sheeting die. Copolymers were generated at the interface while the polymer streams flowed in the coextrusion die. Upon exiting the die, the temperature of the molten

polymer decreased very little < 5 ^{o}C, until it touched the nip point, due to the low thermal diffusivity of polymers and relatively high film velocity.[61] Thus the time polymer spends between the die exit and the nip was taken into account as part of the reaction time calculation. To check whether chill rolls are effective enough to quench interfacial reaction by reducing temperature, we solved the unsteady state energy balance.[62] By assuming an isothermal boundary at 4 ^{o}C, the time for the interface to be cooled below 60 ^{o}C (~100 ^{o}C lower than urethane dissociation temperature) is less than 0.5 s. We also observed that the temperature of coextrudate decreased to below 50 ^{o}C after it passed through chill rolls, indicating that the interfacial reaction was terminated. Thus, the interfacial reaction in a coextrusion line begins in the region where polymer streams start contacting and ends at the chill roll nip.

The copolymer number density Σ is affected by both the residence time and the change of interfacial area during coextrusion. In the absence of reaction, an increase in the interfacial area (dilation) would dilute the areal density Σ. We consider this aspect when calculating the resulting copolymer number density via coextrusion. The calculation in the appendix gives the following conservation expression, which is a balance between creation and advection,

$$\nu = V_x \frac{\partial \Sigma}{\partial x} + V_y \frac{\partial \Sigma}{\partial y} + \left(\frac{\partial V_x}{\partial x} + \frac{\partial V_y}{\partial y} \right) \Sigma . \qquad \text{(Equation 3.5)}$$

Here ν is the effective two-dimensional reaction rate defined in Equation 3.1, and V_x and V_y are the velocity at the interface in the flow- and spanwise-direction, respectively. The first two terms on the right hand side represent standard advection. The term in parentheses represents the dilation of the interfacial area due to stretching and cannot be neglected for this two-dimensional case (although in three-dimensions this term would equal zero for incompressible materials). Equation 3.5 is solved under the simplifying assumption of plug flow through the coextrusion die (e.g. perfect slip at the bounding walls):

$$\frac{\Sigma(x)}{\nu} = \frac{1}{Q} e^{-\int_0^x f(x)dx} \left\{ \int_0^x e^{\int_0^x f(x)dx} H(x)W(x)dx \right\} \qquad \text{(Equation 3.6)}$$

where ν has been factored out since it is an unknown constant, Q is the total volumetric flow rate through the die, $H(x)$ is the bilayer thickness in the *z*-direction and $W(x)$ is the spanwise width in the *y*-direction. The term $f(x)$ is the area dilation term

$$f(x) = \frac{1}{H(x)} \frac{dH}{dx}. \qquad \text{(Equation 3.7)}$$

The ratio Σ/ν represents the *effective* reaction time during the coextrusion process, which is a combination of the residence time and any interfacial area dilation which occurs. We use the definition of effective reaction time,

$$t_{eff} \equiv \frac{\Sigma}{\nu} \qquad \text{(Equation 3.8)}$$

as calculated via Equation 3.6, to show the effect of drawdown on adhesion and to compare coextrusion and lamination experiments.

Figure 3.6 shows the solution of Equation 3.6 for our coextrusion die for the draw down ratios used in Figure 3.5 for the PE-NHR samples. In section 0→1 and 2→3, since bilayer thickness H(x) and spanwise width W(x) do not change with x, Σ/ν simplifies to $\frac{\Sigma}{\nu} = \frac{H(x)W(x)x}{Q}$. Therefore Σ/ν is only a function of residence time and it increases linearly with position. In section 1→2 and 3→4, Σ/ν is affected by both the residence time and the interfacial area dilation. The interfacial area dilation is caused by the change of die dimension in section 1→2 and drawdown in section 3→4. In section 3→4, increasing drawdown ratio gives rise to reduced t_{eff}. This is due to the fact that faster drawdown not only leads to shorter reaction time but also increased interfacial area. Both lead to reduced interfacial copolymer density, thus weaker adhesion.

The coextrusion peel strength values in Figure 3.5 were plotted versus effective reaction time, Σ/ν in Figure 3.7. As we expect from the results in Figure 3.6 increasing drawdown ratio leads to shorter effective reaction time and hence decreased peel

strength. A similar phenomenon was observed by Morris,[63] where the peel strength between coextruded HDPE/Adhesive/EVOH films increased with process time.

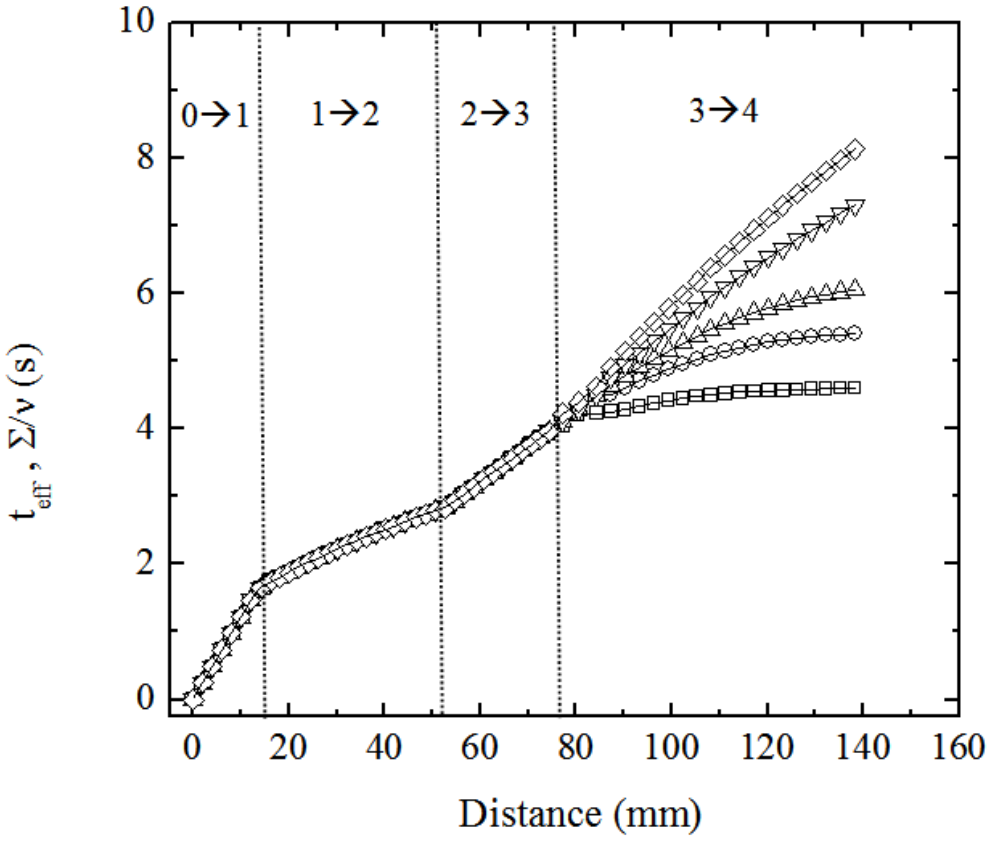

Figure 3.6 An illustrative solution for Equation (6), t_{eff} vs. distance for different drawdown ratios taken from Figure 5 for 3 wt% PE-NHR. The drawdown ratio values are as following ◇:1.02, ▽: 1.24, △:1.73, ○:2.19, □: 3.05. Section 0→1, 1→2, 2→3, and 3→4 correspond to the notation in Figure 3.2.

For the same functional PE, all the data follow a double-log slope of 2, which agrees with the fundamental correlation[17] $G_c \propto \Sigma^2$. It is also shown in Figure 3.7 that 1 wt% PE-NHR, 10 wt% PE-OH and 20 wt% PE-MA had similar reactivities while 3 wt% PE-NHR was much faster. This ranking agrees with the trend of lamination results in

Figure 3.4. Consequently, lamination tests can be used to rank the adhesion strength expected for coextrusion of the same polymers.

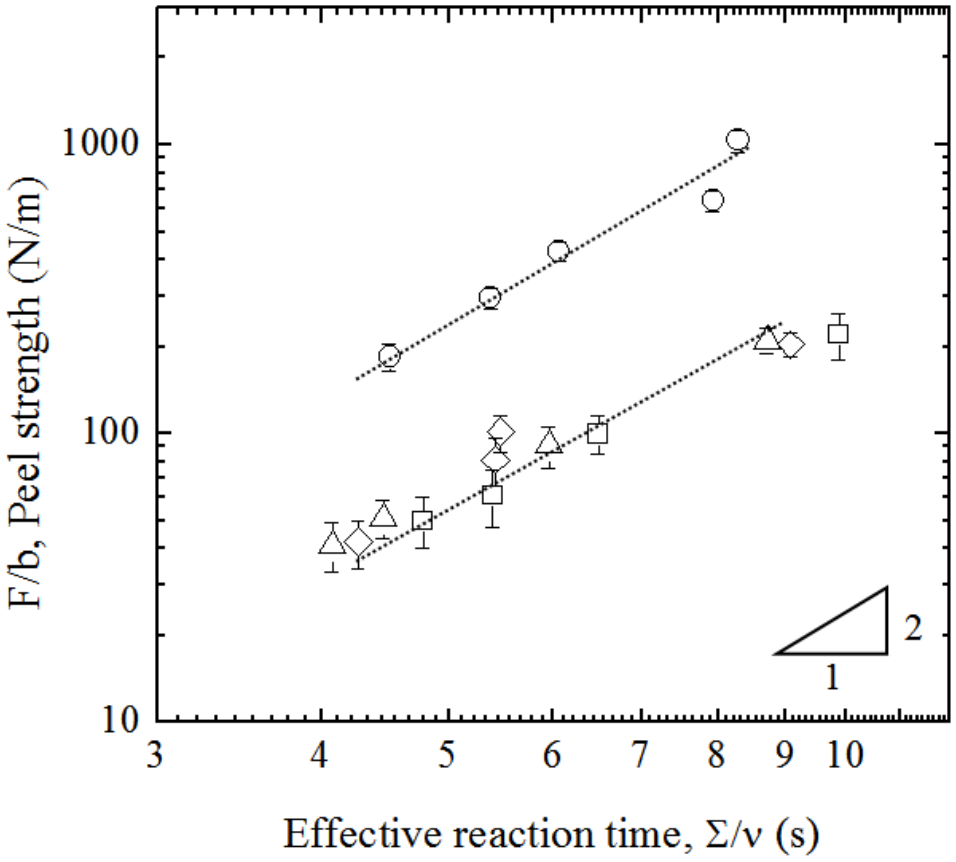

Figure 3.7 Peel strength data from Figure 3.5 plotted vs. effective reaction time, Σ/ν for adhesion achieved by coextrusion. □, ○:1 and 3 wt% PE-NHR, △: 10wt% PE-OH, ◇:20wt% PE-MA. The solid lines are used to guide the eye.

3.4.3 Reaction acceleration through coextrusion

For lamination, the annealing time in Figure 3.4 was considered to be effective reaction time, since it takes less than 0.5 s for the bilayer interface to reach the command temperature (the heat transfer calculation for lamination is analogous to that for the chill

rolls during coextrusion). For coextrusion, $t_{eff} = \Sigma / \nu$ was calculated according to Equation 3.6.Thus, peel strength vs. effective reaction time for both lamination and coextrusion are compared in Figure 3.8 (a) and 3.8 (b) for different functional groups. Figure 3.8 (a) shows that after 90 seconds of reaction for lamination, the interface of PE and TPU approached saturation with interfacial copolymers, i.e. peel strength approached a plateau value. While for coextrusion, it took only about 8 seconds to reach the same value (i.e. about one order of magnitude faster than lamination).

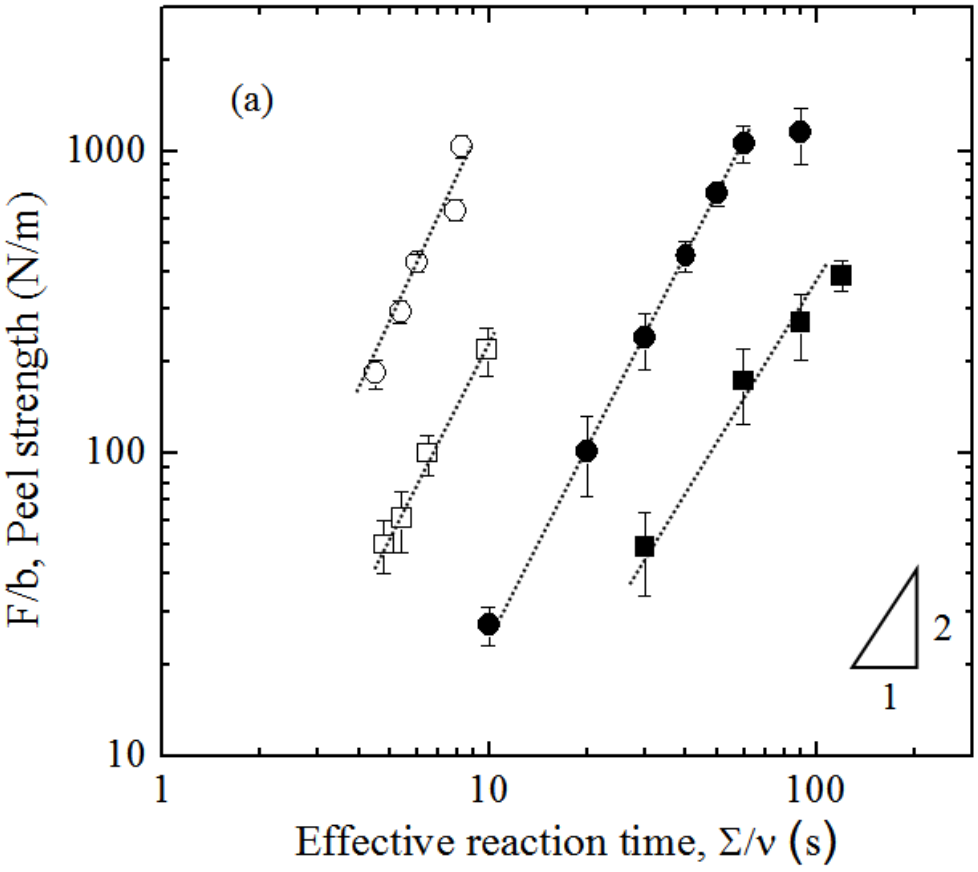

Figure 3.8(a) Peel strength comparison between lamination and coextrusion.

3 wt% PE-NHR: ○ (coextrusion), ●(lamination); 1 wt% PE-NHR: □ (coextrusion), ■ (lamination).

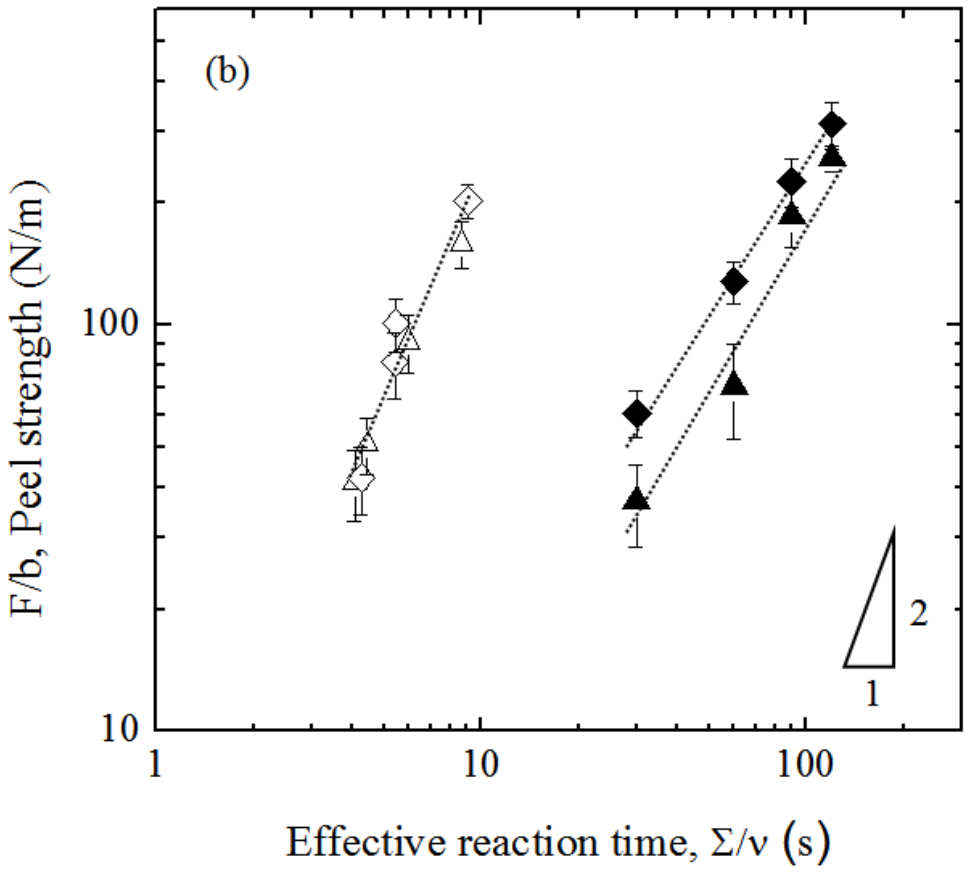

Figure 3.8(b). Peel strength comparison between lamination and coextrusion.
20 wt% PE-MA: ◇ (coextrusion), ◆ (lamination); 10 wt% PE-OH: △ (coextrusion), ▲(lamination).

It is apparent that the interfacial coupling reaction was greatly accelerated by coextrusion in comparison with lamination. As shown in Figure 3.8 (a) and (b), coextrusion accelerates the coupling reaction for all types of functional PEs. Similar phenomena were found in the literature where the coupling reaction between an amine-terminal polystyrene (PS-NH_2) and an anhydride-terminal polymethyl methacrylate (PMMA-anh) bilayer took about one hour for the interface to be saturated with block

copolymers, while when these two polymers were melt blended[11,28] or multilayer coextruded [8], it took less than one minute (i.e. about two orders of magnitude faster compared to quiescent annealing).

For the coextrusion experiments reported here, the reaction acceleration occurs during laminar flow without mixing. Furthermore, the interface is located in the middle of the die, where shear stress approaches zero. However, the interfacial plane does experience compression and extension during coextrusion, as do the bulk phases above and below the interface. As the molten polymer stream was converted from a square shape (10×10mm) into a rectangular shape (1.2×50mm) at the end of the fish-tail sheeting die, the interface of the bilayer experienced extensional strain (Hencky strain[64] ε_{Henky} = 0.95) in the machine direction (x), extensional strain (ε_{Henky} = 1.4) in the transverse direction (y) and compressive strain (ε_{Henky} = 2.3) in the z direction. Moreover, during draw down from the die exit to the nip, additional extension and compression were applied.

Under these compression/extension conditions, in the absence of shear or mixing, there are several possible causes of the increase of the interfacial reaction rate or the increase of the measured peel strength. These include induced crystallinity, enhanced diffusive flux of functional groups via compression of diffusion boundary layers, and increased concentration of functional groups in the interfacial region due to extensional and compressive flow in coextrusion. We will argue against crystallinity and show that enhanced diffusion alone cannot account for the dramatic increase in reaction rate. We therefore speculate that extensional and compressive flow in the coextrusion process contributes to the accelerated reaction rate during coextrusion.

Crystallinity is known to affect interfacial adhesion,[65,66] and this could increase the adhesive force even with constant copolymer reaction rate. We compared the crystallinity of laminated and coextruded functional PE/ LLDPE-1 blends and found that crystallinity was affected little by processing: 8-9% (pellets) and ~11% (coextrusion). The stress-strain curves were also the same for films produced by both lamination and coextrusion. Thus, crystallinity plays a negligible role in the observed increase in peel

strength and we must consider possible mechanisms for increasing the copolymer reaction rate.

We consider the general possibility of modifying diffusive flux or the local reaction process due to compressive flow normal to the interface. The absolute reaction rate is determined by the reaction-diffusion balance,

$$\nu = -D\frac{dC}{dz} \approx \frac{D(C_\infty - C_X)}{\delta} \qquad \text{(Equation 3.9)}$$

where ν is the two-dimensional coupling reaction rate in the interface, D is the diffusivity of the functional PE, C_∞ the volumetric density of grafted functional groups in the bulk, C_X is the volumetric density of grafted functional groups at the interface, and δ is the diffusion lengthscale. Assuming a=1 for bimolecular collisions, combining Equation 3.4 and 3.9 gives

$$\nu = \frac{DC_\infty}{\delta + \frac{D}{k\lambda}} \quad . \qquad \text{(Equation 3.10)}$$

Equation 3.10 gives the reaction rate in terms of both diffusion and local reaction parameters. Flow of the bulk phase material to the interface will modify the concentration profile of the reactive species. Compressing the layered sample normal to the interfacial surface: (i) decreases the diffusion layer δ, and (ii) may increase local reaction rate k by forcing polymer chains towards each other. Each mechanism will increase the reaction rate ν as shown by Equation 3.10. The relative importance of these two mechanisms is determined by the reaction being diffusion-limited or reaction-limited, i.e. the relative size of the terms in the denominator of Equation 3.10. We compared reaction rate to transport rate by calculating Damkohler number in the Appendix and found that although decreasing the diffusion length scale δ due to external mass transfer will increase the reaction rate, such increase of diffusive flux would be negligible for the reaction-limited process studied here.

We are therefore left to conclude that reaction acceleration was mainly caused by an increase in the local reaction process, and suggest that extensional and compressive flow in the coextrusion process gave rise to the reaction acceleration.

The interface between two immiscible polymers plays the role of an obstacle (or diffusion barrier) that hinders the diffusion of both reactive polymer chains to the interface for chemical reactions. Rafailovich[67] *et al*. found that the diffusion rate is one order of magnitude slower near an interface compared with in the bulk. We speculate that under coextrusion condition flow helps forcing reactive species to penetrate into interface and increases the concentration of reactive species in the interface.

Macosko *et al.*[34] found that flow resulted in a rate constant over 1000 times higher in heterogeneous melt blending than that in the quiescent bilayer reaction for an amine-terminal polystyrene (PS-NH_2) and an anhydride-terminal polymethyl methacrylate (PMMA-anh) system. Although a significant amount of interface was generated during blending, the rate constant was still ~ 300 times higher than that of quiescent bilayer reaction after normalizing by interfacial area.[7]Apparently, the complex flow under mixing accelerated interfacial reaction.

Zhang *et al.*[18] found that for a similar system, the reaction rate in coextrusion is comparable to that achieved in heterogeneous blending, as well as in homogeneous melt reaction, where the same functional groups were attached to PS chains and brought together to react. Apparently flow in coextrusion also accelerated interfacial coupling reaction compared to quiescent bilayer reaction without the presence of flow. Moreover, flow may help to stretch the polymer chains and expose the functional groups thus increasing the probability of reactive groups colliding with each other.

In this study, the reaction rate difference between coextrusion and lamination is less than that measured for the primary amine/anhydride functional polymers.[18] In the PS/PMMA system, functional groups tend to be depleted from the interface due to their high surface energy compared with that of the polymer backbones, leading to very slow coupling under quiescent conditions. However the polar TPU backbones may attract the polar functional groups into the interface, leading to faster reaction. Additionally, the

model study by lamination is different from quiescent reaction since some compressive flow is almost inevitable in lamination and flow accelerates interfacial reaction. Moreover, our functional groups are along the polymer chain, while Zhang *et al.*[18] observed the effect of extrusion acceleration of interfacial coupling with end functional chains and multilayer coextrusion.

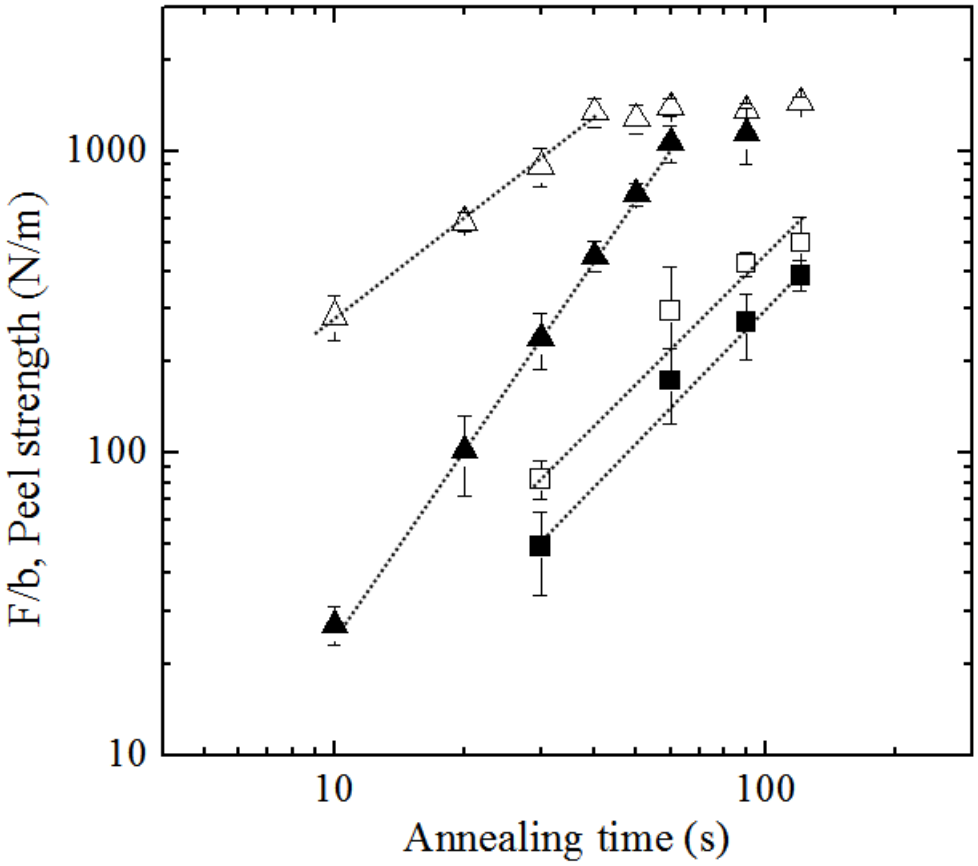

Figure 3.9 Peel strength comparison for lamination with different compressive strain. 3 wt% PE-NHR: △ (ε_{Henky} = 0.47), ▲ (ε_{Henky} = 0.06); 1 wt% PE-NHR: □ (ε_{Henky} = 0.47), ■ (ε_{Henky} = 0.06).

It should be noted that for the drawdown process in coextrusion, we find that increased chill roll velocity gave increased reaction rate because of flow and decreased effective reaction time due to dilation of interfacial area. It seemed that the latter one was dominant with respect to the effect of drawdown. However, the overall coextrusion process still resulted in reaction acceleration compared with lamination at the same temperature and reaction time.

In order to test the hypothesis that compressive deformation normal to the interface accelerates interfacial reaction, we repeated some lamination tests with more flow as shown in Figure 3.9. For 3 wt% PE-NHR and TPU, a Hencky strain of 0.47 gave much higher peel strength than a Hencky strain of 0.06 at the same annealing time. Thus, when a larger compressive strain was applied normal to the interface, more copolymers were generated at the interface. This effect is less pronounced for 1 wt% PE-NHR, presumably due to the lower concentration of functional groups at the interface. Note in Figure 9 for the 3% samples the difference between large strain and small strain compression decreases with annealing time. This is reasonable because there is no further flow during annealing after the initial compression.

Future studies can be designed to test the effect of compressive flow normal to the interface in contrast with compressive/extensional flow in the plane of the interface. This can be accomplished by modifying the current die design (Figure 2) in order to decouple these effects. Compressive flow normal to the interface can be generated by changing the height $H(x)$ while keeping width W=constant, in contrast to compression/extension in the plane of the interface caused by varying the width $W(x)$ while keeping height H=constant. Such tests would reveal the dependency of the reaction rate ν on the strength of the compressive flow $\dot{\varepsilon}$, and these results would be a guide to developing a more specific molecular theory to explain the increase in reaction rate observed in this study.

3.5 CONCLUSION

Adhesion between polyethylene and thermoplastic polyurethane was improved by blending functional PEs into non-modified PE. Direct measurements of interfacial

adhesion were obtained using a T-peel test. We investigated the influence of functional group type, annealing time, concentration of incorporated functional PEs and processing methods on interfacial adhesion. We were able to convert the effects of all these variables on adhesion to interfacial copolymer coverage. The ranking of adhesion strength of functional PE with TPU was determined as follows: NHR » OH ~ MA for both lamination and coextrusion processes. Particularly, amine functional PE showed dramatic improvement in adhesion with quite small incorporated amount. We also found increased adhesion strength with annealing time and concentration of incorporated functional PEs, as these effects resulted in increased interfacial copolymer coverage. Based on the calculation of interfacial copolymer coverage, reaction rates for two processes, lamination and coextrusion, were compared. Interfacial coupling reaction was found to be accelerated as much as an order of magnitude through coextrusion in comparison with lamination. We also found that the interfacial coupling rate in lamination could be increased by increasing the amount of compressive flow. This result is attributed to an increased concentration of functional groups in the interfacial region that results from the extensional and compressive flow in the coextrusion process forcing reactive species to penetrate into interface. Beyond its scientific significance, this work illustrates why coextusion is so successful for producing multilayer products within a very short residence time.

CHAPTER 4

Compressive Flow Accelerates Interfacial Coupling Reactions between Maleated Polyethylene and Nylon 6

4.1 OVERVIEW

We studied the processing flow effect on the kinetics of interfacial coupling reaction between maleic anhydride grafted polyethylene (PE-MA) and nylon 6. The NH_2 functional group at the end of nylon reacted with maleic anhydride on PE-MA and formed copolymers *in situ*. We found from lamination that adhesion increased with temperature and the concentration of PE-MA. The development of adhesion, characterized by G_c (critical energy release rate), as a function of Σ (interfacial copolymer density) was found to fall on the same master curve despite of different reaction process, temperature and time. G_c was a linear function of Σ for low Σ coverage and weak adhesion, while it scaled with Σ^2 when the applied interfacial stress was sufficient to activate local plastic deformation at the crack tip for relatively high Σ coverage.The reaction rate through coextrusion with a compressive/stretching die was strikingly two orders of magnitude larger than that through a stretching die. The latter rate was close to quiescent lamination. Even for lamination, when compressive flow was applied normal to the interface, the coupling reaction rate was also accelerated. Thus we determined that compressive flow accelerates the interfacial coupling reactions.

4.2 **INTRODUCTION**

Blending different polymers have been used to obtain desired properties superior to the single-component polymers. Most polymer pairs are thermodynamically

immiscible. As a result, they form two or more phases upon blending. Without additives, this interface is weak due to the lack of entanglements between both polymers.[16-18]

Coupling reactions between functional group grafted macromolecules have been proven to be a powerful way to facilitate compatibilization and adhesion. Compared with adding premade copolymers, interfacial coupling reactions, have some advantages: 1) most of the copolymers formed stay at the interface; 2) coupling reactions can link many homopolymer pairs for which the complementary block copolymer synthesis is not available.

Yet their reaction kinetics requires more fundamental understanding. Although many aspects of reactive blending[4,5,7,8,18,24,33,34,39,48,50,51,57,60,61,63,65-82] have been investigated by using quiescent bilayers including reactivity,[33] architecture,[7] molecular weight,[35] and concentration of functional polymers,[26] reaction kinetic under flow still remains to be a big challenge. The common wisdom for reactions between *small molecules* under flow is that external mass transfer increases the reaction rate by increasing concentration of reactive species without affecting reaction mechanism and transition states at a certain temperature. However, for reactions between *macromolecules* under flow, the kinetics is more complicated. It is generally difficult to study the effects of flow on macromolecules reactions during mixing because interfacial area generation and flow patterns are always convoluted and hard to isolate.

Coextrusion has been widely used to produce multilayer sheets.[36-38] It is a process in which two or more polymer layers are combined and extruded simultaneously. As the interface is well defined, coextrusion provides an ideal model system for studying interfacial phenomena such as inter-diffusion,[39] reaction,[18] and slip at polymer–polymer interface.[36,37] However, few studies were contributed to investigate how the interfacial reaction and adhesion depend on the flow conditions during processing. Zhang et al.[18] determined that the coupling reaction of amine terminal polystyrene (PS-NH_2)/anhydride terminal poly(methyl methacrylate) (PMMA-anh-anth) was up to 1000 times faster than that under quiescent annealing. For a different chemistry system, the coupling reaction between functional polyethylenes and polyurethane[83], we determined that the coupling

reaction rate through coextrusion was about one order of magnitude faster than lamination.

Shear flow was convoluted with compressive/extensional flow in multi-layer coextrusion. Although there are some studies[84-88] showing that the coupling reaction rate increases with the intensity of shear flow, shear is not the major concern of this study. In our research we eliminated shear by using bilayer coextrusion. We will show that compressive flow alone could accelerate coupling reactions dramatically.

In order to quantitatively relate the coextrusion conditions and the adhesion properties at interfaces, we have undertaken a systematic investigation of the kinetics of the grafting reaction of maleic anhydride modified PE (PE-MA) on nylon 6 as a function of the grafting temperature, both without flow (lamination) and with flow (coextrusion). We will compare the reaction rates under different flow conditions as achieved by bilayer coextrusion using a compressive/stretching die and a stretching die. A compressive/stretching die ensures that the interface is under compression/extension conditions and in the absence of shear or mixing. The compressive/stretching die gave rise to dramatic reaction acceleration when all the other parameters were controlled to be the same.

4.3 EXPERIMENTAL

4.3.1 Materials

Low viscosity general-purpose, extrusion grade nylon 6 (Ultramid B 27) was provided by BASF. It has a density of 1.13 g/cm^3, melt flow rate of 130 cc/10min (275 ℃/5 Kg), melting point of 220 ℃, Mn of 17 kg/mol and PDI of 2.0. This nylon 6 has nominally one NH_2 group at the end of each chain. All the data came from the material provider.

Maleic grafted polyethylene (PE-MA) was provided by Chemtura Co. with tradename Polybond 3029. It has a density of 0.96 g/cm^3, melt flow rate of 4g /10min (190 ℃/2.16 Kg), melting point of 130 ℃, Mn of 13 kg/mol and PDI of 5.8. The MA content is 1.6 wt%. PE-MA was blended into high density polyethylene (Dow HDPE 25455N) to study the effect of PE-MA concentration on adhesion. This HDPE has a density of 0.957 g/cm^3 and melting point of 129 ℃. nylon 6 and PE-MA pellets were dried overnight in a conventional static oven at approximately 70 ℃ to remove residual moisture before compression molding and coextrusion. The viscosities were measured at 230 ^{o}C under N_2 atmosphere by a strain controlled rotational rheometer (ARES, TA Instruments) using 25 mm parallel plates. Figure 4.1 shows that steady shear viscosity values at 230 ℃ for nylon 6 and PE-MA were similar, within ± 30%, over the rate range 10-100 s^{-1}. Figure 4.2 gives the dynamic frequency sweep of PE-MA at 230 ℃.

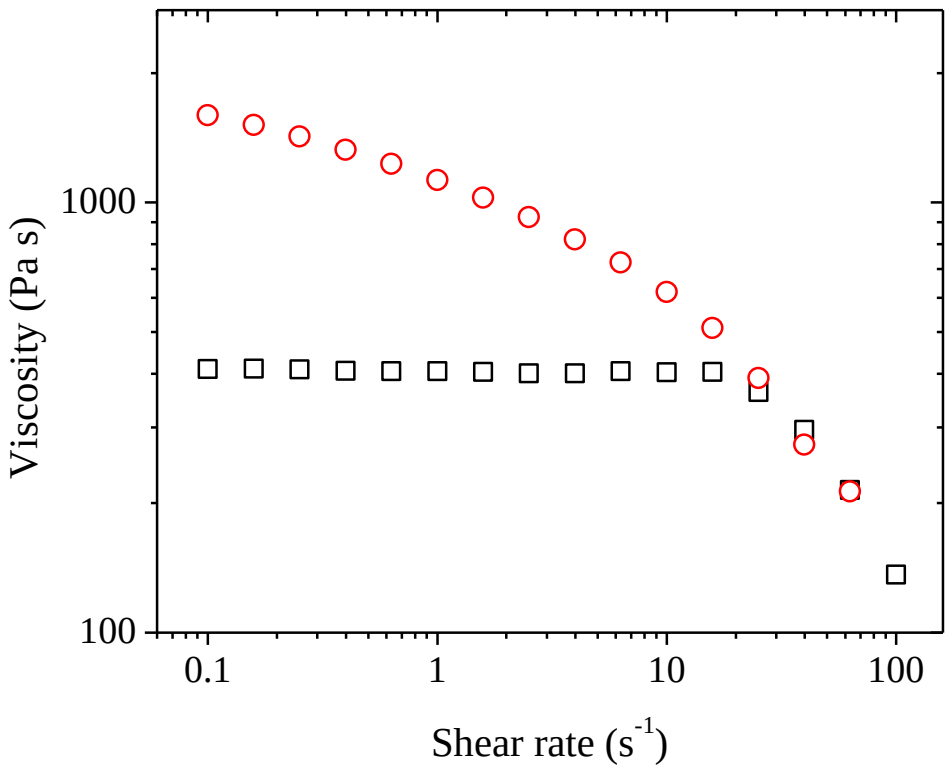

Figure 4.1 Steady shear test at 230 ℃. □: nylon 6; ○: PE-MA.

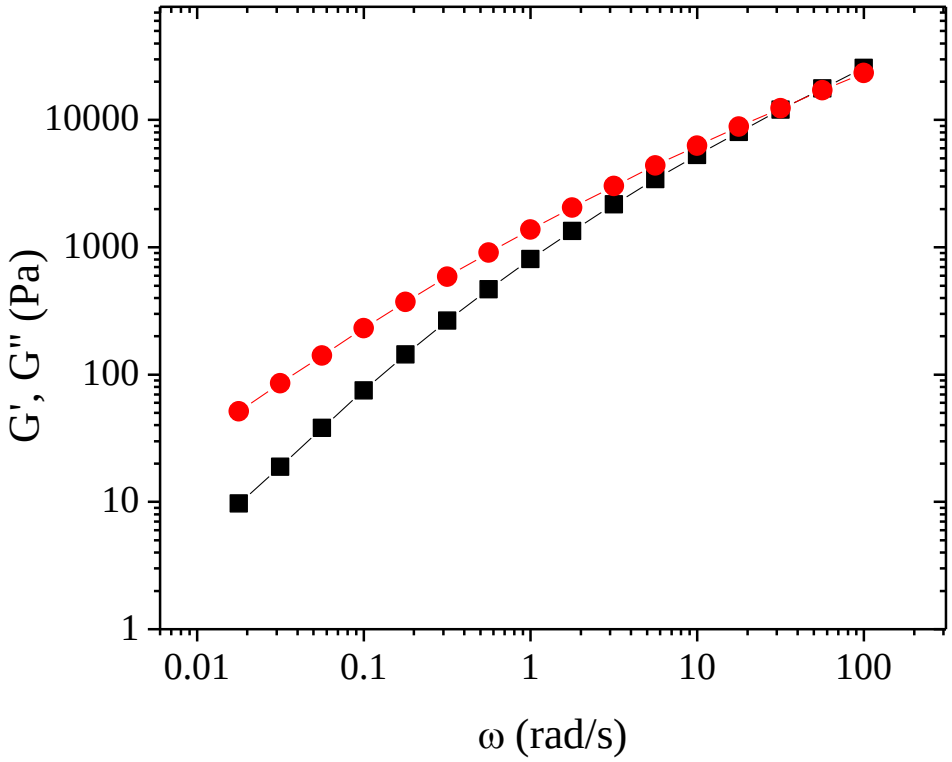

Figure 4.2 Dynamic frequency sweep of PE-MA at 230 ℃. ■: G'; ●: G''.

4.3.2 Coextrusion and lamination

The PE-MA and nylon 6 bilayer samples were prepared by coextrusion at 230 ℃ through dies shown schematically in Figure 4.3. In the compressive/stretching die (shown in Figure 3a), the interfacial plane experiences compression and stretching during coextrusion, as do the bulk phases above and below the interface. In the stretching die (shown in Figure 3b), there was no compressive flow since the thickness of the die was kept constant. Polymer melts were delivered by single-screw extruders to a gear pump (Zenith PEP-II), which controlled the flow rate to the feedblock. Two polymers were extruded at equal flow rate. A detailed description of the coextrusion line can be found in

the literature.[18,39,52,53] Based on the continuity equation, melt velocity in the coextrusion dies can be deduced from the chill roll speed and film thickness. At a total flow rate of 33.6 cm^3/min determined from calibrated gear pumps, the average linear velocity of the polymer melt in the die land was about 10 mm/sec. Thus, the residence time in the sheeting die and die land was less than 10 sec. Upon exiting the die land, bilayer films were drawn by chill rolls at 4 ℃. The temperature of molten polymer was measured by an infrared thermometer (Omega Engineering, Inc.). The die dimensions can be found in Table 4.1. The thickness of bilayer samples from the compressive/stretching die varied from 0.4 mm to 1.14 mm and the thickness from the stretching die varied from 0.6 mm to 1.5 mm depending on the take-up speed. The distance in the air gap was varied to obtain different reaction time. Adhesion tests as described below on coextruded films were conducted after 24 h.

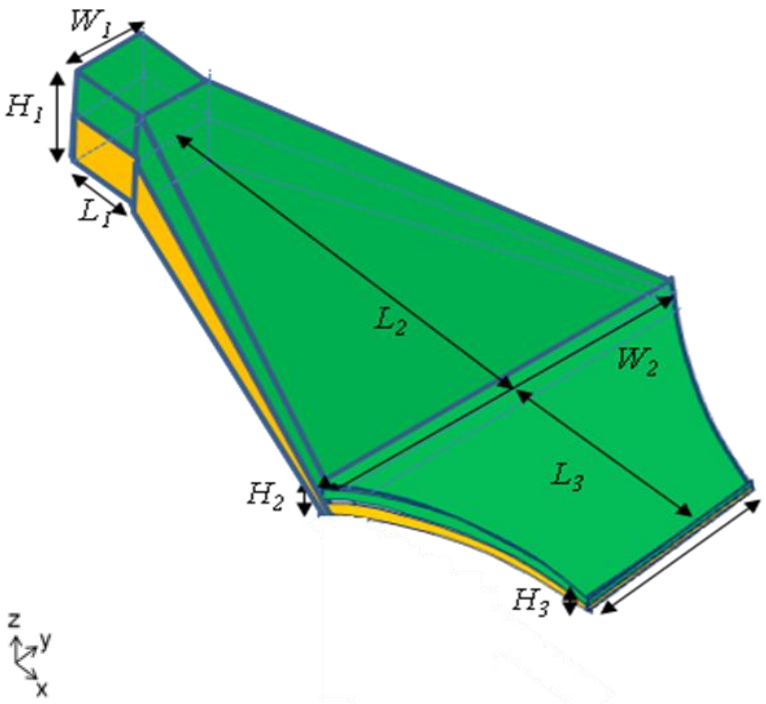

(a)

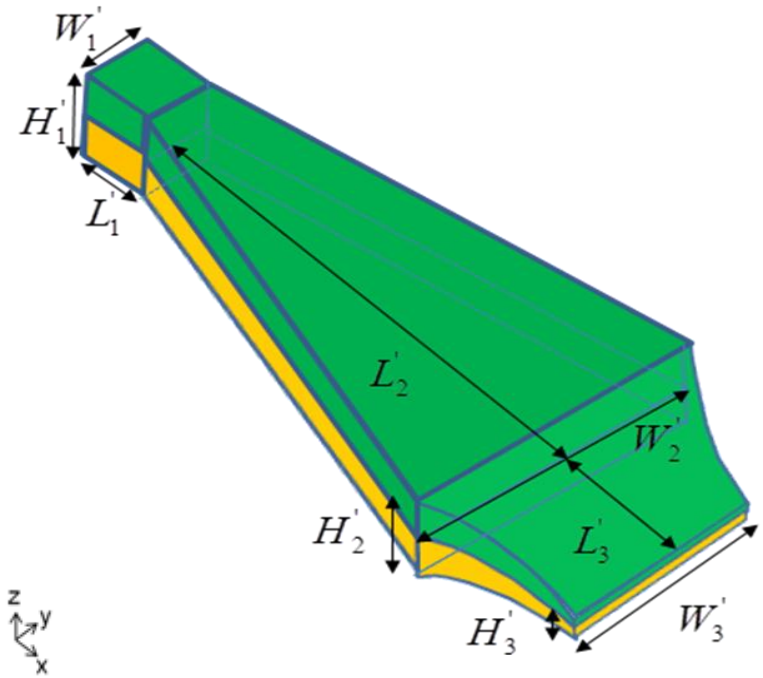

(b)

Figure 4.3 Schematic of polymer flow inside coextrusion dies and upon exiting the dies. (a) Compressive/stretching die. (b) Stretching die. Green and orange bulk parts represent nylon 6 and PE-MA layers respectively.

Table 4.1 Dimensions of the compressive/stretching die and stretching die

Compressive/stretching die	Value (mm)	Stretching die	Value (mm)
H_1	12.5	H_1'	12.5
H_2	1.2	H_2'	12.5
W_1	12.5	W_1'	12.5
W_2	50	W_2'	40.0
L_1	14.2	L_1'	14.2
L_2	33.5	L_2'	50.0

PE-MA/ HDPE and nylon films (80mm×7.5mm×0.4mm) were prepared by compression molding from pellets at 180℃ and 230 ℃ respectively under 2 MPa between two polytetrafluoroethylene (PTFE) coated aluminum foils (Saint-Gobain Performance Plastics). PE-MA/ HDPE and nylon films were dried in vacuum ovens at 80 ℃ and then they were pressed into intimate contact very gently and annealed for various time at 230 ℃ under 0.1 MPa within a rectangular mold (80 mm×7.5 mm×0.75 mm). Immediately after annealing, bilayer samples were quenched by plunging into ice water. The edges of bilayer samples were trimmed with a razor blade before adhesion tests.

To generate more compressive flow during melt lamination, a pair of thicker layers (0.6 mm instead of 0.4 mm) were squeezed down to 0.84, 0.6, 0.45, 0.36 and 0.19 mm to test the change of adhesion with various strain rates. After the initial squeezing at a speed of 10 mm/s, the bilayers were annealed for 10 seconds at 230 ℃.

4.3.3 Characterization

Adhesion measurement by ADCB (Asymmetric Dual Cantilever Beam) test

ADCB test has been shown to be a reliable method to determine the adhesion strength between stiff polymers.[23] A rectangular blade of thickness Δ is inserted into the interface of a double-layer sample to initiate a crack. After allowing the crack to equilibrate for a certain period of time, the crack length, a, can be measured from the crack front to the tip of the wedge. Optical microscopes are used for short crack length. The driving force for the propagation of crack comes primarily from the stiffness of the beams separated by the wedge and this driving force decreases as the crack propagates. Crack stops propagation when the release rate of elastic energy equals the energy needed to create a unit surface.

The critical rate of energy release has to be calculated in the proper limit. Since the crack length ahead of the blade, *a*, was less than $10h_{nylon6}$ for most of our samples, the following equation derived by Boucher et al.[17] was used. Kanninen[89] further assumed that the finite elasticity of the material ahead of the crack tip required correction for small crack length.

The critical fracture toughness or critical strain energy release rate (G_c) can be calculated using Equation 4.1 as follows: [23]

$$G_c = \frac{3\Delta^2}{8a^4} \frac{E_{PE-MA} E_{Nylon} h_{PE-MA}^3 h_{Nylon}^3}{E_{PE-MA} h_{PE-MA}^3 \alpha_{Nylon}^2 + E_{Nylon} h_{Nylon}^3 \alpha_{PE-MA}^2} \qquad \text{(Equation 4.1)}$$

where $\alpha_i = \left(1 + 1.92\frac{h_i}{a} + 1.22\left(\frac{h_i}{a}\right)^2 + 0.39\left(\frac{h_i}{a}\right)^3\right) / (1 + 0.64\frac{h_i}{a})$, E_i is the modulus of component *i*, and h_i is the thickness of the component *i*. (*i*=1, 2) The modulus and thickness of each layer, as well as the crack length, are required for the calculation of the critical mechanical energy release rate.

X-ray photoelectron spectroscopy (XPS) determination of interfacial copolymer density Σ

To determine the amount of copolymers formed at the interface, we used the method developed by Boucher et al.[90] The same nylon 6/ PE-MA bilayer samples on which Gc had been previously measured was put into excessive formic acid bath for at least 24 h. Although formic acid is a good solvent for nylon, free chains of nylon were linked by hydrogen bonds to the copolymer chains. In order to remove these free chains, rinsed PE-MA bulk samples were subsequently treated with trifluoroacetic anhydride in the gas phase to break the hydrogen bonding. The treated samples were then dissolved in dichloromethane to remove the free chains. Deionized water was then used to detach the trifluoroacetyl functional groups. Finally the treated samples were put into vacuum oven at room temperature with fresh surface upward and covered carefully to prevent

contamination. They were analyzed within 1 day to minimize contamination and oxidation of the grafted chains.

XPS measurements were performed on a Surface Science SSX-100 spectrometer using a focused monochromatic Al Ka anode (hv = 1486.6 eV) and a spot size of 800 μm. Electrostatic charging was neutralized by mounting a nickel grid about 2 mm above the sample surfaces. Accelerating voltage of 10 kV was used for data acquisition. After reflections corresponding to binding energies of C_{1s}, O_{1s} and N_{1s} were identified, higher resolution spectra were recorded for elemental quantification. The recorded spectra were adjusted to the C_{1s} peak of the saturated hydrocarbon bonds at a binding energy 286 eV. The elemental compositions were quantified from the peak areas using Wagner's sensitivity factors [91] and the spectrometer transmission function was taken into account. The parameters used for fitting were the peak area, the peak full width at half maximum, the position of the peak maximum, and the Gaussian–Lorentzian ratio. Σ can be calculated by using Equation 4.2:

$$\Sigma = -\frac{N_a \rho \lambda \sin\theta}{M_n} \ln\left(1 - \frac{I_N / I_C}{I_N^\infty / I_C^\infty}\right) \qquad \text{(Equation 4.2)}$$

where N_a is Avogadro's number, ρ the density of nylon 6, M_n its number-average molar mass, λ the mean free path of N 1s photoelectrons, and θ the takeoff angle. The escape length of the photoelectrons, $\lambda \sin\theta$, was estimated to be 19 Å using an experimentally determined relationship for escape length through hydrocarbon layers. I_C and I_N are the intensities of the carbon and nitrogen peaks on the analyzed sample surface, and I_C^∞ and I_N^∞ are the intensities of these peaks on a pure nylon surface. The ratio of I_C^∞ over I_N^∞ equals to 6/1 according the chemical structure of nylon 6.

We measured copolymer areal density Σ by XPS for each sample. Figure 4.4 shows typical XPS spectra of rinsed PE-MA surface after selectively dissolving nylon 6 following interfacial reactions. Figure 4.4 (a) exhibits a symmetric N_{1s} peak centered at 399.6 eV. Although for the grafted nylon chains, there are two different kinds of N: the

one next to carbonyl in the original nylon backbones and the one in the imide groups after reaction. Because of the low concentration of the N in imide, XPS only shows the first type. An asymmetric C_{1s} peak centered at 284.6 eV has a shoulder toward higher binding energy, indicating the presence of C=O in the nylon backbone.

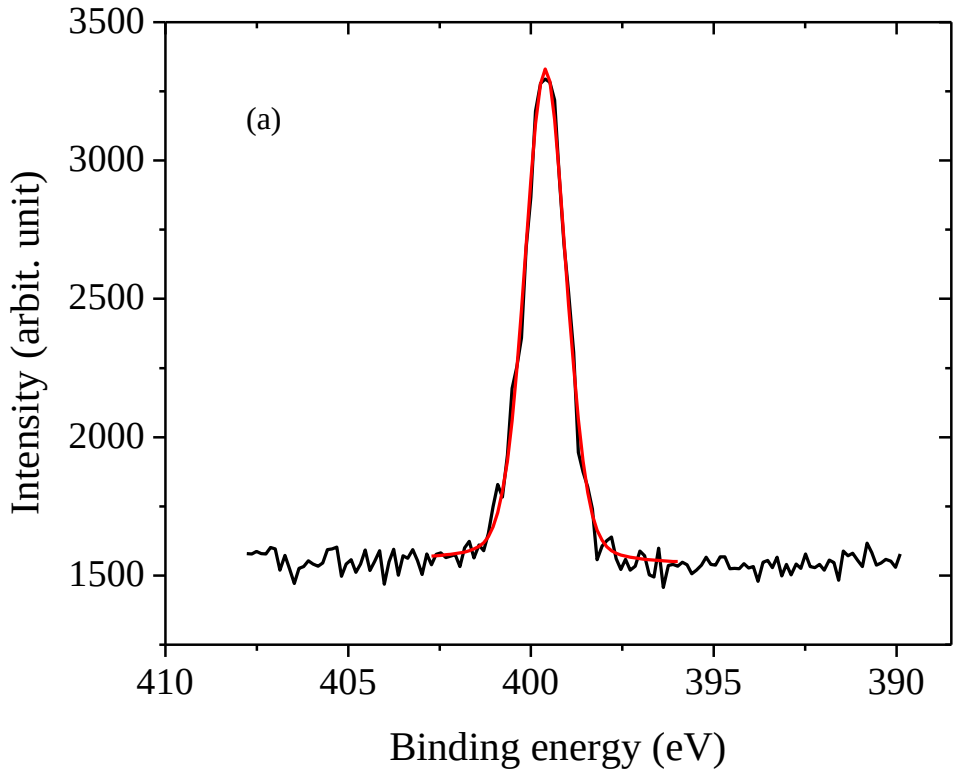

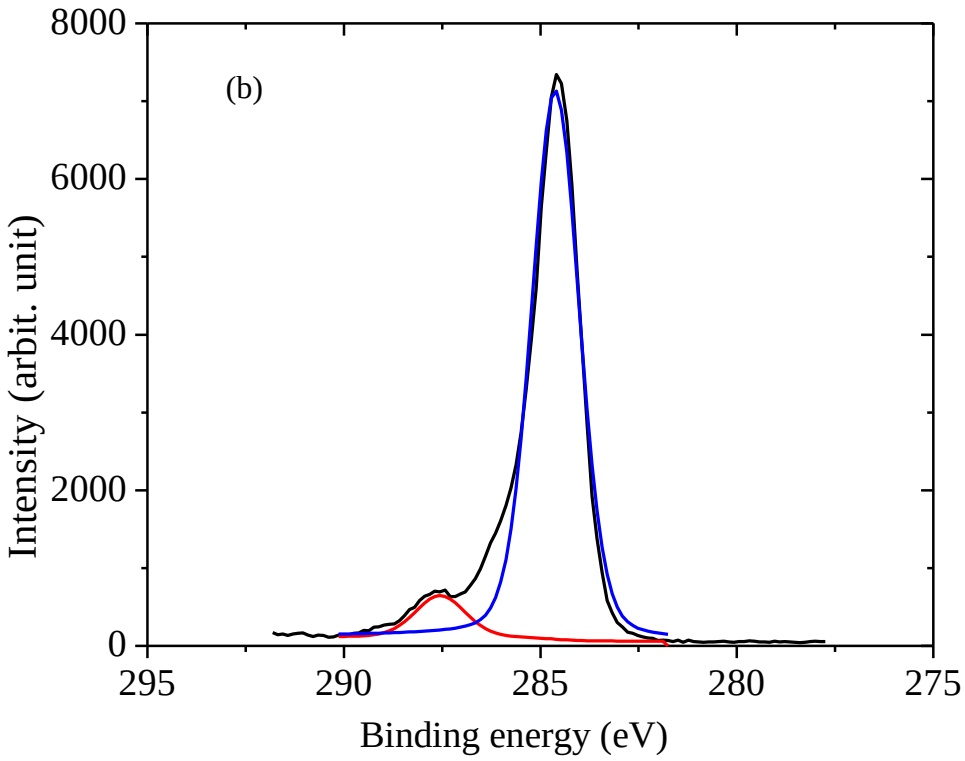

Figure 4.4 XPS spectra of rinsed PE-MA surface after selectively dissolving nylon 6 following interfacial reactions. This sample was obtained from coextrusion through the compressive/stretching die with 12 s reaction time. (a) High resolution XPS spectrum of Nitrogen (b) High resolution XPS spectra of Carbon (Black curves are original data; Colored curves represent deconvolution of the spectrum after curve fitting).

Wide-angle X-ray diffraction (WAXD)

Wide-angle X-ray diffraction (WAXD) intensity of cleaved surfaces was collected in a reflection mode with a Bruker-AXS microdiffractometer and CuKα radiation (45 kV and 40 mA). Samples are mounted on a 1/4 circle Eulerian cradle holder and analyzed in reflection mode at an incident angle of 2° to obtain structural information for a depth of a few micrometers from the surface.

Differential scanning calorimetry (DSC)

DSC measurements were performed with TA Instruments DSC Q1000. Approximately 10 mg of dry polymers were loaded into non-hermetic aluminum pans. DSC scans were performed at the rate of 10 ^{o}C/min from -100 to 250 ^{o}C. Heat flow vs. temperature curves were recorded from the first scanning cycle to compare the effects of processing conditions on crystallinity of nylon 6 andPE-MA. TA Instruments Universal Analysis 2000 software was used.

4.4 RESULTS AND DISCUSSION

4.4.1 The development of Σ and G_c and their correlations

We present an investigation of reaction kinetics at interfaces between maleic anhydride grafted polyethylene (PE-MA) and nylon 6, which has NH_2 functional groups at the end of each chain to react with maleic anhydride to form copolymers in situ.

The dependence of adhesion energy, G_c, versus the reaction time t for laminated nylon 6/PE-MA joints prepared at 230 ℃ is reported on Figure 4.5. G_c increases with the reaction time and the concentration of PE-MA as well. G_c is found to be directly proportional to the initial concentration of PE-MA (C_o) as shown in Figure 4.6. The adhesion increased rapidly with PE-MA concentration. As a result, for this system the adhesion can be predictably controlled through the concentration of PE-MA blended into the HDPE matrix. Figure 4.7 gives the development of Σ as a function of reaction time and temperature for lamination between nylon 6 and PE-MA. Obviously Σ built up much faster at 230 °C in contrast to 170 °C. At 170 °C, Σ shows a linear development with reaction time t, indicating a constant reaction rate at the initial stage of the coupling reaction.

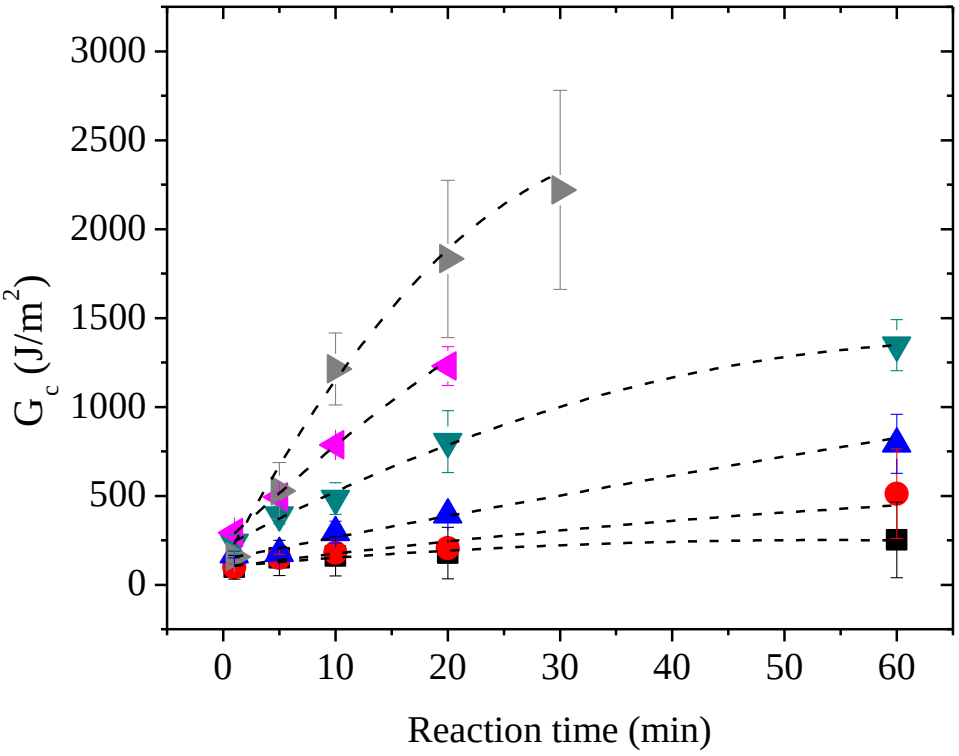

Figure 4.5 Critical energy release rate G_c development as a function of reaction time for adhesion between laminated nylon 6 and PE-MA/HDPE blend at 230 ℃. Concentration of PE-MA in the blends is listed as follows. ▶: 100 wt%, ◀: 80 wt%, ▼: 50 wt%, ▲: 20 wt%, ●: 10 wt%, ■: 5 wt%. Dashed lines are used to guide the eye.

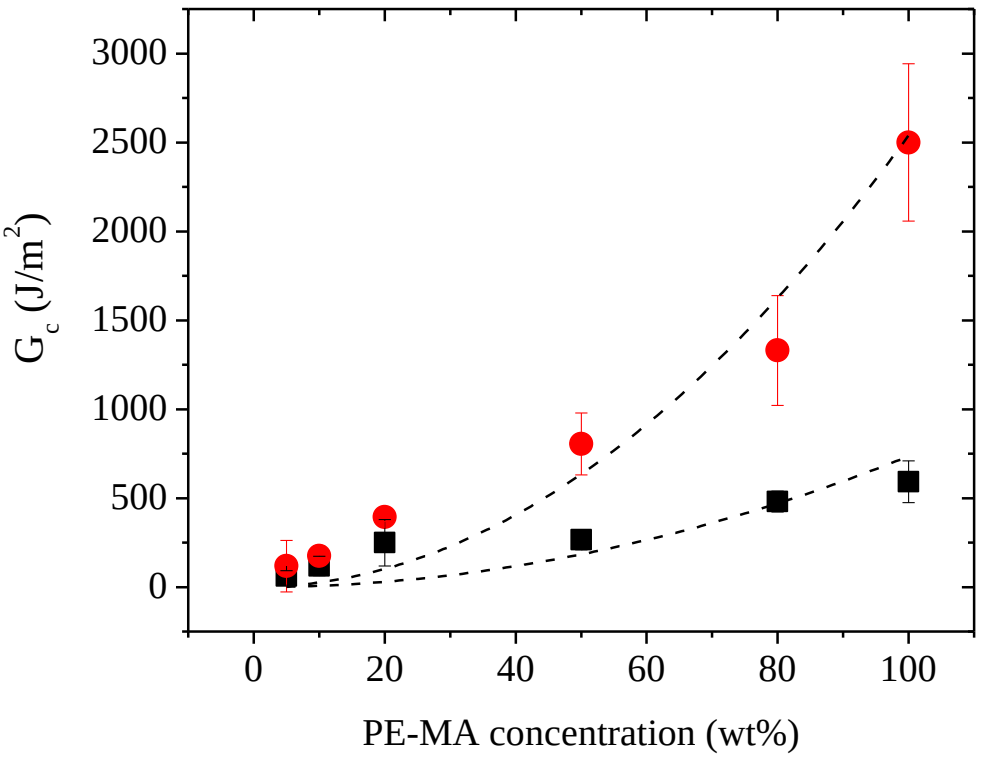

Figure 4.6 Critical energy release rate G_c development as a function of PE-MA concentration for lamination at 170 ℃ and 230 ℃ with reaction time 60 min. ■: 170 ℃, ●: 230 ℃. The broken lines are power law fitting of the data with an exponent of 2.

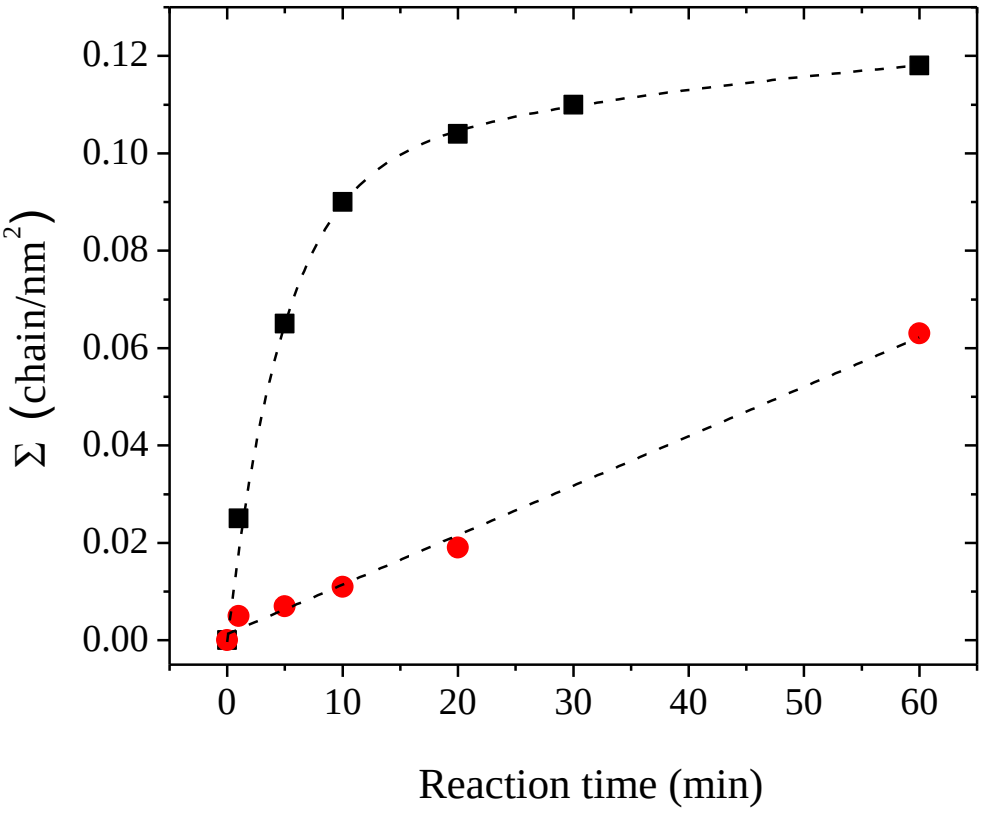

Figure 4.7 Interfacial copolymer density Σ vs. reaction time for lamination between nylon 6 and PE-MA. ■: 230 ℃; ●: 170 ℃.

We demonstrated that graft copolymer molecules were indeed formed at the interface, with an areal density Σ as verified by XPS. Table 4.2 summarizes the development of G_c and Σ as a function of process, temperature and reaction time. By plotting the data from Table 4.2, the resulting dependence of G_c as a function of Σ is shown in Figure 4.8. It is quite remarkable that all the data for samples made via different processes at different temperatures fall approximately on the same master curve. The measured critical energy release rate of the interface scaled as $G_c \propto \sum^2$ for high Σ coverage and it scaled as $G_c \propto \sum$ for relatively low coverage, regardless of the process,

reaction temperature and time. Combining the $G_c \propto C_0^2$ relationship in Figure 4.6, we have $\sum \propto C_0$, indicating the reaction rate is proportional to the concentration of reactive species at the initial stage of reaction.

G_c is the work required to produce a unit increase in crack area. It is a linear function of Σ if the interface failure occurs by simple chain scission or chain pull-out without any extensive plastic deformation, while it scales with Σ^2 if the applied interfacial stress is sufficient to activate plastic deformation of a small volume at the crack tip.[17,57] Those failure mechanisms apply to glassy polymers. However, semi-crystalline polymers are also of interest, and the question of whether the same models can be applied arises.

Brown derived an equation that describes the behavior of glassy and semicrystalline polymers when the main plastic deformation mechanism ahead of the crack tip is a craze and when failure of the craze occurs by chain scission in the fibrils. He showed that for adhesion between glassy polymers:[20]

$$G_c \approx (\sum^2 f_b^2 2\pi D / \sigma_d)(S_{22} / S_{12})^{1/2}(1 - 1/\lambda) \qquad \text{(Equation 4.3)}$$

where D is the craze fibril diameter, f_b is the force needed to break a covalent bond, σ_d is the crazing stress, λ is the fibril extension ratio S_{22} and S_{12} are the tensile and shear compliances of the crazed material, respectively. According to Equation 4.3, G_c scales as Σ^2 when all the other parameters are kept the same.

This model has been used to predict the adhesion development in glassy polymers with interfacial copolymers. For semicrystalline polymers, the large measured G_c values between nylon 6 and PE-MA are also due to the formation of a plastic zone ahead of the propagating crack tip as in glassy polymers. It has been shown that G_c is directly proportional to the maximum width that this plastic zone can achieve.[4] The maximum width of this plastic zone can be simply estimated by dividing G_c by the yield stress of the bulk polymer drawn into the plastic zone.[92,93] For tough interfaces, the resulting

maximum width is of several microns. This is much larger than the size of the connecting chains themselves (typically 50 nm).

Many testing arrangements, such as the DCB test by Creton et al.,[92,94] impose a plane strain condition. Plane strain can lead to cavitation, which is analogous to fibrillar shear at room temperature. The size of fibrils in semicrystalline polymers is on the order of microns, while it is typically about 10 nm for glassy polymers. This size difference may invalidate Brown's continuum model, and over-predict G_c relative to a discrete modeling of the fibrillar structure proposed by Sha et al.[95] for small energies of adhesion. However the two models are in good agreement for

$$\left(\frac{\sigma_y}{\Sigma f_b}\right)^2 < 1 \qquad \text{(Equation 4.4)}$$

Using the value for PE-MA (σ_y = 20 MPa and $f_b \approx 2 \times 10^{-9}$ N), Equation 4.4 predicts a lower limit of $\Sigma = 0.009$ nm^{-2}. Therefore, since majority of values of Σ in this study were greater than this limit, there is good agreement with the Brown model as shown in Figure 4.7. Thus, for both glassy and many semi-crystalline materials, the adhesion is expected to scale with the square of the areal density of copolymer. As a result, the measured critical energy release rate of the interface scaled as $G_c \propto \Sigma^2$ regardless of the process, reaction temperature and time.

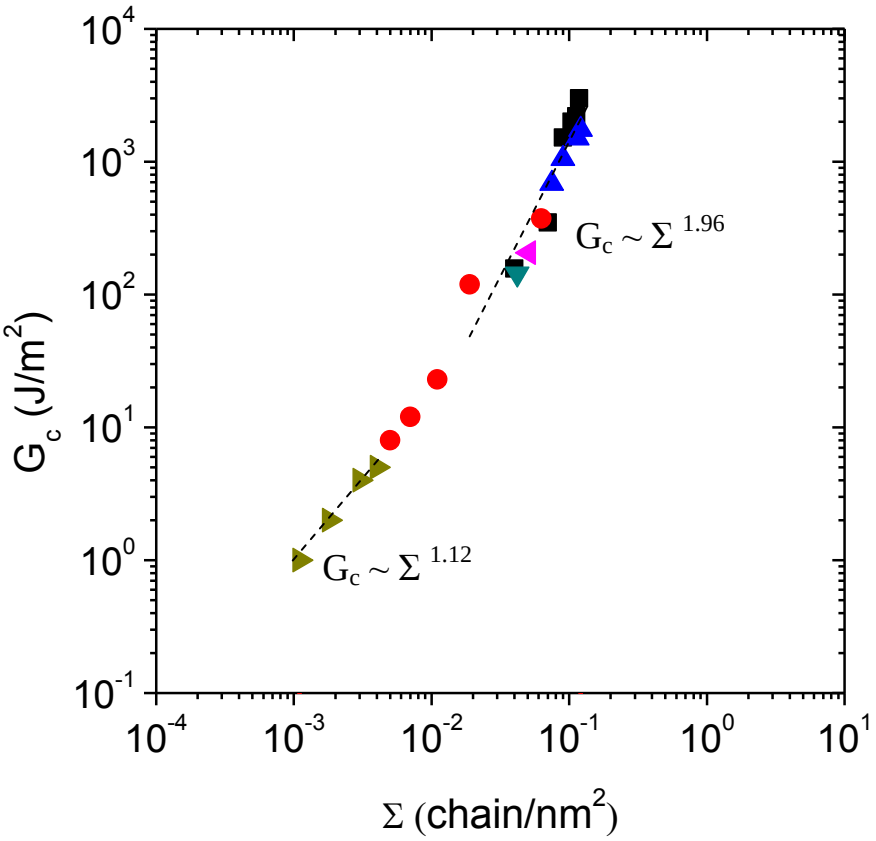

Figure 4.7 G_c vs. interfacial copolymer density Σ for coextruded and laminated nylon 6/ PE-MA bilayers. ■: Lamination at 230 ℃; ▲: Coextrusion at 230 ℃ with compressive/stretching die; ▼:Lamination at 230 ℃, PE-MA/ HDPE (5/95); ◀: Lamination at 230 ℃, PE-MA/ HDPE (10/90); ●: Lamination at 170 ℃; ▶: Coextrusion at 230 ℃ with stretching die. The broken lines represent power law fitting.

Table 4.2 G_c and Σ development as a function of process, temperature and reaction time for the coupling of PE-MA and nylon 6

Process	Temperature (℃)	Reaction time (min)	Σ (chain/nm^2)	G_c (J/m^2)
Lamination	230	1	0.025	157 ±20.5
Lamination	230	5	0.065	528 ±159
Lamination	230	10	0.09	1214 ±203
Lamination	230	20	0.104	1832 ±443
Lamination	230	30	0.113	2220 ±560
Lamination	230	60	0.118	2409 ±662
Lamination[a]	230	10	0.042	144 ±21
Lamination[b]	230	10	0.051	206 ±38
Lamination	170	1	0.005	8 ±1
Lamination	170	5	0.007	14 ±2
Lamination	170	10	0.011	23 ±4
Lamination	170	20	0.019	119 ±21
Lamination	170	60	0.063	372 ±48
Lamination[c]	230	0.17	-	120 ±20 (-11.9 s^{-1})
Lamination	230	0.17	-	210 ±42 (-13.9 s^{-1})
Lamination	230	0.17	-	453 ±69 (-15.7 s^{-1})
Lamination	230	0.17	-	955 ±109(-17.1s^{-1})
Lamination	230	0.17	-	1598 ±230(-21.9s^{-1})
Coextrusion (CS)[d]	230	0.09	0.076	585 ±143
Coextrusion (CS)	230	0.13	0.085	799 ±139
Coextrusion (CS)	230	0.15	0.09	1050 ±215
Coextrusion (CS)	230	0.17	0.115	1500 ±302
Coextrusion (CS)	230	0.2	0.121	2047 ±224
Coextrusion (CS)	230	0.23	0.124	2390 ±457

Coextrusion (S)[e]	230	0.17	0.0011	1 ± 0.9
Coextrusion (S)	230	0.2	0.0018	2 ± 1
Coextrusion (S)	230	0.23	0.003	4 ± 1
Coextrusion (S)	230	0.27	0.004	5 ± 1

[a] Lamination with PE-MA/ HDPE (5/95) blend; [b]Lamination with PE-MA/ HDPE (10/90) blend; [c] Lamination under different compression strain rates (The numbers in the bracket indicate strain rates); [d] Coextrusion with the compressive/stretching die; [e] Coextrusion with the stretching die.

4.4.2 Reaction acceleration through coextrusion with a compressive/stretching die

For coextrusion, we compared the reaction kinetics and adhesion development with different dies in Figure 4.8. It is striking that compressive/stretching die built up adhesion and generated interfacial copolymers almost 100 times faster than the stretching die, when all the other parameters were kept the same including type of material, flow rate, temperature and cooling conditions.

It should be noted that the reaction time used here is the summation of residence time in the die and also the dwelling time in the air gap. Since the melt temperature only decreased by ~ 4 ℃ from die exit to the nip point, a significant amount of reaction was expected to occur at the interface. Figure 4.8(a) shows that within only 15 seconds, the interfacial copolymer density of nylon 6 and PE-MA almost reached a plateau when a compressive/stretching die was used, while there was little amount of copolymers formed for a stretching die. Adhesion development in these two dies also showed similar trend. We plot the variation of Σ with time for coextrusion and lamination on the same figure as shown in Figure 4.9. Once again, compressive/stretching die showed remarkable reaction acceleration at the same temperature.

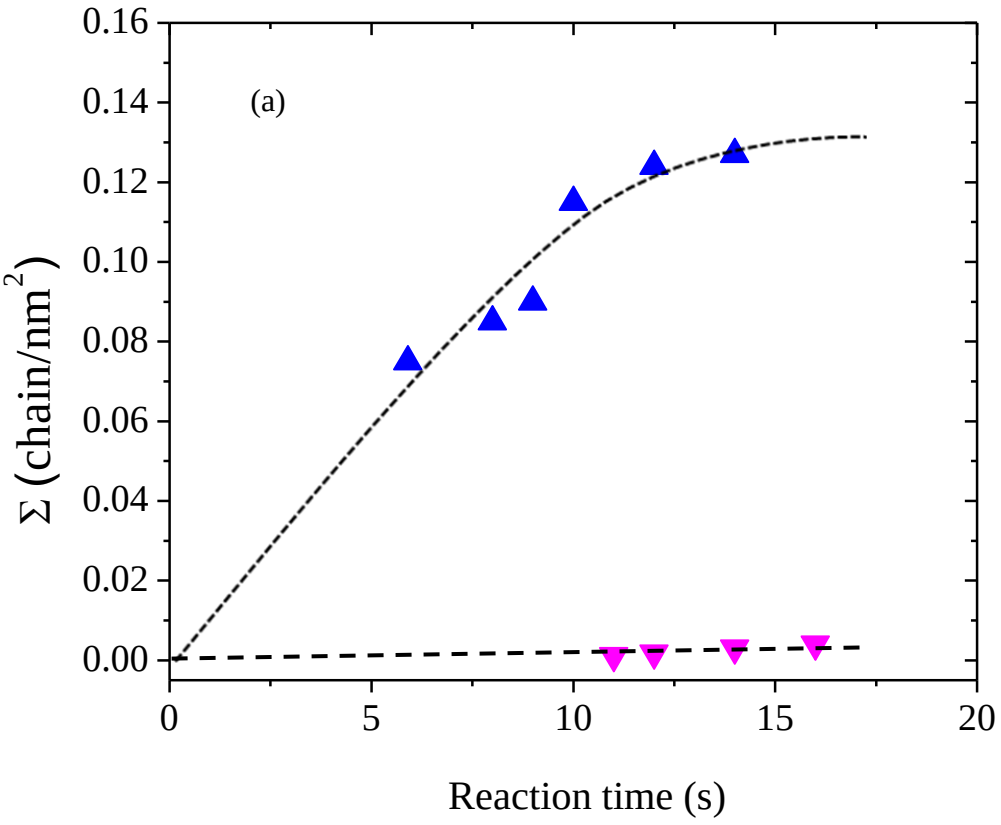
(a)
0.16
0.14
0.12
0.10
0.08
0.06
0.04
0.02
0.00
Σ (chain/nm^2)
0
5
10
15
20
Reaction time (s)

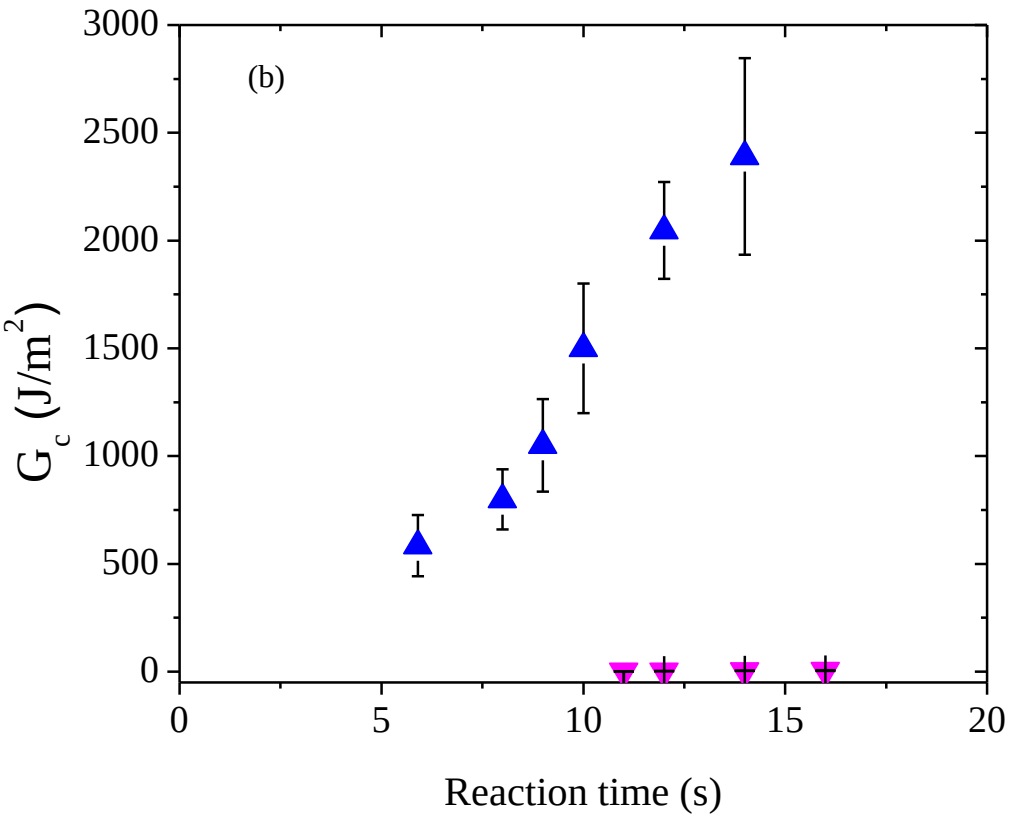

Figure 4.8 Comparison for coextrusion of nylon 6 and PE-MA via compressive/stretching die (▲) vs. stretching die (▼) at 230 ℃. (a) Σ vs. reaction time. (b) G_c vs. reaction time. The dashed lines are used to guide the eye.

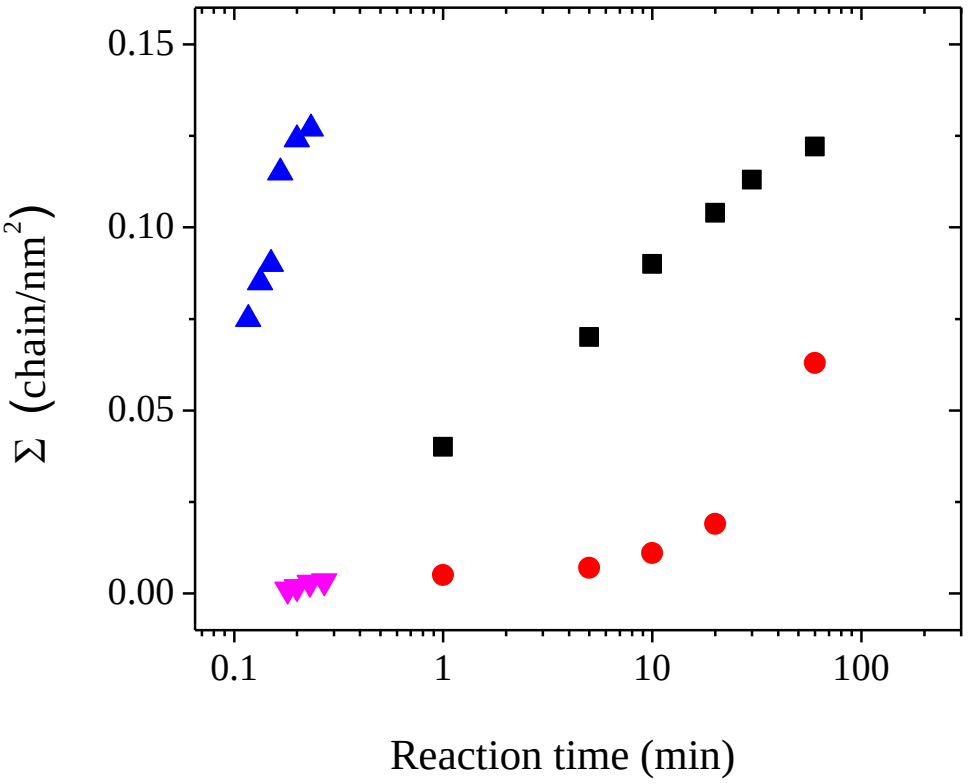

Figure 4.9 Interfacial copolymer density Σ vs. reaction time for coupling reaction between nylon 6 and PE-MA. ■: lamination at 230 ℃; ●: lamination at 170 ℃; ▲: coextrusion with compressive/stretching die at 230 ℃; ▼: coextrusion with stretching die at 230 ℃.

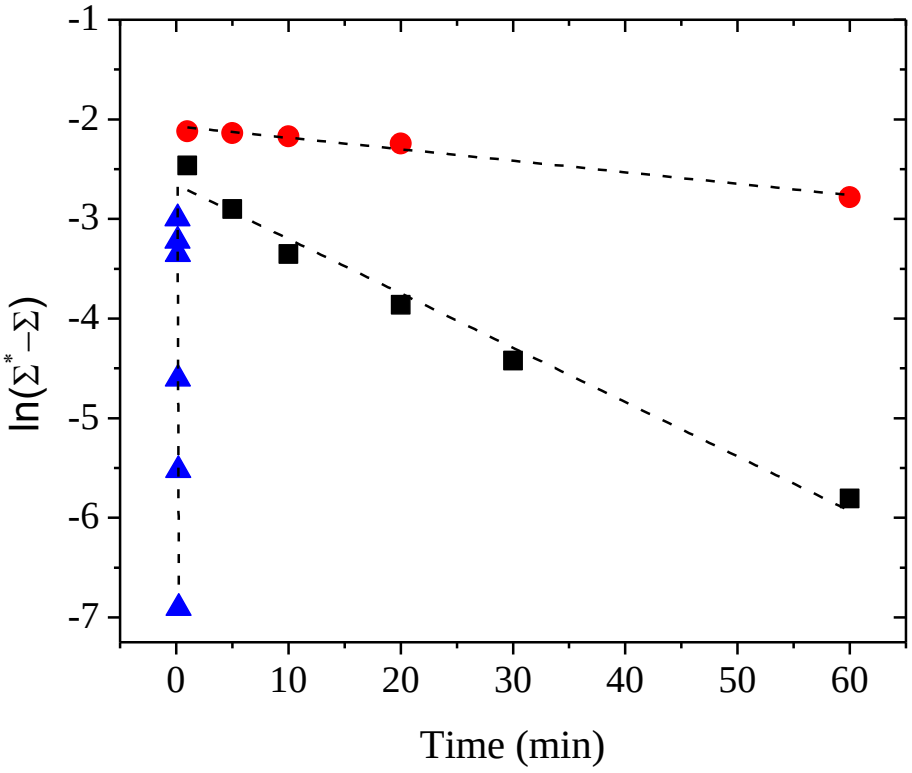

Figure 4.10 ln(Σ^* - Σ) vs. reaction time for coupling reaction between nylon 6 and PE-MA by fitting a pseudo-first-order reaction model. ●: lamination at 170 ℃; ■: lamination at 230 ℃; ▲: coextrusion with compressive/stretching die at 230 ℃.

We calculated the interfacial coupling reaction rates quantitatively in two ways. The first method was by simply assuming Σ increases linearly with time at the initial stage of reaction, as verified by data in Figure 4.7. By using equation $\sum = \nu t$, where ν is two-dimensional reaction rate and t is reaction time, we presented the results in Table 4.3. The reaction rate when using a compressive/stretching die is > 80 times than that of lamination, while coextrusion with a stretching die showed quite similar reaction rate with lamination at the same temperature.

The variation of Σ with time was also fitted with a pseudo-first-order kinetic model developed by Oyama et al.[29] The coupling reaction was assumed to proceed two-dimensionally on a flat interface and a monolayer-like copolymer formed by the reaction remained at the interface. In the end, the coupling reaction was terminated by interfacial saturation. The number of sites available for the reaction at the interface, $\Sigma^* - \Sigma$, determined the reaction rate. The reaction rate at the interface could be written as follows

$$r_{AB} = k_{AB}[A_{interface}][B_{interface}][\textit{vacant sites available for the reaction at the interface}]$$

(Equation 4.5)

Here k_{AB} was the rate constant, while $\left[A_{interface}\right]$ and $\left[B_{interface}\right]$ were the reactive group concentrations at the interface. For the initial stage of reaction, considered as the numbers of reactants per unit area located within the characteristic diffusion length are much larger than the concentration of formed copolymers, ln(Σ*-Σ) varies linearly with reaction time. This scheme is ideally suited to our system. As shown in Figure 10, Plotting the calculated ln(Σ^*- Σ) vs time showed a linear relationship. According to Oyama and Inoue's model, this implies that the overall coupling kinetics is reaction controlled.

Table 4.3 Reaction rates of interfacial coupling reaction between nylon 6 and PE-MA.

Processing Condition	Reaction rate (chain/(nm^2•min))	
	Pseudo-first-order model	Linear model[a]
Coextrusion (Compressive/Stretching Die, 230 ℃)	0.66	0.86
Coextrusion (Stretching Die, 230 ℃)	0.005	0.012
Lamination (230 ℃)	0.004	0.011
Lamination (170 ℃)	0.0007	0.001

[a]Linear model is based on the equation $\sum = \nu t$.

The fracture surfaces on each side of PE-MA/ nylon 6 adhesive interface were microscopically examined. Figure 4.11 shows the SEM images of the fracture surfaces of the samples with different processes and different adhesion strength. The distinct difference on the roughness and morphology of cleaved surfaces are shown between strong adhesion (G_c > 1500 J/m^2) in Figure 11(a) and very weak adhesion (G_c < 50 J/m^2) in Figure 11(b). The cleaved nylon surface via coextrusion at 230 ℃ using a compressive/stretching die with reaction time of only 12 seconds is analogous to the cleaved nylon surface via lamination at 230 ℃ for 30 minutes.

The morphologies in (a) and (c) also showed remarkable similarity. Some region on nylon 6 side is found to be covered with distorted fibrils-shaped domains. While strong adhesion gave roughened cleaved surfaces, Figure 11(b)(d)(f)(h) showed smooth surfaces correlated with weak adhesion. As much less copolymers were generated at the interface due to short reaction time, with Σ verified by XPS, the interfacial stress during fracture only generated very small amount of fibrils. Apparently compressive/stretching die generated exceptionally strong adhesion within short time compared with almost no adhesion for stretching die and slow adhesion development for lamination at the same temperature.

Thus, both the Σ quantification and adhesion measurement confirmed that the interfacial coupling reaction was greatly accelerated by coextrusion using compressive/stretching die in contrast with stretching die and lamination. Next, we will explore the mechanisms that generated this acceleration.

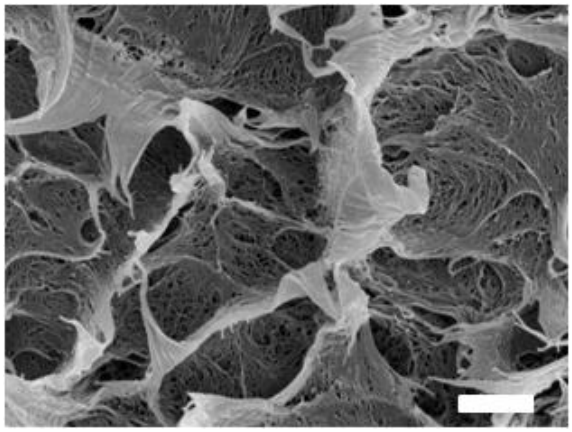

(a)

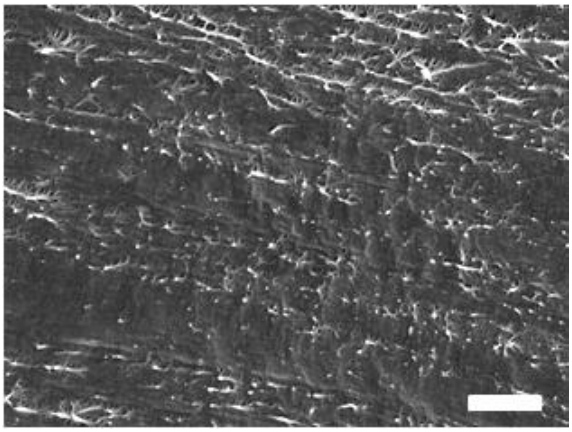

(b)

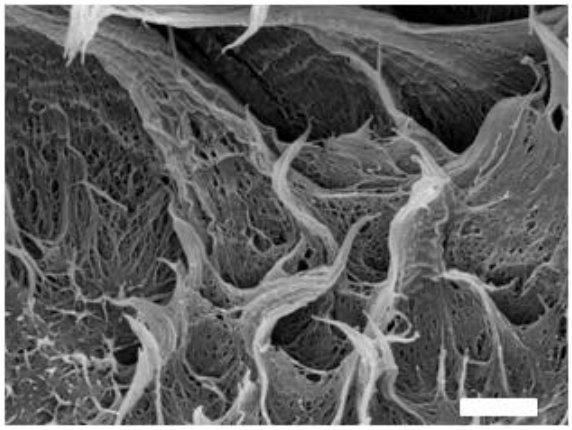

(c)

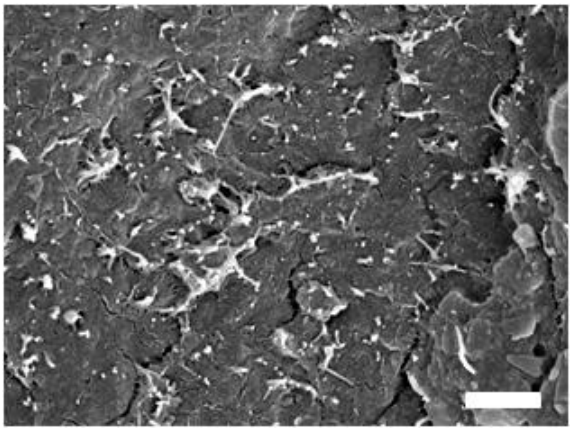

(d)

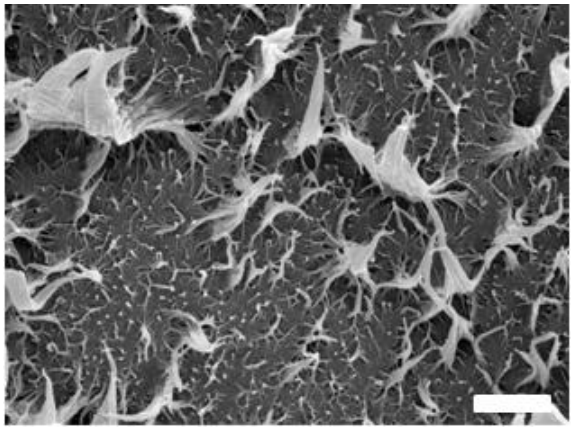

(e)

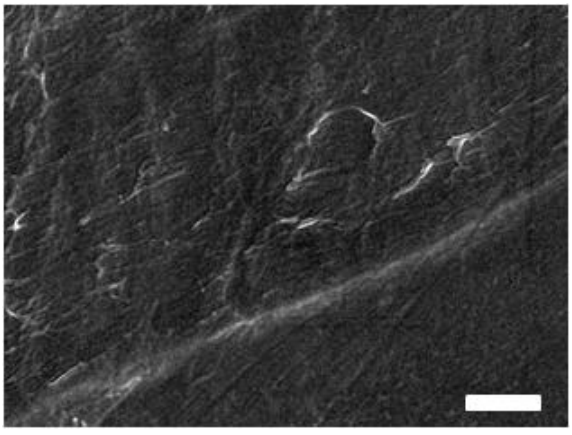

(f)

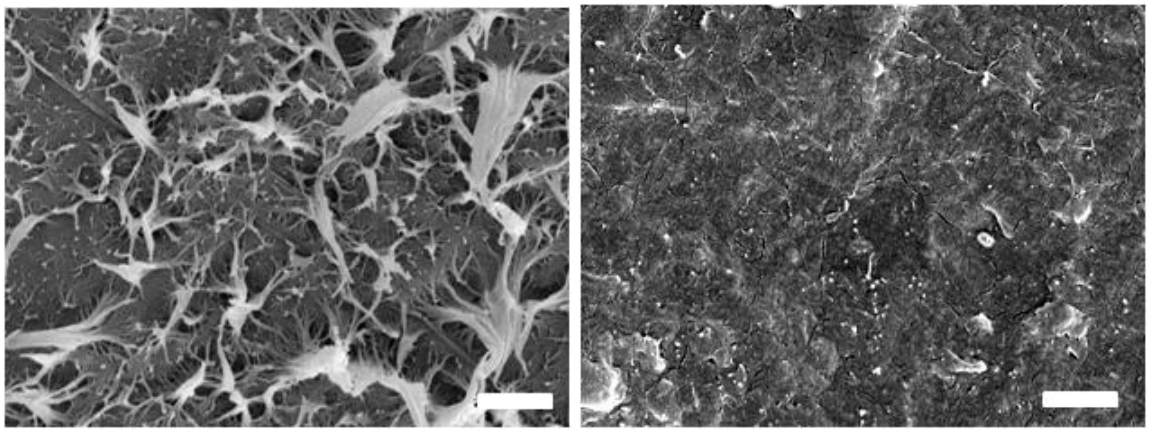

(g) (h)

Figure 4.11 SEM micrographs for cleaved surface after adhesion tests. All the samples before adhesion tests were prepared at 230 ℃. (a) nylon 6 (coextrusion using the compressive/stretching die with reaction time 12 s); (b) nylon 6 (coextrusion using the stretching die with reaction time of 12 s); (c) nylon 6 (lamination for 30 min); (d) nylon 6 (lamination for 1 min); (e) PE-MA (coextrusion using the compressive/stretching die with reaction time 12 s); (f) PE-MA (coextrusion using the stretching die with reaction time of 12 s); (g) PE-MA (lamination for 30 min); (h) PE-MA (lamination for 1 min). All the scale bars represent 1 μm.

4.4.3 Origin of reaction acceleration

For the coextrusion experiments reported here, the reaction acceleration occurs during laminar flow without mixing. Furthermore, the interface is located in the middle of the die, where shear stress approaches zero. However, the interfacial plane does experience compression and extension during coextrusion, as do the bulk phases above and below the interface.

Under compression/extension conditions, in the absence of shear or mixing, there are several possible causes of the increase of the interfacial reaction rate or the increase

of the measured adhesion strength. These include induced crystallinity, enhanced diffusive flux of functional groups via compression of diffusion boundary layers, and increased concentration of functional groups in the interfacial region due to extensional/ compressive flow in coextrusion. We will argue against crystallinity and show that enhanced diffusion alone cannot account for the dramatic increase in reaction rate. We therefore speculate that extensional and compressive flow in the coextrusion process contributes to the accelerated reaction rate during coextrusion.

Crystallinity is known to affect interfacial adhesion,[65,66] and this could increase the adhesive force even with constant copolymer reaction rate. We compared the crystallinity and crystal structures near the interface for coexrusion with different dies. We found that the crystallinity and crystal structures for the same polymer extruded though different dies are almost identical, as shown in the appendix Figure app.1 and app.2. The stress-strain curves were also the same for films produced by both lamination and coextrusion. Thus, crystallinity plays a negligible role in the observed increase in adhesion strength and we must consider possible mechanisms for increasing the copolymer reaction rate.

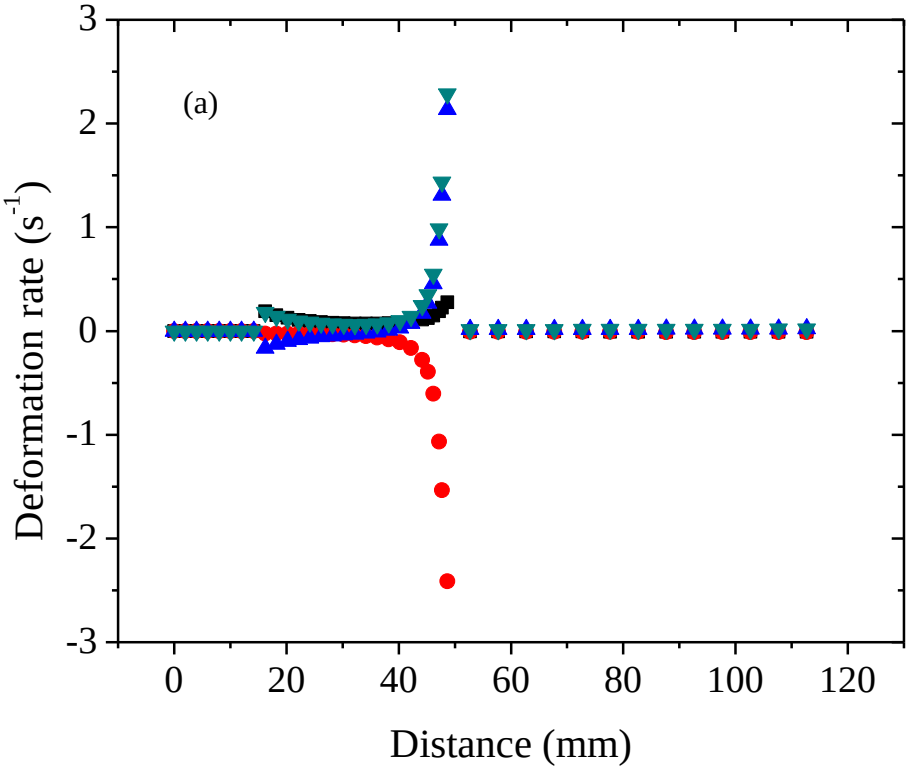
(a)
Deformation rate (s-1)
Distance (mm)
3
2
1
0
-1
-2
-3
0
20
40
60
80
100
120

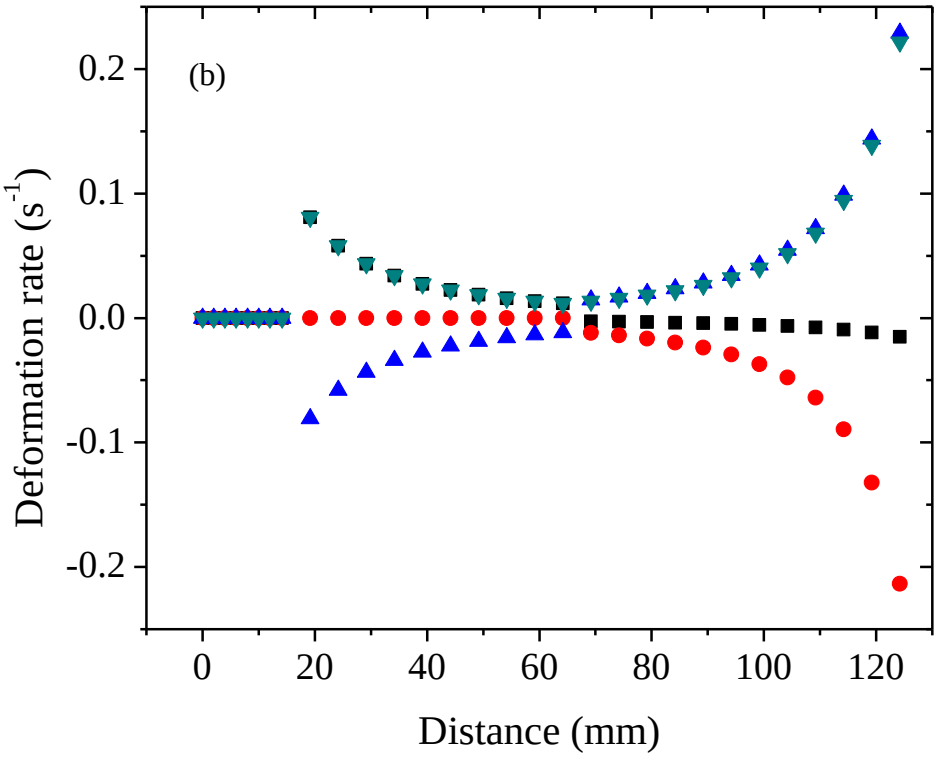

Figure 4.12 Deformation rate vs. distance for coextrusion at 230 ℃, starting from the initial contact of nylon 6 and PE-MA to the nip point of chill rollers. (a) compressive/stretching die; (b) stretching die. ●: $\dot{\varepsilon}_{zz}$ z-direction deformation rate; ■: $\dot{\varepsilon}_{yy}$ y-direction deformation rate; ▲: $\dot{\varepsilon}_{xx}$ x-direction deformation rate; ▼: $\dot{\gamma}$ Square root of the second invariant of deformation rate tensor. The dimensions of the polymer melt in the air gap: Figure (a), H_3 = 1.14 mm, W_3 = 47 mm, L_3 = 85 mm; Figure (b), $H_3^{'}$ = 1.5 mm, $W_3^{'}$ = 36.2 mm, $L_3^{'}$ = 85 mm.

We consider the general possibility of modifying diffusive flux or the local reaction process due to compressive flow normal to the interface. The absolute reaction rate is determined by the reaction-diffusion balance,

$$\nu = -D\frac{dC}{dz} \approx \frac{D(C_\infty - C_X)}{\delta} \qquad \text{(Equation 4.6)}$$

where ν is the two-dimensional coupling reaction rate in the interface, D is the diffusivity of the functional PE, C_∞ the volumetric density of grafted functional groups in the bulk, C_X is the volumetric density of grafted functional groups at the interface, and δ is the diffusion lengthscale. We compared reaction rate to transport rate by calculating Damkohler number (shown in the appendix) and found that although decreasing the diffusion length scale δ due to external mass transfer will increase the reaction rate, such increase of diffusive flux would be negligible for the reaction-limited process studied here.

We are therefore left to conclude that reaction acceleration was mainly caused by an increase in the local reaction process, and suggest that extensional and compressive flow in the coextrusion process gave rise to the reaction acceleration.

The degree of polymer orientation/extension depends on external deformation. In general, the onset of polymer deformation under flow occurs when hydrodynamic friction force across the chain exceeds the entropic elasticity of the coiled chain. The onset of polymer stretching occurs[96] at a critical strain rate of $\dot{\varepsilon}_c$ of $\dot{\varepsilon}_c \approx 0.5/\tau_1$, where τ_1 is the longest relaxation time of the polymer. When $\dot{\varepsilon} < \dot{\varepsilon}_c$, polymer chains are in the "coiled" state. When $\dot{\varepsilon}$ increased to be above $\dot{\varepsilon}_c$, the external stress field just exceeds the linear portion of the polymer's entropic elasticity. Thus, the polymer will stretch until its nonlinear elasticity limits the further extension of the "stretched" state.

Chu et al. reported[97-99] elegant studies of the conformational dynamics of individual, flexible polymers (fluorescence labeled DNA molecules) under flow. Under elongational flow, the extension rises dramatically to a value close to the full contour

length of the chain at quite low W_i values.[97-99] The shear and elongational process can be characterized by the Weissenberg number, Wi, which is the ratio between the flow time scale (reciprocal shear rate) and the diffusion time scale (the longest relaxation time), accounting for Brownian motion induced configuration changes.

It should be noted that the above discussion is for polymers in dilute solution. The corresponding situation in an entangled melt is more complicated due to inter- and intra-molecular interactions. Yet polymer chain dynamics is expected to be affected by the characteristics of the surrounding matrix. We expect that the behavior of the mean fractional extension versus *Wi* should qualitatively similar to that in dilute solution.

For the coextrusion process in our study, we first calculated the rate of deformation in all the coordinate directions for both the compressive/stretching die and the stretching die. The same assumptions are applied as in the previous chapter,[83] i.e. perfectly slipping boundary conditions and plug flow. The results are plotted in Figure 4.12. While for stretching die the maximum deformation rate along the entire process was below 0.25 s^{-1}, $\dot{\varepsilon}_{zz}$, $\dot{\varepsilon}_{xx}$ and $\dot{\gamma}$ increased to around 2.5 s^{-1} dramatically when the bilayer hot melt approached the exit of compressive/stretching die. From the steady shear test, we obtained ~0.37 s as the longest relaxation time for PE-MA. Then we determined that the maximum Wi for compressive/stretching die is ~ 1 while for stretching die, the maximum Wi is only 0.09. Apparently there was chain stretching in the compressive/stretching die during melt processing. For the stretching die, polymer chains stayed in "coiled" state along the entire process.

As discussed above, there was significant stretching of polymer chains when the reactive bilayers were extruded through the compressive/stretching die. It has been proven that stretching a polymer can accelerate chemical reactions of its building blocks by many orders of magnitude.[100,101] Although it is miscellaneous how stretching polymer chains could influence reaction rate, we speculate that functional polymers that are "slammed" into interface and stretched by flow increase the collision possibility of functional groups.

The interface between two immiscible polymers plays the role of an obstacle (or diffusion barrier) that hinders the diffusion of both reactive polymer chains to the interface for chemical reactions. Rafailovich[67] *et al*. found that the diffusion rate is one order of magnitude slower near an interface compared with in the bulk. We speculate that under coextrusion condition flow helps forcing reactive species to penetrate into interface and increases the concentration of reactive species in the interface. In addition, the interaction between MA groups with nylon backbones or between NH_2 with PE-MA backbones is repulsive. Flow helps overcome this repulsive force and facilitates reactions.

In addition, flexible macromolecules that contain functional groups distributed along the chain that favors aggregation.[102-104] These groups interact via short-range forces. The functional groups could be ionic, so that the nature of the interactions is electrostatic. We speculate that the polar functional groups attached to the non-polar hydrocarbon backbones have the tendency of aggregation. Flow facilitates to release the functional groups from aggregated cage and expose them to interfacial reaction.

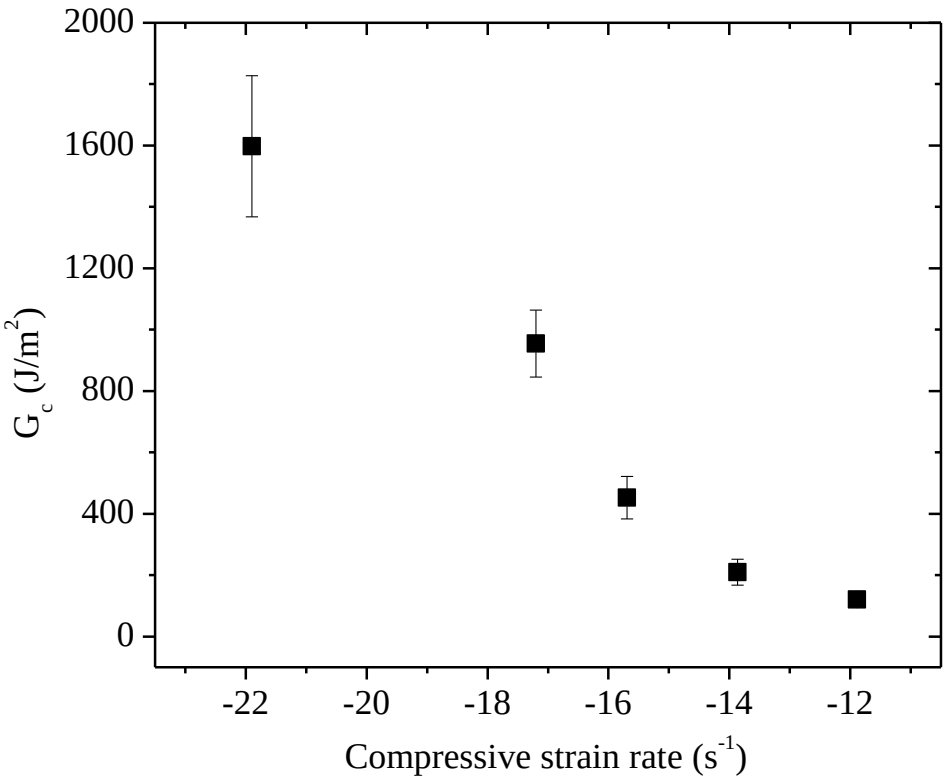

Figure 4.13 G_c vs. compressive strain rate for lamination between PE-MA and nylon 6 annealed for 10 seconds at 230 ℃.

To test the hypothesis that compressive deformation normal to the interface accelerates interfacial reaction, we repeated some lamination tests with more compressive flow as shown in Figure 4.13. As the magnitude of Hencky strain rate increased, the adhesion strength increased dramatically within only 10 seconds annealing time. Thus, when a larger compressive strain rate was applied normal to the interface, more copolymers were generated at the interface.

4.5 CONCLUSION

Coupling reaction occurred during the coextrusion and lamination of a nylon 6 /PE-MA bialyer. Aspects contributing to adhesion between nylon 6 and PE-MA were systematically studied including reaction temperature, annealing time, concentration of incorporated functional PEs, crystallinity and processing methods. Direct measurements of interfacial adhesion by ADCB test and interfacial copolymer density by XPS allowed us to compare the reaction rates under different conditions.

It is striking that with all the other parameters being the same, the reaction rate of coextrusion through a fish tail die was almost two orders of magnitude larger than that through a stretching die. The reaction rate through a stretching die was found close to that of lamination.

For the coextrusion experiments reported here, the interface was under compression/extension conditions and in the absence of shear or mixing. We compared the deformation rates on all the coordinates along coextrusion process with different dies. While the maximum deformation rate along the entire process for stretching die was below 0.4 s^{-1}, $\dot{\varepsilon}_{zz}$, $\dot{\varepsilon}_{xx}$ and $\dot{\gamma}$ increased to around 20 s^{-1} dramatically when the bilayer hot melt approached the exit of compressive/stretching die. A direct result of large deformation rate was that polymer chains were stretched significantly in the compressive/stretching die and they stayed in the "coiled" status when stretching die was used. We speculate that flow accelerates interfacial coupling reaction due to the synergistic effects of following mechanisms: (1) Functional polymers that are "slammed" into interface and stretched by flow increase the collision possibility of functional groups; (2) Flow overcomes the repulsive force between polar functional group from one polymer and non-polar backbones of the other polymer and facilitates reactions; (3) Flow facilitates to release the functional groups from aggregated cage and expose them to interfacial reaction.

Beyond its scientific significance, this work illustrates why coextusion is so successful for producing multilayer products within a very short residence time.

Enhancing the compressive/ extensional flow can build up interfacial adhesion much faster even with all the other parameters being the same. Taking advantage of flow conditions during polymer processing may create revolutionary opportunities for designing new reactions, products and materials.

CHAPTER 5

Polyethylene/ Polyurethane Blends for Improved Paint Adhesion

5.1 OVERVIEW

Polyolefins have low free surface energy that prevents good wettability of adhesives or paint emulsions to their surface. This work shows that adhesion of olefin block copolymers (OBC) to a polyurethane-based paint can be significantly improved by blending thermoplastic polyurethane (TPU) into OBC. Furthermore, blend morphologies near the paint/polymer interface, and surface compositions of injection molded plaques, were characterized by scanning electron microscopy (SEM), atomic force microscopy (AFM), x-ray photoelectron spectroscopy (XPS) and Fourier-transform infrared spectroscopy with attenuated total reflectance (FTIR-ATR) in order to explore the underlying mechanism of paint adhesion to TPU/OBC blends. It was found that for 35 wt% and 25 wt% TPU loading, the top paint layer is well-attached at the interface, whereas for 15 wt% loading, there was incomplete wetting of the paint, and a gap between the polymer substrate and paint was apparent. XPS and SEM gave consistent results demonstrating that outermost surface composition of TPU in these blends is slightly higher than in the bulk. It is speculated here that, during painting and the subsequent drying step, polyurethane chains from the paint diffuse into the blend substrate and entangle with TPU in the blend. The entanglement between paint and substrate generates a physical link that provides adhesion.

5.2 INTRODUCTION

Polyolefins (PO) are the largest family of commercial polymers. The main commercial drivers for this success are their excellent cost position, mechanical properties, environmental and energy footprint, recyclability, and chemical resistance [105,106]. Some of the applications where PO are used demand that the part is painted. These include automotive and consumer goods. However, the intrinsic non-polar surfaces of polyolefins inevitably lead to poor paint adhesion.

To achieve the adhesion between a polyolefin substrate and a paint, various surface modification technologies have been developed, such as flame or plasma treatment [107], or application of chlorinated and non-chlorinated adhesion promoters [108]. Although these surface treatments can lead to enhanced paint adhesion, there are shortcomings associated with each of them. Chlorinated and non-chlorinated chemicals and organic solvents are not desirable from an environmental point of view, and flame or plasma treatment require extra investment in infrastructure and manufacturing time.

Over the past decades, blends of PO with polar polymers have received attention as an easy route to enhance the adhesion of polyolefins [109]. It has been shown that near-surface morphology of the unpainted and painted injection molded polyolefin plaques is of primary importance in controlling the paint adhesion to the polyolefins [110]. Characterization techniques, such as X-ray microfocus fluoroscopy [111], visible-light differential interference microscopy [112,113], and photo-acoustic Fourier transform infrared spectroscopy [114], have been used to determine the polyolefin surface morphology. These are indirect observational techniques and the practical spatial resolution limits of all of these techniques are on the order of several micrometers. Direct observational techniques and better resolutions are needed.

In this study, in order to enhance the adhesion between a polyurethane paint and an olefin block copolymer (OBC), thermoplastic polyurethane (TPU) was blended into OBC. This study is aimed at determining the mechanism of paint adhesion associated with these blends, specifically the blend morphology near the paint polymer interface and the TPU composition on the surface.

5.3 EXPERIMENTAL

5.3.1 Materials

OBC and TPU were provided by The Dow Chemical Company. INFUSE™ 9500 is a polyolefin elastomer (POE) with blocks of hard (highly rigid) and soft (highly elastomeric) segments. This polymer has a density of 0.877 g/cm^3, melt index of 5.0 g/10 min (190 ^{o}C/ 2.16 kg) and zero shear viscosity of 1.4×10^3 Pa s at 200 ^{o}C.

The TPU we used is a polytetramethylene glycol ether-based polyurethane elastomer with 25 wt% hard segment composed of 4,4'-methylene diphenyl diisocyanate (MDI) and 1,4-butanediol. The zero shear viscosity of this TPU is 1.2×10^3 Pa s at 200 ^{o}C. The paint used is a 1K polyester diol-based polyurethane paint (Marbo, Italy) with ethyl acetate and butyl acetate as the major solvents.

5.3.2 Blend preparation

Three compositions were prepared: 15, 25 and 35 wt% of TPU. These samples were prepared either by compounding with a Twin Screw Extruder (TSE) or by dry blending. The former are denoted here C_1, C_2 and C_3, and the latter P_1, P_2 and P_3.

C_1, C_2 and C_3 were prepared on a Werner and Pfleiderer ZSK-25 compounding extruder. The TPU and OBC pellets were fed through separate weight loss feeders that were controlled to feed in the ratio of the desired composition. Between 2-5 wt% of maleated polyethylene based elastomer was used to aid dispersion of the TPU in the OBC. This elastomer was dry blended with the polyolefin component and fed together with the polyolefin. A temperature profile of 140 °C in zone 1 and 170 °C in zone 2 through zone 8 was used. The extruded strand was pelletized and dried overnight in a conventional static oven at approximately 80 ℃ to remove residual moisture.

The dry blends, P_1, P_2 and P_3 were dry blended from pellets and fed directly into the injection molder. The same formulation ingredients described above were used in this dry blending study.

5.3.3 Injection-molded plaques

Injection molding was carried out on an Arburg 370C, 80 ton injection molder using a plaque mold with dimensions 10.2 cm × 15.2 cm × 0.32 cm. No mold release was applied. The nozzle temperature was set at 200 ℃. Mold temperature was 18 ℃. The injection molded plaques were held at 600 bar for 30 seconds.

5.3.4 Paint adhesion test

Figure 5.1 shows the procedure used to evaluate paint adhesion based on ASTM D3359 method B and DIN Standard 53151. Samples are cleaned once with a wipe (Kimberly-Clark KIMTECH Science) soaked with toluene and allowed to fully evaporate afterwards. Painting is applied with wire rods that lay down a dry thickness of 15-20 μm. Plaques are dried at room temperature for four days. The surface of each painted plaque is scratched with a tool holding 11 cutting blades, separated from each other at 2 mm distance, both vertically and horizontally, thus creating 100 small squares of 4 mm^2. A strip of adhesive tape (TESA™ Tesafix 04970-00154-00) is applied with constant pressure which is released after 1 min. The tape then is pulled at 90° to the plaque surface. The experiment is repeated a second time with a new piece of tape. The percentage of squares where the paint is still intact is reported.

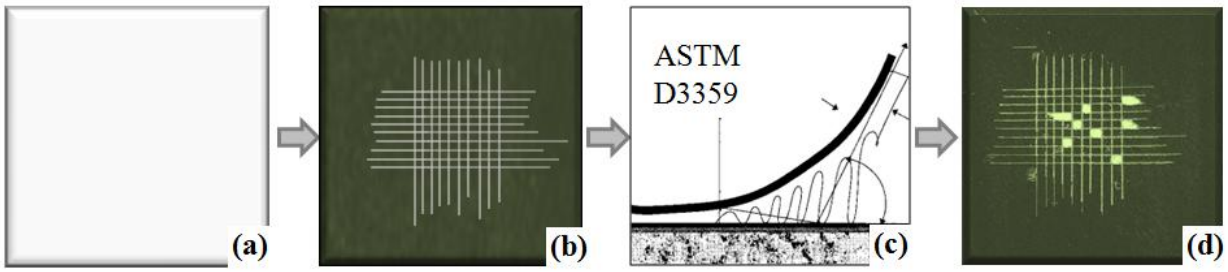

Figure 5.1 Procedures for testing paint adhesion based on ASTM D3359 method B and DIN Standard 53151. (a) Prepare plaques via injection molding; (b) Spread PU paint with wire rods. Cut the paint layer into 100 small squares after paint is fully dried; (c) Apply adhesive tape and peel; (d) Report the percentage of squares with intact paint.

5.3.5 Characterization techniques and sample preparation

X-ray photoelectron spectroscopy (XPS)

XPS measurements were performed on a Surface Science SSX-100 spectrometer using a focused monochromatic Al Ka anode (hv = 1486.6 eV) and a spot size of 800 μm. Electrostatic charging was neutralized by mounting a nickel grid about 2 mm above the sample surfaces. Accelerating voltage of 10 kV was used for data acquisition. After reflections corresponding to binding energies of C_{1s}, O_{1s} and N_{1s} were identified, higher resolution spectra were recorded for elemental quantification. The recorded spectra were adjusted to the C_{1s} peak of the saturated hydrocarbon bonds at a binding energy 284.6 eV. Samples were cut near the center of injection molded plaques and cleaned once with a wipe soaked with toluene. Then the toluene was allowed to fully evaporate. The elemental compositions were quantified from the peak areas using Wagner's sensitivity factors [91] and the spectrometer transmission function was taken into account. The parameters used for fitting were the peak area, the peak full width at half maximum, the position of the peak maximum, and the Gaussian–Lorentzian ratio.

Scanning electron microscopy (SEM)

SEM images were taken with a JEOL 6500 scanning electron microscope with a field-emission gun. Samples were cut from near the center of the painted injection molded plaques and then cryo-microtomed in the direction parallel to the interface. All SEM samples were stained in RuO_4 vapor for twenty minutes. Cracks were generated at the interface to observe the microstructure during delamination. Electron beam current and potential were varied for optimal imaging. Small working distance of ~4 mm was used to observe surface detail. Thresholding image analysis was applied for surface composition calculation.

Fourier-transform Infrared Spectroscopy with Attenuated Total Reflectance (FTIR-ATR)

A Fourier-transform infrared spectroscopy (FTIR) (Nicolet Series II Magna-750, Thermo Fisher Scientific Inc., Waltham, MA) equipped with a single bounce attenuated total reflectance (ATR) attachment (Profilir TM, SpectraTech, Oak Ridge, TN) and a mercury-cadmium-telluride detector was used to collect spectra. Samples were cut using a razor blade from the center of unpainted injection molded plaques and a total of three samples were tested for each plaque. The sample was pressed against the ATR crystal to ensure complete contact. A total of 512 scans were taken on each sample over the wavelength range of 4000 to 400 cm^{-1} at a resolution of 4 cm^{-1}.

Atomic force microscopy (AFM)

The free surfaces and cryo-microtomed cross-section of injection molded plaques were examined using AFM with a Nanoscope III Multimode system (Digital Instruments) in tapping mode within the repulsive regime. All the data were acquired in height and phase mode with scan rate of 1 Hz. The root mean square (RMS) roughness was evaluated by analyzing the 2-dimensional (2D) height image with the Nanoscope software.

5.4 RESULTS AND DISCUSSION

5.4.1 Blend morphology near polymer-paint interface

Table 5.1 shows the paint adhesion results on the neat OBC and TPU, as well as blends made either via twin-screw extrusion (C_1, C_2, C_3) or "at press" injection molding (P_1, P_2, P_3). OBC showed 0% adhesion strength due to its intrinsic non-polarity; TPU showed 100% adhesion strength as expected. It would appear from Table 5.1 that the blend preparation did not have an effect on paint adhesion strength for blends with the same concentration of TPU.

Table 5.1 Compositions of OBC/ TPU blends and paint adhesion based on ASTM D3359.

Sample	Concentration of TPU (wt %)	Paint adhesion (%)
TPU	100	100
OBC	0	0
C_1	15	0
C_2	25	95
C_3	35	100
P_1	15	0
P_2	25	95
P_3	35	100

Figure 5.2 displays SEM microphotographs of the cross-sections of painted TPU/OBC blends. The top continuous phase is the coated paint layer, while the bottom dispersed morphology corresponds to TPU/OBC blends. For the bottom layer, the bright region represents TPU and the dark region is OBC. TPU domain size is around 100 nm for the C series due to the good mixing achieved with twin screw extruder and the presence of the compatibilizer. For the P series, some larger TPU domains can be seen, because of poorer mixing.

TPU domains from the substrate are attached to the top painting layers across the interface in Figure 5.2 (b) and 5.2 (c). However, for 15 wt % TPU loading in Figure 5.2 (a), a gap is visible between the paint and the substrate indicating poor attachment. Figure 5.2 (d) demonstrates the development of fibrils during paint layer delamination, indicating the formation of continuous PU domains at the interface due to PU inter-diffusion. The AFM images, Figure 5.3 (a), also show that there are gaps between paint

and substrate of P_1. Some areas of the substrate were covered by OBC, giving rise to incomplete wetting due to the low surface energy of OBC. Figure 5.3 (b) shows that there is some inter-connection between the paint layer and TPU from the polymer substrate.

Several mechanisms have been proposed to explain paint adhesion, such as formation of functional groups at the surface to allow covalent bonding or other interactions [115,116], increased surface roughness to allow mechanical interlocking [117], and inter-diffusion of polymer chains to form interphases [118]. Since the paint used in this study also has polyurethane (PU) as the major component, we believe that the entanglement of TPU from the substrate and paint via solvent, i.e., polymer chain inter-diffusion at the interface is the mechanism of paint adhesion for TPU/OBC blends. We support our hypothesis further with measurement of the concentration of surface TPUs.

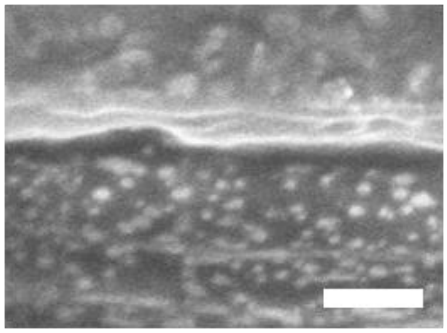

(a) Blend P_1 (15 wt% TPU)

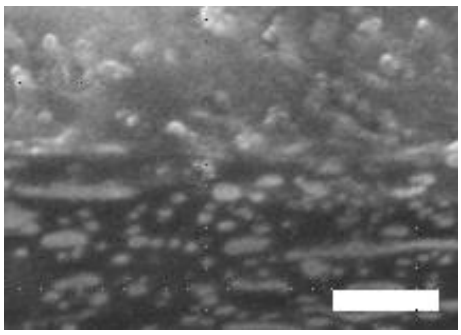

(b) Blend P_2 (25 wt% TPU)

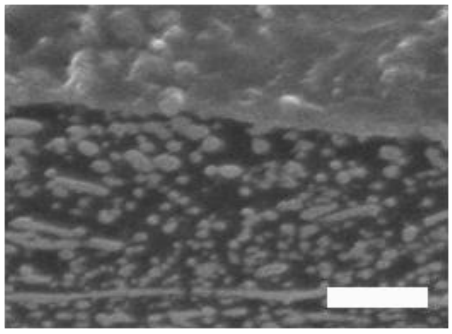

(c) Blend P_3 (35 wt% TPU)

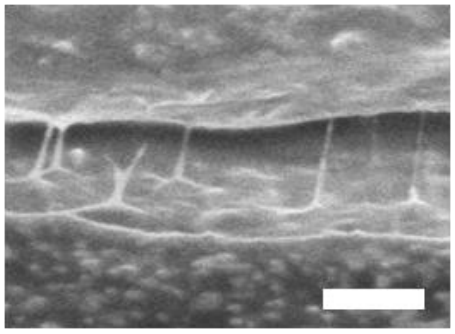

(d) Blend P_2 (25 wt% TPU)

Figure 5.2 SEM micro-photographs of cross-sections of painted TPU/OBC blends. For each image, the top layer is paint and the bottom layer is TPU/OBC blend. PU fibrils attached to the top paint layer during delamination in Figure (d). All the scale bars represent 500 nm.

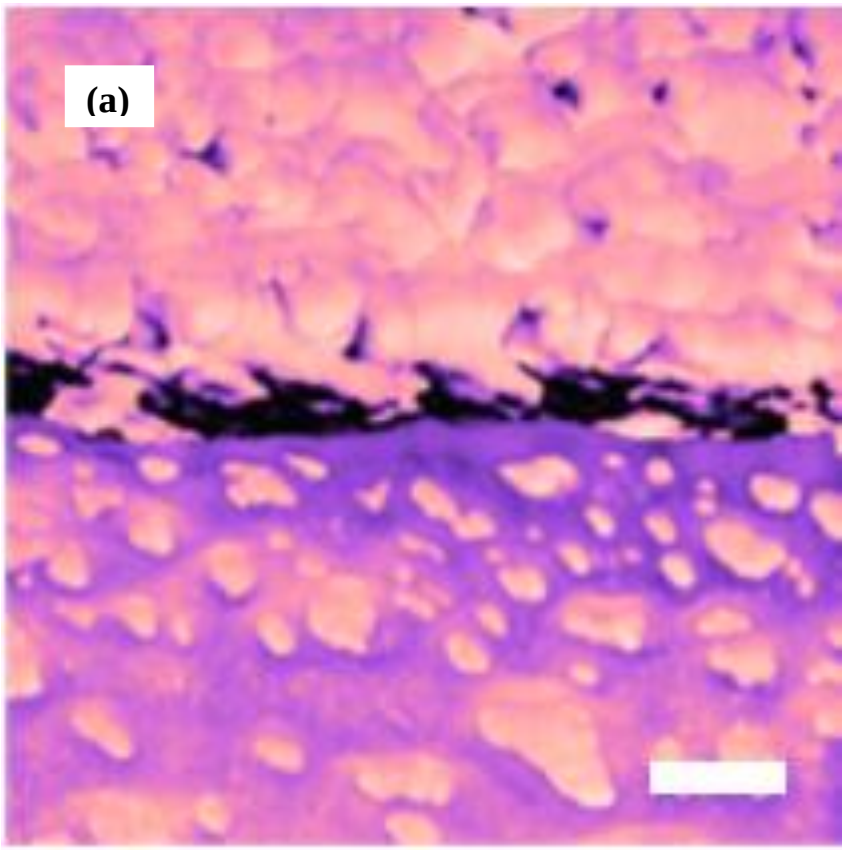
(a)

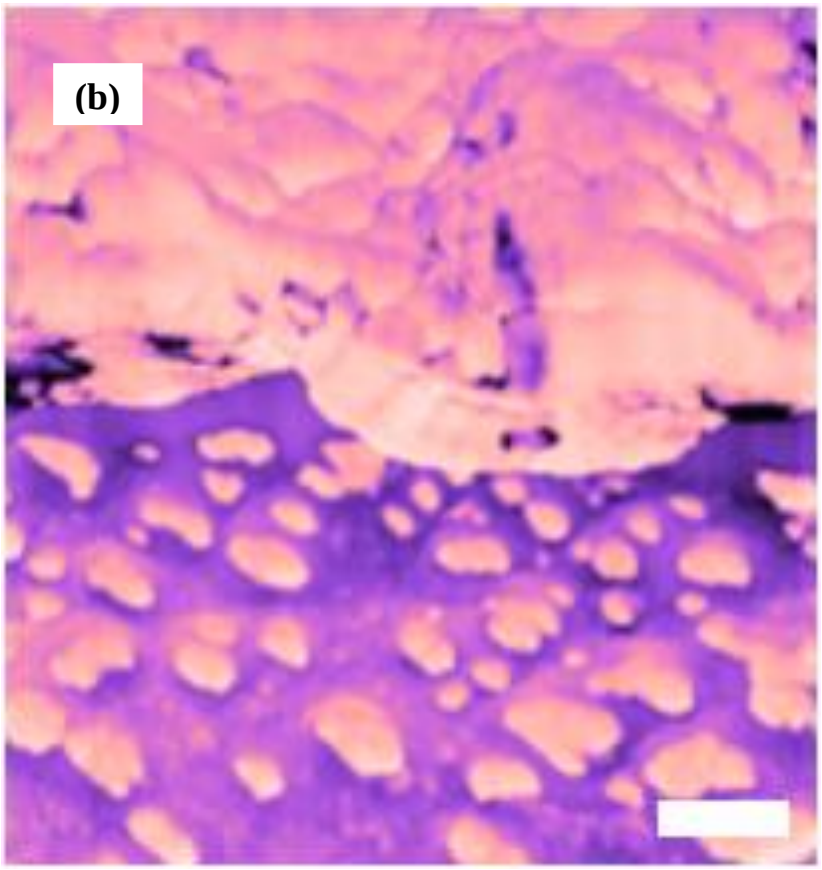

Figure 5.3 AFM phase contrast images of cross-sections of painted TPU/OBC blend P_1. The two images represent different locations of the same sample. For each image, the top layer is paint and the bottom one is TPU/OBC blend. The scale bar represents 250 nm.

5.4.2 Surface composition of TPU/OBC substrates

The surface compositions of injection molded plaques were quantitatively measured by XPS. Figure 5.4 (a) shows the XPS spectra of the surfaces of TPU and OBC. No detectable oxygen was found for the surface of OBC. For TPU, there is around 20 % oxygen on the surface, slightly higher than the calculated value 18.9 %, presumably due to a higher concentration of soft domain on the surface [119-122]. An asymmetric C_{1s} peak centered at 284.6 eV in TPU has a shoulder toward higher binding energy, indicating

presence of C-O and C=O bonding on surface. Table 5.2 lists the surface oxygen concentration based on high resolution scanning of C_{1s} and O_{1s} peaks as shown in Figure 5.4 (b). The measured oxygen concentration values are greater than calculated ones, i.e., based on bulk concentration, indicating surface enrichment of TPU.

Scanning electron imaging enables observation of topography on surface. During staining, RuO_4 vapor can react with carbon-carbon double bonds in the TPU regions [123], which enables the enrichment of ruthenium in TPU region; no covalent bonding is expected between ruthenium and polyolefin. Therefore, TPU-rich regions appear brighter in secondary electron imaging, giving rise to the contrast between TPU and OBC. The root mean square roughness for the surfaces of all the injection molded plaques were determined to vary between 10 and 30 nm by AFM, such that surface topography will not influence the compositional analysis. Thresholding image analysis was used to quantify the surface concentration of TPU. For example, in Figure 5.5, the scanning electron micrograph on the left was converted to the one on the right, where white region represents TPU and black one OBC. Quantitative results are shown in Table 5.3. The surface concentration of TPU determined from both SEM and XPS typically agreed to within 15%. The images show that TPU is stretched out into fiber-like domains in the flow direction.

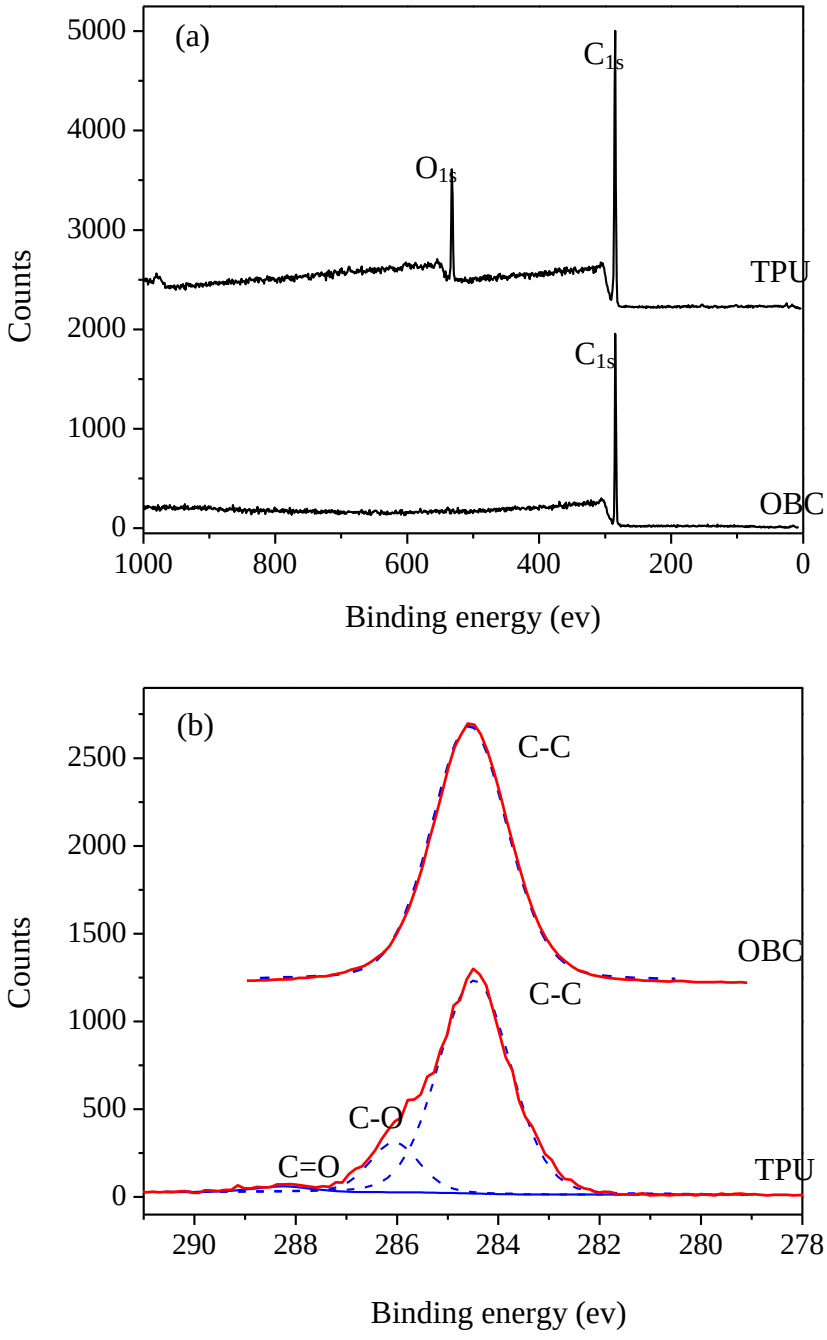

Figure 5.4 XPS spectra of TPU and OBC surfaces (a) Full survey XPS spectra of TPU and OBC free surfaces (b) High resolution XPS spectra of TPU and OBC free surfaces (Solid curves are original data; Dashed curves represent deconvolution of the spectrum after curve fitting).

Table 5.2 Surface oxygen concentration of the injection molded samples

Sample	TPU conc. (wt%)	O conc. (at%) (calcd.)	O conc. (at%) (exptl.)			
OBC	0	0	~0			
C_1, P_1	15	2.6	C_1	3.3±0.2	P_1	3.2±0.2
C_2, P_2	25	4.4	C_2	5.2±0.3	P_2	4.9±0.3
C_3, P_3	35	6.2	C_3	6.6±0.3	P_3	7.0±0.3
TPU	100	18.9	20.0±0.5			

Table 5.3 Surface TPU concentration

TPU conc. (wt%)	Surface concentration (%) (SEM)				Surface concentration (%) (XPS)				Surface concentration (%) (FTIR-ATR)			
15	C_1	22±3	P_1	21±3	C_1	19±1	P_1	18±1	C_1	15±0.5	P_1	15±0.5
25	C_2	34±4	P_2	32±4	C_2	29±2	P_2	28±2	C_2	25±0.5	P_2	25±0.5
35	C_3	44±4	P_3	42±4	C_3	38±2	P_3	40±2	C_3	35±0.5	P_3	35±0.5

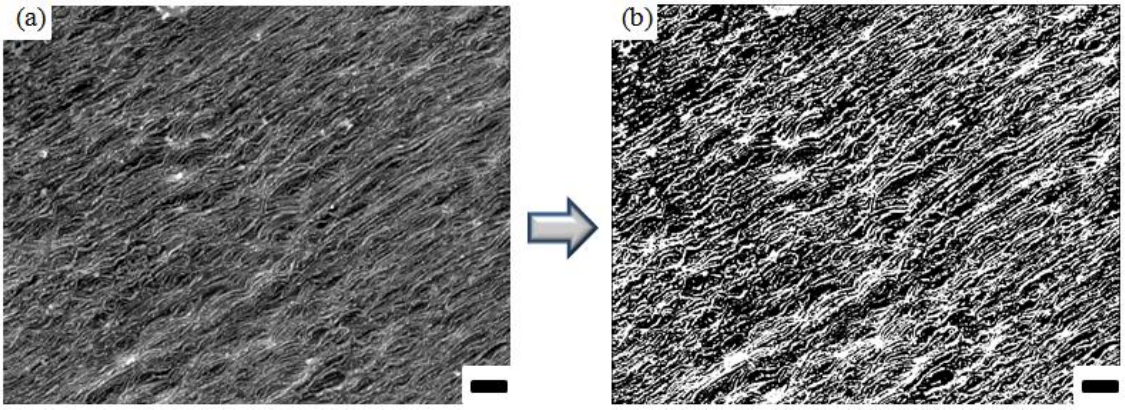

Figure 5.5 Thresholding image analysis gave 42% TPU based on area of white regions. (a) Scanning electron micrograph of free surface of TPU/OBC blend P_3. (b) Thresholding image of free surface of TPU/OBC blend P_3. Scale bars represent 2 μm.

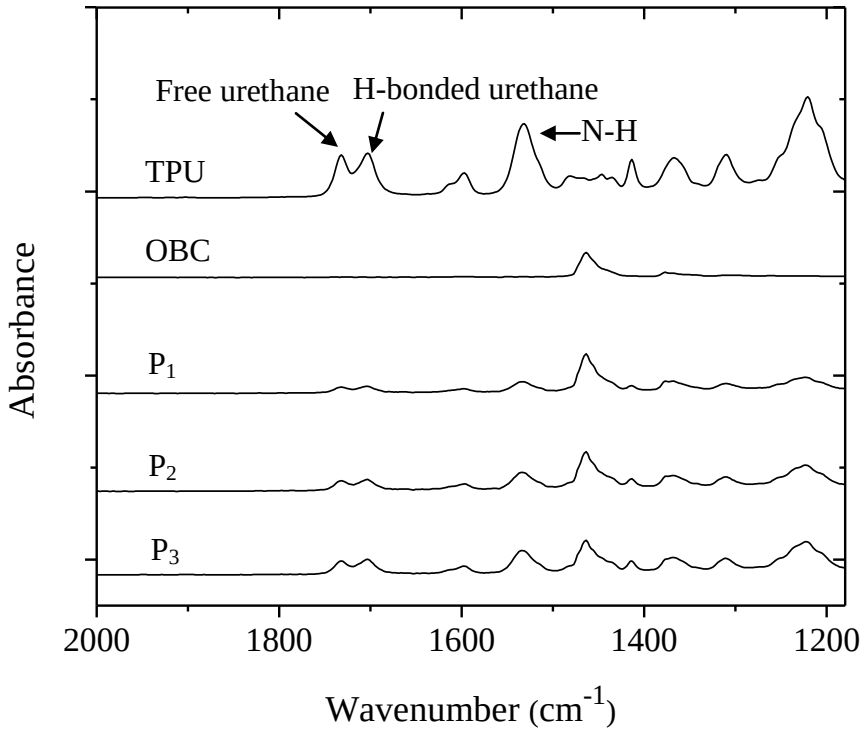

Figure 5.6 FTIR-ATR spectra of un-painted injection-molded plaque surfaces. The spectra were shifted vertically to avoid overlapping.

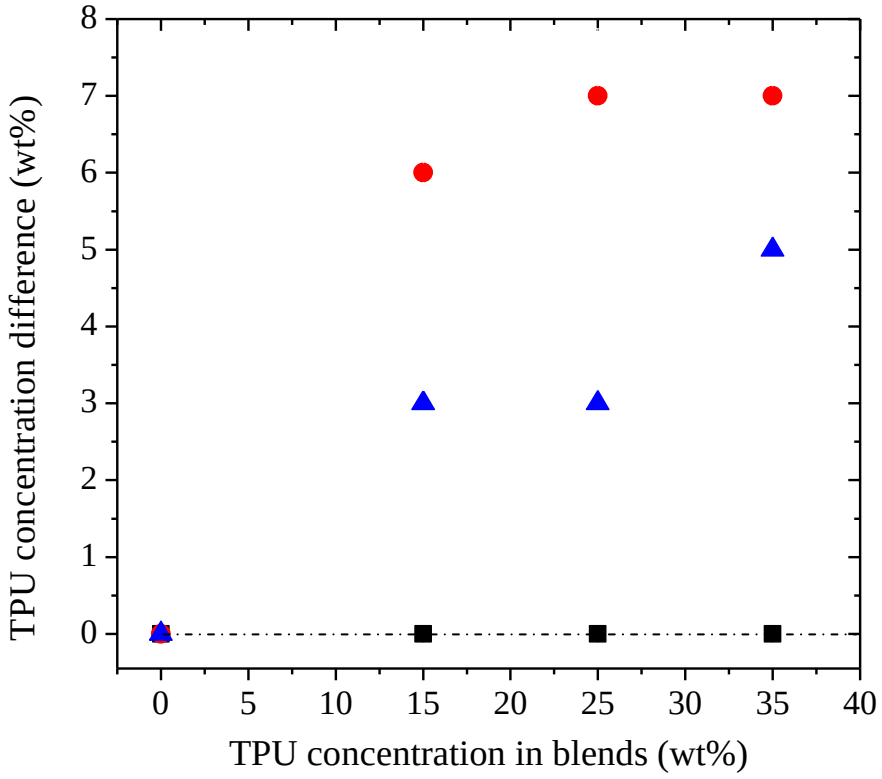

Figure 5.7 TPU concentration difference between surface and bulk of P series vs. TPU concentration in the bulk. ●: SEM; ▲: XPS; ■ FTIR-ATR.

FTIR-ATR was used to analyze the surface composition of unpainted injection molded plaques. For FTIR-ATR, the penetration depth of infrared beam into the sample surface can be calculated by using the equation below [124]:

$$d_p = \frac{\lambda / n_1}{2\pi\sqrt{\sin^2\theta - \left(\frac{n_2}{n_1}\right)^2}}$$

where, d_p is the depth penetration into the surface, λ is the wavelength of incident light, θ is the effective angle of incidence, n_2 is the refractive index of sample, n_1 is the refractive

index of crystal. For the infrared beam 4000-400 cm^{-1} (30-2.5 μm), d_p falls into the range of 0.5-5 μm for TPU/OBC blends in this study.

The collected spectra in Fig. 6 were normalized with respect to the absorbance of the aliphatic C-C stretching at 2796 cm^{-1}. The absorption band at 1732 cm^{-1} corresponds to the carbonyl stretching in a free urethane linkage, while the band at 1703 cm^{-1} is due to the presence of hydrogen bonded urethane [125-127]. The spectra of all the C and P samples were essentially identical for blends with the same amount of TPU concentration.

The peak area from 1666 cm^{-1} to 1760 cm^{-1} (free urethane and hydrogen-bonded urethane linkages [125-127]) was calculated for each sample and normalized with respect to the peak area of pure TPU sample. In this way, the surface TPU concentration was calculated from FTIR-ATR characterization and reported in Table 5.3. The surface concentration of TPU from FTIR-ATR matches that of the bulk material, indicating that the blend composition within 5 μm with respect to the outermost surface is essentially the same as the bulk material.

The TPU composition difference between surface and bulk was plotted as a function of TPU bulk concentration in Figure 5.7. The surface concentration determined from both SEM and XPS typically agreed to within 15%, both indicating slight enrichment of TPU on the outermost surface of injection molded polymer substrates compared with the bulk.

The difference of surface composition between the outermost surface and bulk can be effected by the viscosity ratio during the filling process in injection molding of polymer blends [128]. Karger-Kocsis et al. [129] studied the surface composition of injection-molded polypropylene (PP) blends modified with ethylene/propylene/diene terpolymer (EPDM) and thermoplastic polyolefin rubber (TPO). They found the outermost layer consisted of a thin, pure PP layer. The same phenomenon were also observed in injection-molded PP/(ethylene-propylene) copolymer (EPR) blends. The surface enrichment is induced by the lower viscosity of PP phase in these studies [130]. However in our study, the viscosities of both polymers are closely matched [131]. We speculate that the surface enrichment of polyurethane is induced by adhesion of polymers to the wall. The surface

of stainless steel has a thin but stable and passive chromium-rich oxide film [132]. It is well known that the outermost surface of an oxide film is covered with a layer of hydroxyl goups [132]. During injection molding, fountain flow at the advancing front brings the molten polymer blends in contact with the cold mold wall where they freeze immediately. Polyurethane has better adhesion to the metal oxide film of the injection molds compared to polyolefins, because of its high polarity and possible reactions between the released isocyanate groups from polyurethane with hydroxyl groups attached to the mold [48], resulting in the small surface enrichment of polyurethane that we observed.

5.5 CONCLUSIONS

Adhesion of a PU-based paint to TPU/OBC blends was examined by studying blend morphologies near paint / polymer interface and the surface composition of substrates in order to determine the fundamental mechanism of paint adhesion. Blends with TPU concentrations of 25 wt% or greater show significant improvement on paint adhesion and high connectivity of the TPU with the top paint layer, whereas incomplete wetting and gaps in the coating were observed for lower concentrations. Interfacial polyurethane inter-diffusion was proposed as the mechanism for PU paint to TPU/OBC substrates. In addition, the outermost surface compositions of injection molded plaques were quantitatively measured by scanning electron microscopy (SEM) and x-ray photoelectron microscopy (XPS). Both showed slight enrichment of TPU on the outermost surface. This is attributed to the better adhesion of polyurethane with the wall of the injection molder. FTIR-ATR, nonetheless, generated collective information including all the material from the outermost surface down to the depth of 5 μm. It showed that the composition below the outermost surface is the same as the bulk material due to the viscosity matching between the two polymers.

CHAPTER 6

Blends of Polyolefin/ PMMA for Improved Scratch Resistance, Adhesion and Compatibility

6.1 OVERVIEW

Functionalized poly(propylene-*co*-ethylene) (PPE) made via reactive extrusion dramatically improved the performance of their blends with poly(methyl methacrylate) (PMMA). Adhesion, compatibility, hardness and scratch resistance were all increased greatly expanding the applications of polyolefins. Three types of functional PPEs including maleic anhydride grafted PPE (PPE-MA), hydroxyl group grafted PPE (PPE-OH) and secondary amine group grafted PPE (PPE-NHR) were melt blended with PMMA at different compositions and with PMMA of different molecular weights. Compatibility of each functional PPE with PMMA was compared by investigating the binary blends using mechanical (nano-indentation, nano-scratch and tensile tests), rheological (dynamic temperature ramp), morphological (scanning electron microscopy with image analysis, particle size analysis) and adhesion tests. Improvements on hardness, modulus, scratch resistance, particle dispersion and adhesion were observed for blends with functional PPEs compared to non-modified PPE. Compatibility of functional PPEs with PMMA is confirmed consistently from various tests and ranked in a decreasing order as follows: PPE-NHR > PPE-OH > PPE-MA > PPE, which is attributed to different reactivities of functional groups with ester linkages on PMMA. We also drastically improved the compatibility and adhesion between polyolefin and PMMA by blending a PMMA grafted PPE copolymer.

6.2 INTRODUCTION

Despite the wide usage of polyolefins, they suffer from relatively poor adhesion and compatibility with more polar polymeric materials, due to their intrinsic low polarity. In an effort to enhance the properties of polyolefins, e.g., adhesion, paintability, and impact strength, blends of polyolefins with polar polymers have received attention as an industrially relevant route over the past decades. Polymer blends offer a means to achieve property combination that is generally not available in any single polymeric material.

As polyolefins are not miscible with polar polymers, compatibilization is required to obtain maximum synergy by improving interfacial activity in heterogeneous polymer blends. Compatibilization can be achieved by adding a block or graft copolymer of the two polymer components in the blend or by forming such a copolymer through covalent or ionic bonds *in situ* during blending. The latter strategy is also known as reactive compatibilization.

This study investigated both reactive compatibilization and adding premade copolymers to generate compatibilized polyolefin/ PMMA blends in order to improve polyolefin's scratch resistance. The ability of polyolefin's surfaces to resist scratching is particularly important in coatings for automotives, building materials, and many other applications. PMMA is well known for its high mechanical strength, optical transparency, and excellent UV resistance, which makes it an excellent candidate for polyolefin's scratch improvement. However, there is no report on improving polyolefin's scratch resistance by reactive compatibilization or pre-adding copolymers in open literature.

Although some researchers have proposed the synthesis of PMMA-grafted polyolefins with controlled radical polymerization (CRP),[133-136] the efficiency of these copolymers as compatibilizers has not been explored. While two reports indicate some improvement in the mechanical properties of polyolefins by blending with PMMA,[137,138] very limited information is given regarding the properties of the products. There are also no reports on reactive compatibilization of polyolefins and PMMA. To our knowledge stabilized blends of PMMA with polyolefins have never been achieved.

We will attack the problem of compatibilizing such blends using both pre-made compatibilizers and reactive compatibilization. We show that blends made with these compatibilizers can significantly improve polyolefin's scratch resistance and adhesion. In the present study an attempt on the effect of in situ compatibilization on scratch resistance behaviour of PPE/PMMA blends has been made with an aim to correlate the mechanical, morphological and rheological behaviour of the PPE/PMMA blend system. This study will also illustrate the capabilities of a nanoindentation/nanoscratch tester to assess mechanical and tribological properties of polyolefins.

6.3 EXPERIMENTAL

6.3.1 Materials

Poly(propylene-*co*-ethylene) copolymers (VERSIFY^{TM} 4301), PPE, was provided by The Dow Chemical Company. This copolymer has 11-12 wt% ethylene with a melt flow rate (MFR) of 25 grams/10 min (230 ℃; 2160g) as measured by ASTM D 1238 and density of 0.868 g/cm^3 as measured by ASTM D 792. The anhydride-functionalized poly(propylene-*co*-ethylene) copolymer (PPE-MA) was prepared by free radical grafting of maleic anhydride onto another grade of poly(propylene-*co*-ethylene) copolymer (VERSIFY^{TM} 2400) with 14-15 wt% ethylene in the melt using continuous reactive extrusion described in detail elsewhere.[42] The MFR of PPE-MA was ~80 g/10 min and the anhydride content was determined to be 0.80 wt% by a calibrated FT-IR analytical method. 0.80 wt% corresponds to about one succinic anhydride group per 1000 -CH_2- units on the polyolefin backbone. The hydroxy- and amino-functional analogs were then prepared directly from PPE-MA by reactive extrusion with 2-aminoethanol and N-methyl-1,3-propanediamine as described by Silvis et al. [42] The relative concentrations of OH and NHR functionalities, N-(2-hydroxyethyl)-succinimide and N-(3-(N-methylamino)-1-propyl)-succinimide were 1.15 wt% and 1.36 wt%, respectively, based on complete conversion of the anhydride to functionalized imide as determined using FT-IR spectroscopy (anhydride C=O at 1790 cm^{-1}; imide C=O at 1705 cm^{-1}). Due to chain

scission effects during maleation reaction, the MFR increased to ~80 g/10min after grafting with maleic anhydride, however, the density and ethylene content were essentially unchanged. Conversion of MA to OH or NHR did not alter the MFR any further. The structures of PPE and functional PPEs are given in Figure 6.1. The properties of these materials, along with the two types of PMMA studied, are shown in Table 6.1. PMMA-1 (V825-NA) was provided by Arkema; PMMA-2 was purchased from Aldrich.

Table 6.1 Molecular characteristics of polymers used

Sample	Mn (kg/mol)	Mw (kg/mol)	PDI	T_m[a] (℃)	Modulus (MPa)	Hardness (MPa)	η_0[b] (Pa•s)
PPE-MA	49.8	92.7	1.86	55	49	8	1.3×10^2
PPE-OH	61.0	104.6	1.71	55	46	7	1.7×10^2
PPE-NHR	63.1	108.4	1.72	55	45	6	1.9×10^2
PPE				64	43	6	3.9×10^2
PMMA-1[c]	63.3	92.7	1.46	-	4.3×10^3	2.6×10^2 [d]	2.5×10^4
PMMA -2[d]	9.53	15.4	1.62	-	1.5×10^3	41[d]	0.8×10^2
PPE-*g*-PMMA[e]	72.2	238.6	3.30	-	-	-	-

[a] onset of melting

[b]zero shear viscosity measured at 210 ℃

[c]molecular weights measured by GPC at room temperature using polystyrene standards

[d]data obtained by taking the average of defined range

[e]molecular weights measured by high temperature GPC at 160 ℃ with polystyrene standards

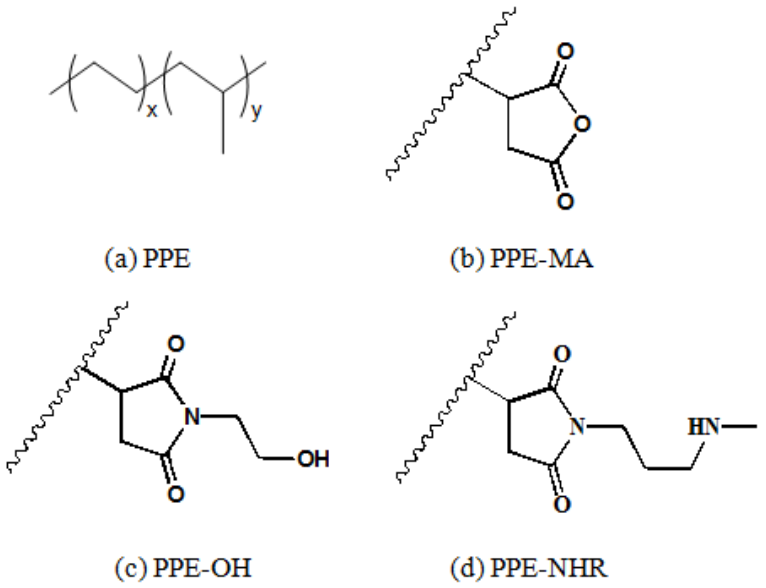

Figure 6.1 Structures of the functional polyethylenes used in this study. (a): PPE, poly(propylene-*co*-ethylene) x/(x+y)= (7.3-8) %; (b): Succinimide grafted poly(propylene-*co*-ethylene) (PPE-MA); (c): N-(2-hydroxyethyl)-succinimide grafted poly(propylene-*co*-ethylene) (PPE-OH); (d):N-(3-(N-methylamino)-1-propyl)-succinimide grafted poly(propylene-*co*-ethylene) (PPE-NHR). The small jagged chains in (b), (c), (d) represent poly(propylene-*co*-ethylene) backbones.

6.3.2 Synthesis of PPE-*g*-PMMA

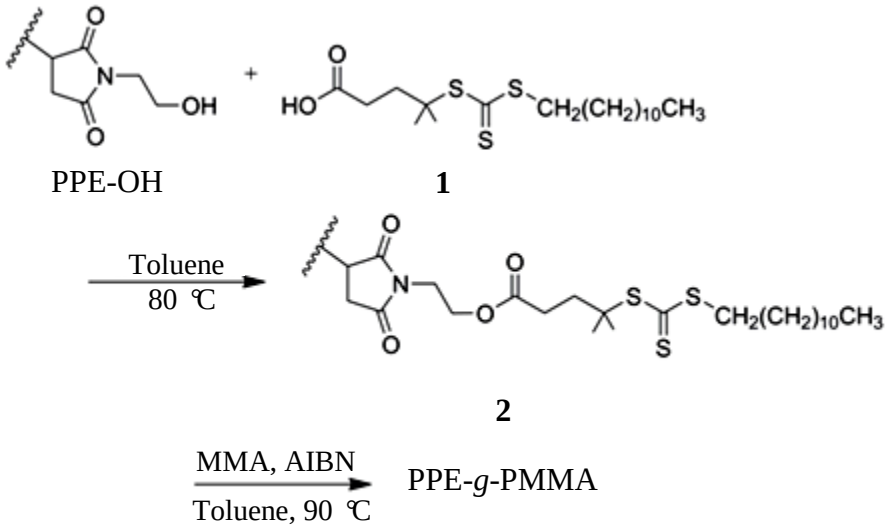

Scheme 6.1 Synthesis of PMMA grafted PPE (PPE-*g*-PMMA) from PPE-OH.

PMMA grafted PPE copolymer (PPE-g-PMMA) was synthesized by reversible addition−fragmentation chain transfer polymerization (RAFT) starting from PPE-OH. ACS reagent grade starting materials and solvents were used as received from commercial suppliers without further purification unless otherwise stated. Under an argon atmosphere, $(COCl)_2$ (2.4 mL, 28 mmol) was added by syringe to compound **1** (0.95 g, 2.6 mmol) at room temperature with rapid stirring, causing the vigorous evolution of CO_2(g), CO(g), and HCl(g). It should be noted that poisonous and corrosive gases were generated during this process. After about 5 h, the evolution of gases ceased and a homogeneous phase was observed. Excess $(COCl)_2$ was removed in vacuo to yield acyl chloride. Then 1 g of PPE-OH and 1 g of acyl chloride version of compound **1** were reacted in 30 mL of toluene at 80 ℃ to generate compound **2**. 0.3 g of PP-RAFT, 0.3 g of MMA and 2 mg of AIBN were dissolved into 1 mL of toluene. After the solution was degassed using freeze-pump-thaw cycles, the polymerization was performed at 90 ℃ for

18 h. The polymer yield was 0.42 g (70%, based on the total materials) and MMA conversion by NMR was determined to be 54%.

Preparation of PPE-X/PMMA Blends (X=MA, OH, NHR)

PPE-X/PMMA blends were prepared in a recirculating, conical twin screw extruder (DACA Instruments, 4g capacity) at 200rpm and temperature of 210 ℃ with nitrogen purge. After mixing for five minutes, the blends were extruded and collected.

6.3.3 Characterization

Nano-indentation test

Nano-indentation was performed using a dynamic contact modulus Nano Indenter (Nano Indenter XP, MTS). The indentation load-displacement behavior of PMMA, PPE materials and their blends were tested with a Berkovich indenter to determine hardness and elastic modulus. The samples were films made from compression molding and mounted on an Al puck with superglue. For the indenting test, the loading process was controlled by an allowable drift rate of 0.2 nm/s. The approaching velocity and the harmonic displacement of the nano-indentation tip toward a target surface were maintained at 10 nm/s and 2 nm respectively for all the testing surfaces.

Nano-scratch test

The scratch test was performed using the same Nano Indenter instrument as above. A diamond indenter with 90 ° conical geometry was used. In the scratch test, a normal force was applied on the surface at a constant rate of increase as the indenter moves a certain distance laterally, progressively increasing the applied load along from 0 to 40 mN. This test allows observing the scratch resistance behavior of the material. After the scratch test, images of the scratched surface were obtained with an optical microscope. All the operation parameters are summarized in Table 6.2.

At least three strips separated by at least 1mm to minimize interference have been scratched on the same sample in order to avoid errors caused by point defects on the surface. Penetration depth versus scratch distance as the indenter laterally moves on the surface was recorded to evaluate scratch resistance. After each scratch test, the indenter traverses the area to test while applying a minimum load and recording the contours of the surface. By comparing the profiles during and after the scratching, changes in depth on the scratched surface can be detected.

Table 6.2 Parameters for nano-scratch test

Parameter	Quantity
Scratch length	500 μm
Scratch velocity	10.000 μm/s
Maximum scratch load	40.000 mN
Profiling acquisition rate	5.000 Hz
Starting scratching load	0.000 mN
Scratch acquisition rate	5.000 Hz

Scanning electron microscopy (SEM)

SEM images were taken with a JEOL 6500 scanning electron microscope with a field-emission gun. Polymer blends were quenched and fractured in liquid nitrogen immediately after they were extruded so that the morphology could be preserved. All SEM samples were then sputter coated with platinum to a thickness of approximately 75 angstroms to make them conductive. Electron beam current and potential were varied for optimal imaging. The particle size analysis of the blends was performed on cryogenically fractured samples.

Tensile test

A MINIMAT tensile tester (Rheometric Scientific) with an extension rate of 1 mm/s was used to investigate the tensile properties of the blends. Tensile testing of compression molded dogbone samples (12 mm gage length, 0.5 mm gage thickness, 3 mm gage width) was conducted on a Rheometrics Scientific Minimat instrument. Functional PPE/ PMMA-1 dogbone samples were prepared by compression molding from pellets at 210 ℃ under 2 MPa between two polytetrafluoroethylene (PTFE) coated aluminum foils (Saint-Gobain Performance Plastics). They were dried in a vacuum oven at room temperature before test.

Differential scanning calorimetry (DSC)

Differential scanning calorimetry was performed on a TA DSC Q1000 utilizing an indium standard for temperature calibration. At least 4 mg of sample contained in hermetically sealed aluminum pans were analyzed under N_2 with a 10 ℃/min heating rate. Thermal transition temperatures were determined from the second heating after annealing above the glass transition or melting point for at least 1 min to erase thermal history.

High Temperature Gel Permeation Chromatography

The PL-GPC 220 integrated high temperature GPC system (Agilent Systems) was used to measure the molecular weights and distribution of PPE materials. Trichlorobenzene (TCB) with 0.0125 wt% of butylated hydroxytoluene (BHT) was used as eluent phase with flow rate 1.0 ml/min at 135 ℃. The data were analyzed against a polystyrene standard calibration using the following Mark-Houwink parameters:
Polystyrene in TCB: $K=12.1\times10^{-5}$ $\alpha=0.707$

Polypropylene in TCB: $K=19.0\times10^{-5}$ $\alpha=0.725$

Adhesion test

In order to test the capabilities of functional PPEs and PPE-*g*-PMMA as adhesion promoters, they were coated between PPE and PMMA, and annealed at 180 ℃. The adhesion between PPE and PMMA was then tested. First all the functional PPEs were dissolved in benzene at 80 ℃ (0.03g/ 13ml), and then the temperature of the solution was lowered to 50 ℃. Premade PMMA films were dipped into the solution for 5 seconds and then dried in fume hood. Then coated PMMA film and premade PPE film were pressed into intimate contact (sandwiched between two polytetrafluoroethylene (PTFE)-coated aluminumfoils) and laminated for 100 seconds at 180 ℃ under 0.1 MPa pressure. The bilayer samples were cooled down by water to room temperature. The 180° peel tests were performed on the same MINIMAT Tensile tester at an extension rate of 0.33 mm/s and a total travel of 50 mm.

6.4 RESULTS AND DISCUSSION

6.4.1 Nano-indentation and nano-scratch tests

We blended PMMA-1 with PPE and three types of functional PPEs, namely maleic anhydride grafted PPE (PPE-MA), hydroxyl group grafted PPE (PPE-OH) and secondary amine group grafted PPE (PPE-NHR) at first. Then we evaluated the mechanical property and compatibility of resulting blends by using nano-indentation tests, nano-scratch tests, tensile tests, rheological characterization, SEM and adhesion tests.

The nanoindenter instrument can perform both nano-indentation and nano-scratch tests with a single head equipped with different shaped diamond indenters, namely

Berkovich indenter for indentation test and 90 ° cone indenter for scratch test. Each indentation test accurately measures hardness and elastic modulus, and each scratch test provides additional insight into the material's scratch resistance behavior.

In a nano-indentation test,[139-141] an indenter tip is driven into the sample by applying an increasing load up to some preset value. The load is then decreased until partial or complete relaxation occurs. The young's modulus of PMMA-1 was determined to be 4.3 GPa. When it was blended into various PPE materials, as shown in Table 6.3, non-modified PPE only has slight increase of modulus and hardness. However, for all the initial modified PPEs, the modulus and hardness increased by at least 100% via blending with PMMA compared with the PPEs without PMMA shown in Table 6.1. We attribute this behavior to the interfacial bonding between PMMA and complementary functional groups on the modified PPE backbones. The rigid PMMA particles provide enormous resistance to tensile force as the young's modulus of PMMA is several orders of magnitude larger than PPE materials. PPE-NHR gave the best improvement, almost three times larger, suggesting the highest reactivity of secondary amine towards the PMMA ester group among the three.

For nano-scratch test, as shown in Figure 6.2, the normal force increased linearly up to 40 mN and the indenter moves laterally on the surfaces to be tested. All the single PPE materials show very similar resistance to the normal force. Penetration depth increases linearly with force for PPE and functionalized PPE materials. However, dramatic changes were observed after PMMA was blended. Even with a weak interfacial interaction, PPE/ PMMA-1 present a significant resistance to the scratching normal force. Starting from scratch distance ~ 250 μm, the indenter could no longer penetrate into the material even with increased forces. Instead, the indenter's vertical decent was stalled after 250 μm. It is remarkable that functional PPEs generated even more scratch resistance, in the following order: PPE-NHR > PPE-OH > PPE-MA.

As shown in Table 6.4, for the original PPE materials, the penetration depth at 550 μm increased about 50 % compared with the value at 350 μm. For instance, the penetration depth for PPE-NHR increased from 29.2 μm at scratch distance of 350 μm to 43.5 μm at scratch distance of 550 μm. Nonetheless, for polymer blends, the penetration depth at 550 μm is almost 30 % lower than the values at 350 μm while the normal force kept increasing. In particular, the PPE-NHR/PMMA-1 blend provided dramatically larger repulsive force in contrast to unmodified PPE-NHR. For the blend PPE-NHR/PMMA-2 (70/30), although strongest interfacial bonding is expected among three functional groups, this blend did not generate as strong scratch resistance as PPE-NHR/PMMA-1(70/30), where high molecular weight PMMA-1 was used. Although lower molecular weight PMMA-2 gave rise to much finer morphology and matched viscosity with PPE materials, the mechanical property was deteriorated, as shown in Table 6.3, because the molecular weight of PMMA-2 was lower than PMMA's entanglement molecular weight.

Figure 6.3 (a) presents an example of how the visual picture would change for the scratched surface once PMMA was blended. It illustrates that the scratch in PPE-NHR is much more visible than the scratch in PPE-NHR/PMMA blends in Figure 6.3 (b). While the scratch of PPE-NHR was clear and there was an obvious pile up of polymers, the scratch of blends was narrower at the beginning of scratching compared with PPE-NHR and smeared at surface when the force increased. It should be noted, as shown in Table 6.4, in terms of residual depth of scratch, which is the contour of scratched mark detected at a minimum load after scratching, the blends have a generally lower residual scratch depth than the original PPEs.

Figure 6.4 confirmed the ranking order determined from nano-indentation and nano-scratch test. While the ultimate elongation of all PPE materials falls beyond the instrument limitation, the blends also showed quite significant elongation despite of being smaller than the pure PPE. PPE-NHR, again, gave the best improvement in terms of ultimate elongation and elastic modulus, followed by PPE-OH, PPE-MA and non-modified PPE. It is quite remarkable that at strain 100 %, the stress that can be achieved

by PPE-NHR/ PMMA-1 blend outnumbered the other blends by more than 50 % and compared with the pure PPE-NHR by 30 %.

Xiang et al.[142] studied scratch behaviors of a broad range of polymers to understand how the material characteristics of a polymer affect the scratch resistance. They found that tensile tear is responsible for the brittle fracture mode during scratch, especially for brittle materials, which leads to cracks and crazes. However, for elastomers used in our research, shear yielding is the dominant factor resulting in scratch damage. For shear yielding, modulus, yield stress and friction coefficient determine the scratch resistance. Obviously, increased modulus and yield stress in the modified PPE/PMMA blends lead to better shear yielding resistance. As a result, scratch resistance of PPE and functionalized PPEs were increased after blending PMMA.

Table 6.3 Modulus and Hardness determined from nano-indentation tests.

Sample	Modulus (MPa)	Hardness (MPa)
PPE/ PMMA-1 (70/30)	57	8
PPE-MA/ PMMA-1 (70/30)	94	13
PPE-OH/ PMMA-1 (70/30)	98	14
PPE-NHR/ PMMA-1 (70/30)	113	18
PMMA-1	4.3×10^{3}	2.6×10^{2}
PMMA-2	1.5×10^{3}	40

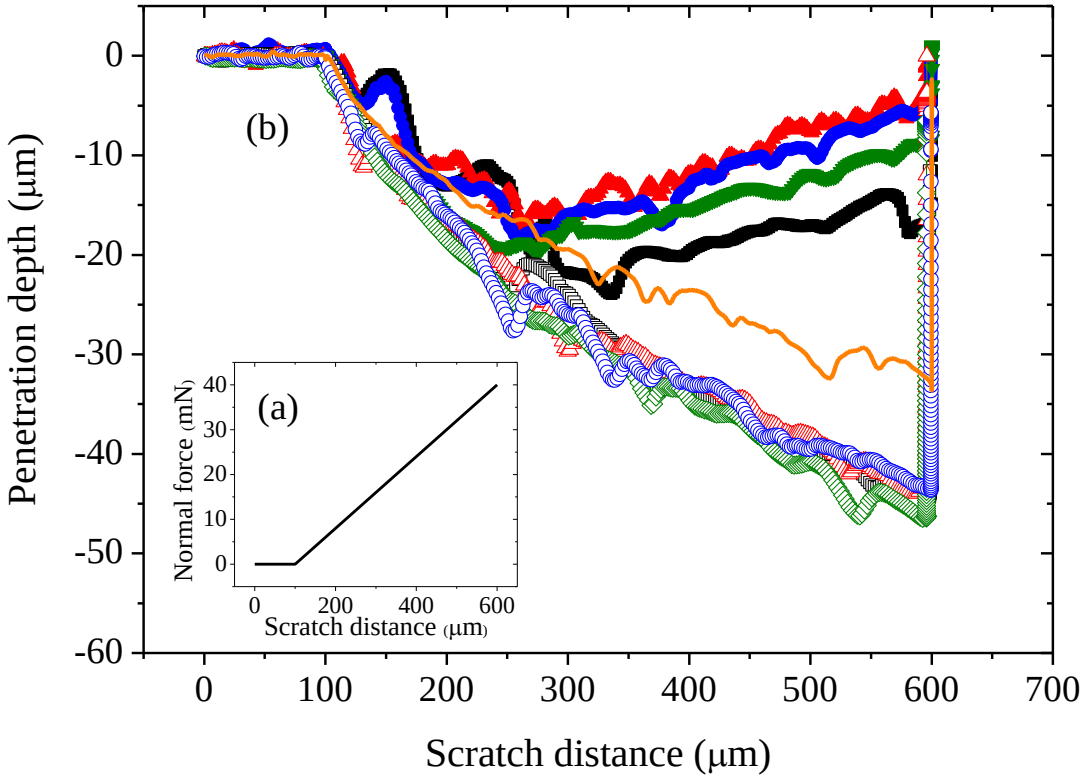

Figure 6.2 (a) Normal force vs. scratch distance in nano-scratch tests. A normal force applied on the surface increased at a constant rate as the indenter moves laterally. The same force change is universally applied to all the tested surfaces. (b) Penetration depth vs. scratch distance in nano-scratch tests for different materials. △**:** PPE-NHR; ○: PPE-OH; ◇:PPE-MA; □: PPE (Note these the penetration curves of these four materials almost overlapped with each other.)▲: PPE-NHR/PMMA-1 (70/30); ● : PPE-OH/PMMA-1 (70/30); ◆: PPE-MA/PMMA-1 (70/30); ■: PPE/ PMMA-1 (70/30);——: PPE-NHR/PMMA-2 (70/30).

Table 6.4 Penetration depth and residual depth at different scratch distances for nano-scratch tests

Sample	**Penetration** depth at scratch distance 350 μm (μm)	**Residual** depth at scratch distance 350 μm (μm)	**Penetration** depth at scratch distance 550 μm (μm)	**Residual** depth at scratch distance 550 μm (μm)
PPE	29.7	5.7	43.5	5.7
PPE-MA	31.1	6.0	45.4	5.9
PPE-OH	32.4	6.1	42.6	6.0
PPE-NHR	29.2	5.5	43.5	5.2
PPE/ PMMA-1 (70/30)	20.5	4.5	9.8	4.5
PPE-MA/ PMMA-1 (70/30)	17.8	4.1	9.0	4.0
PPE-OH/ PMMA-1 (70/30)	15.4	3.5	5.9	3.0
PPE-NHR/ PMMA-1 (70/30)	12.9	3.0	5.4	3.0
PPE/ PMMA-2 (70/30)	18.5	5.4	36.9	5.2
PPE-NHR/ PMMA-2 (70/30)	21.5	4.5	30.8	4.1

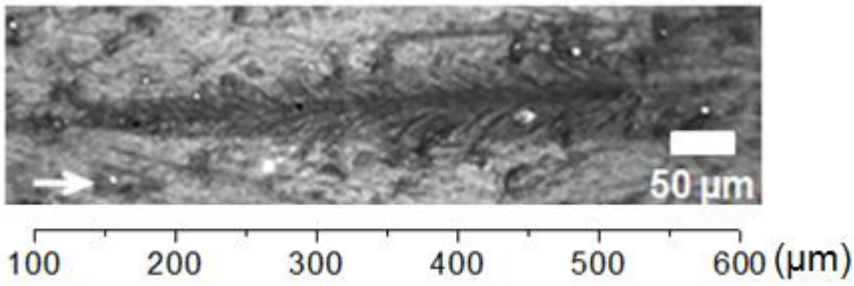

(a) PPE-NHR

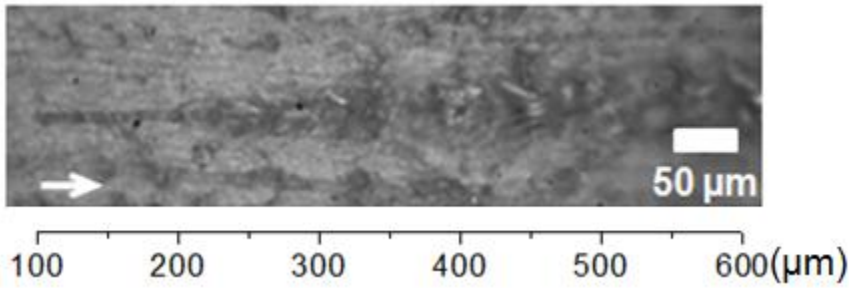

(b) PPE-NHR/ PMMA-1 (70/30)

Figure 6.3 (a) Optical micrograph of a scratch path made over the surface of PPE-NHR; (b) The scratch path over the surface of PPE-NHR/PMMA-1 blend (70/30) is less visible. Arrows indicate the scratch direction.

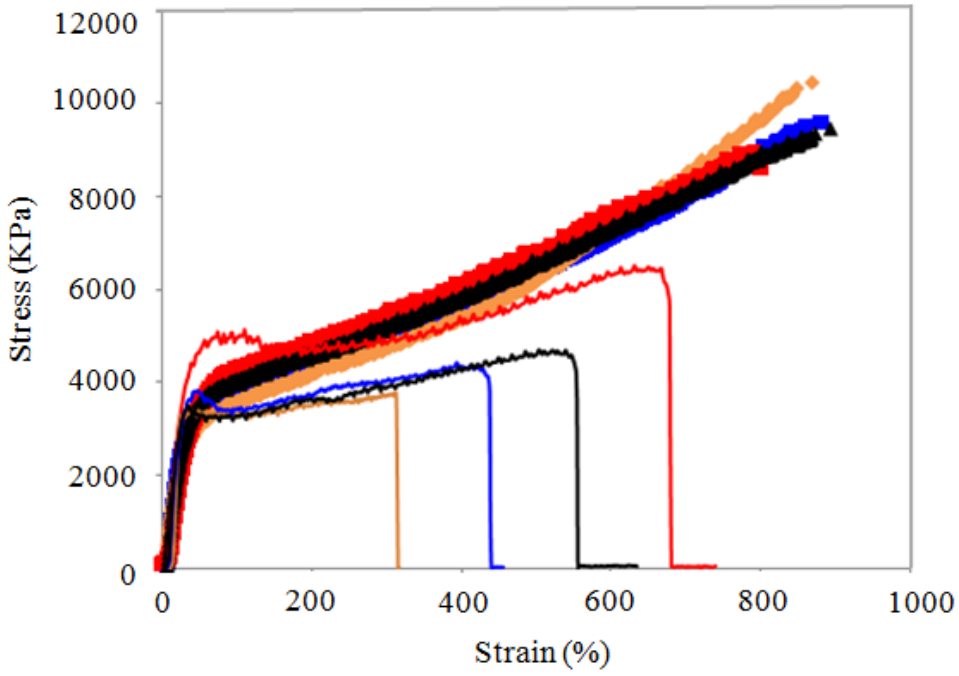

Figure 6.4 Stress-strain curves for PPE, functional PPEs and their blends with PMMA-1. ■: PPE-NHR; ▲: PPE-OH; ■: PPE-MA; ◆: PPE; (Note the stress-strain curves of these materials almost overlapped with each other.) ——: PPE-NHR/PMMA-1 (70/30); ——: PPE-OH/PMMA-1 (70/30); ——: PPE-MA/PMMA-1 (70/30); ——: PPE/PMMA-1 (70/30).

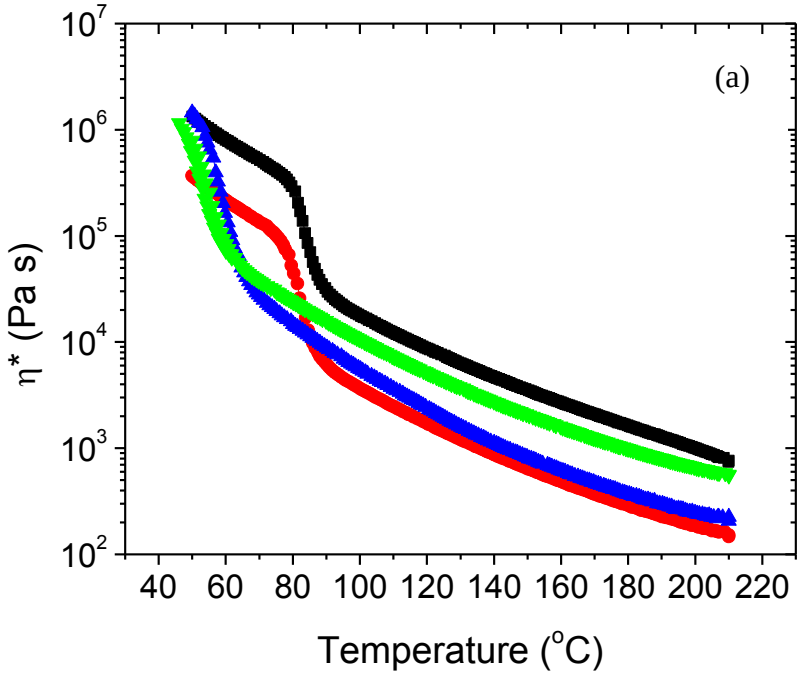
(a)
η* (Pa s)
Temperature (°C)

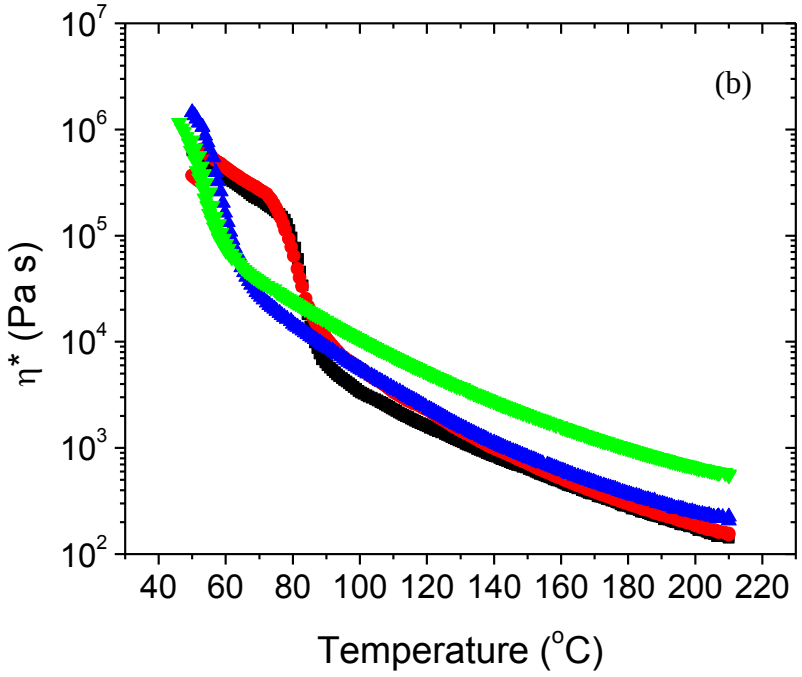
(b)
η* (Pa s)
Temperature (°C)

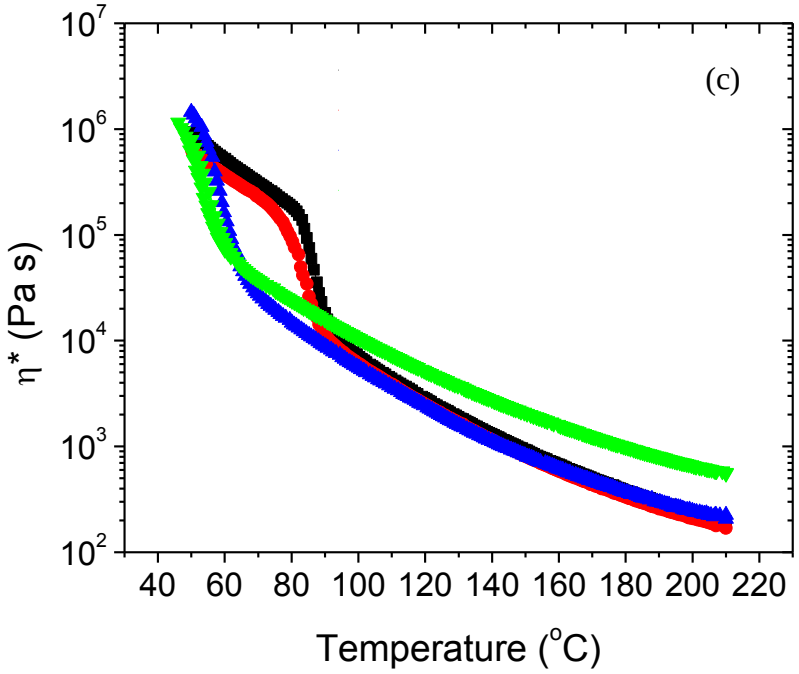

Figure 6.5 Dynamic temperature ramp (complex viscosity vs. temperature) for PPE and PMMA blends. (a) ■:PPE-NHR/PMMA-1 (70/30); ●: PPE-NHR; ▲:PPE/PMMA-1 (70/30); ▼: PPE. (b) ■:PPE-MA/PMMA-1 (70/30); ●: PPE-MA; ▲:PPE/PMMA-1 (70/30); ▼: PPE. (c) ■:PPE-OH/PMMA-1 (70/30); ●: PPE-OH; ▲:PPE/PMMA-1 (70/30); ▼: PPE. Note that PPE and PPE/PMMA-1 (70/30) appear in every figure for comparison purpose.

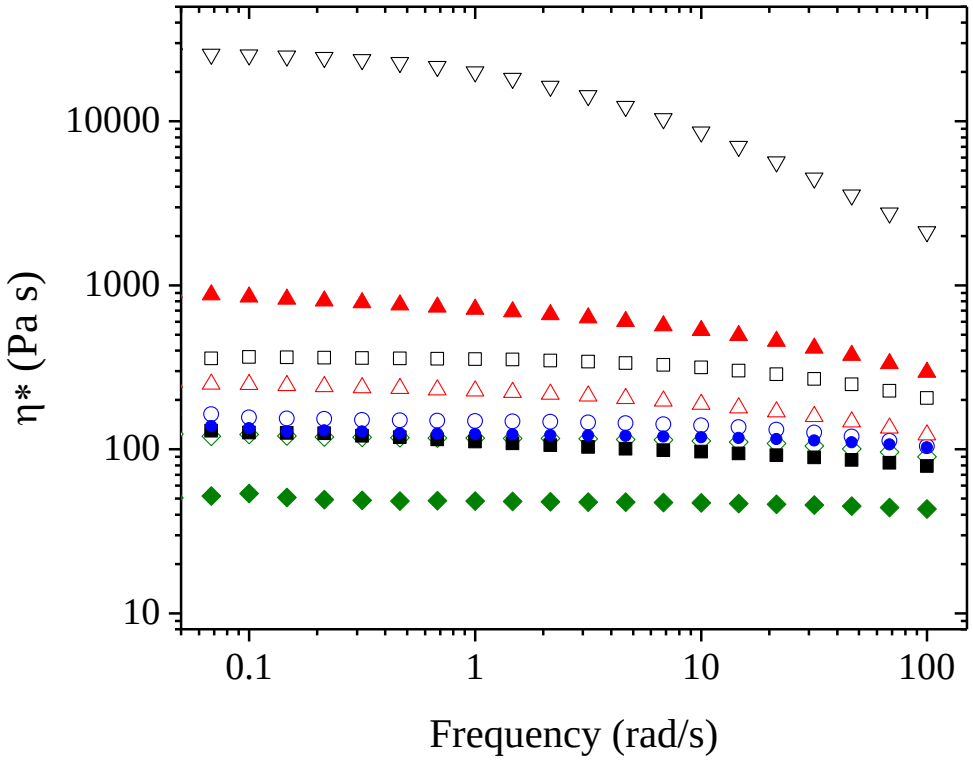

Figure 6.6 Dynamic frequency sweep tests at 210 ℃. ▽: PMMA-1△: PPE-NHR; ○: PPE-OH; ◇:PPE-MA; □: PPE ▲: PPE-NHR/PMMA-1 (70/30); ● : PPE-OH/PMMA-1 (70/30); ◆: PPE-MA/PMMA-1 (70/30); ■: PPE/ PMMA-1 (70/30).

6.4.2 Rheology

In order to understand the rheological behaviors of the PPE-X/PMMA blends and verify the compatibility of each blend, dynamic temperature test and dynamic frequency tests were carried out for both the PPE-X materials and PPE-X/ PMMA blends, as shown in Figure 6.5 and 6.6. There are at least two empirical equations that can predict the viscosity of binary polymer blends. We present them as below:

1. Additivity model:

$$\eta_m = \eta_1\phi_1 + \eta_2\phi_2$$

where η_m represents viscosity of the blend, η_1 and η_2 are the viscosities of each component, and ϕ_1 and ϕ_2 are the volume fraction. The additivity model is normally applicable to the uncompatibilized polymer blends. It assumes that the viscosity of the uncompatibilized blend is the arithmetic addition of the contributions from the viscosity of each component multiplied by their respective volume fractions.

2. Log additivity model:

$$\log\eta_m = c_1 \log\eta_1 + c_2 \log\eta_2$$

where η_m represents viscosity of the blend, η_1 and η_2 are the viscosities of each component, and c_1 and c_2 are the weight fraction. The log additivity model is based on the assumption that the viscosity of the blend is the summation of their logarithmic addition. It has been employed most frequently for prediction of viscosities for homologous polymer blends.

In Figure 6.5 (a), above 60 ℃, the complex viscosity of PPE is even higher than the blends of PPE and PMMA-1. The same trend is seen in Figure 6.6. Apparently, the viscosity of this uncompatibilized blend exhibits a significantly negative deviation when compared with various theoretical models. Since there is very weak interaction (van der Waals force) and high interfacial tension between the PPE and PMMA-1 (4.7 mN/m), the lower viscosity is possibly due to an interfacial slip between the highly uncompatibilized phases.

In contrast, the complex viscosity of PPE-NHR/ PMMA-1 blends is almost one order of magnitude higher compared with PPE-NHR over the entire temperature range tested, indicating much better compatibility than PPE/ PMMA-1. In Figure 6.5 (b), the viscosity of PPE-MA/ PMMA-1 blend almost overlaps with the single component PPE-MA, indicating the moderate compatibility of PPE-MA with PMMA. In Figure 6.5 (c), the viscosity of blend lies in between the values of pure components and is slightly higher than that of PPE-OH, showing better compability of PPE-OH than PPE-MA. Although in

Figure 6.6, the complex viscosities of PPE-MA and PPE-OH blends are lower than PPE-MA and PPE-OH, the same compatibility ranking is followed as in Figure 6.5.

It should be noted that there is a clear sharp transition of viscosity with temperature for each material in Figure 6.5. DSC with the same rate of cooling (3 ℃/min) as dynamic temperature ramp verified that the transition temperature from rheological tests corresponds to the crystallization temperature of PPE and functional PPEs. In conclusion, the ranking of PPE and functional PPEs with PMMA can be presented in below: PPE-NHR > PPE-OH > PPE-MA > PPE.

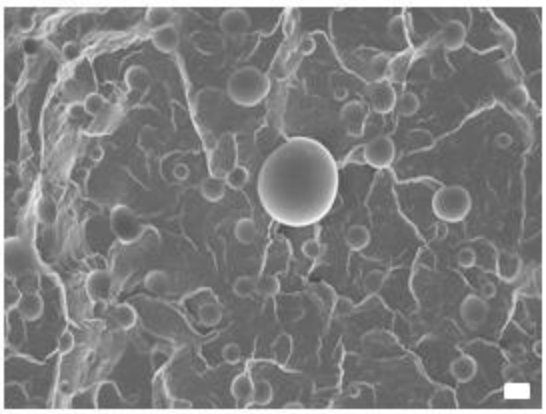

(a) PPE/ PMMA-1 (90/10)

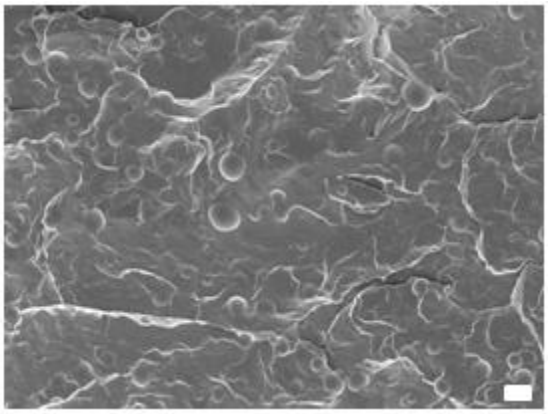

(b) PPE-MA/ PMMA-1 (90/10)

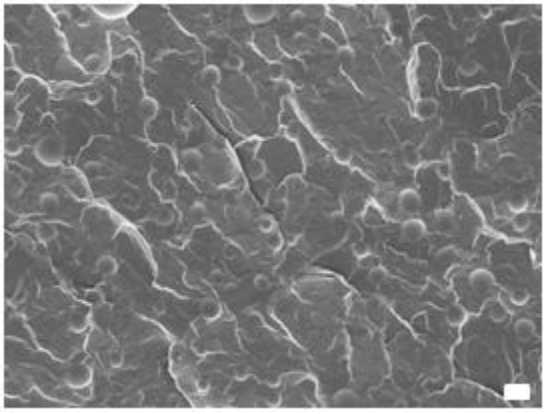

(c) PPE-OH/ PMMA-1 (90/10)

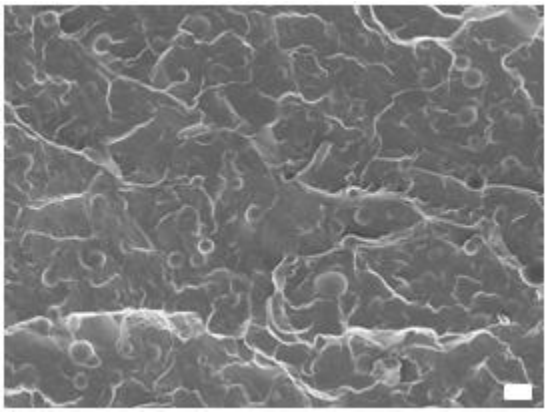

(d) PPE-NHR/ PMMA-1 (90/10)

Figure 6.7 SEM micro-photographs of cryogenically fractured surfaces. (a) Blends of PPE/ PMMA-1 (90/10); (b) Blends of PPE-MA/ PMMA-1 (90/10); (c) Blends of PPE-OH/ PMMA-1 (90/10); (d) Blends of PPE-NHR/ PMMA-1 (90/10). Scale bar represents 10 μm.

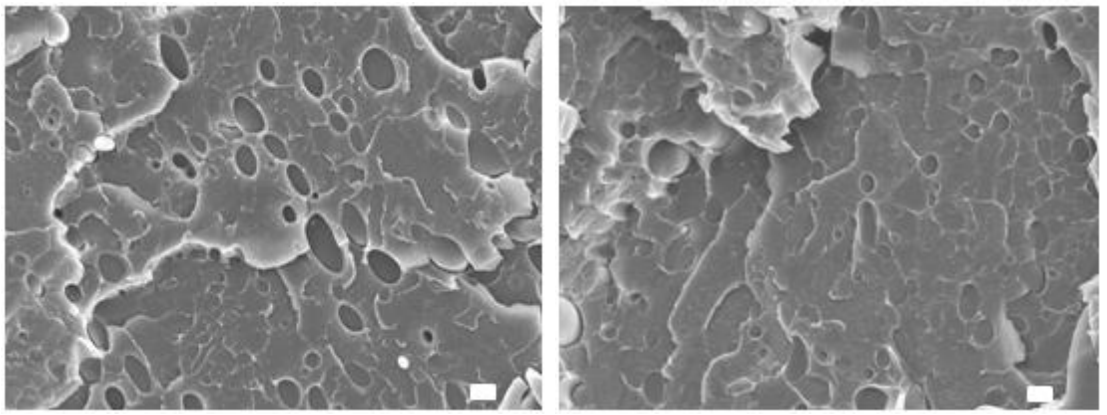

(a) PPE/ PMMA-1 (10/90) (b) PPE-MA/ PMMA-1 (10/90)

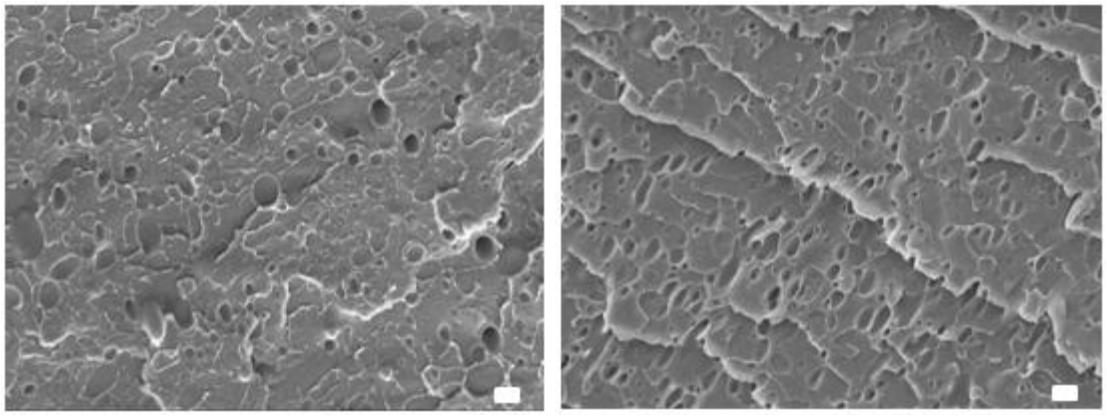

(c) PPE-OH/ PMMA-1 (10/90) (d) PPE-NHR/ PMMA-1 (10/90)

Figure 6.8 SEM micro-photographs of cryogenically fractured surfaces. (a) Blends of PPE/ PMMA-1 (10/90); (b) Blends of PPE-MA/ PMMA-1 (10/90); (c) Blends of PPE-OH/ PMMA-1 (10/90); (d) Blends of PPE-NHR/ PMMA-1 (10/90). Scale bar represents 1 μm.

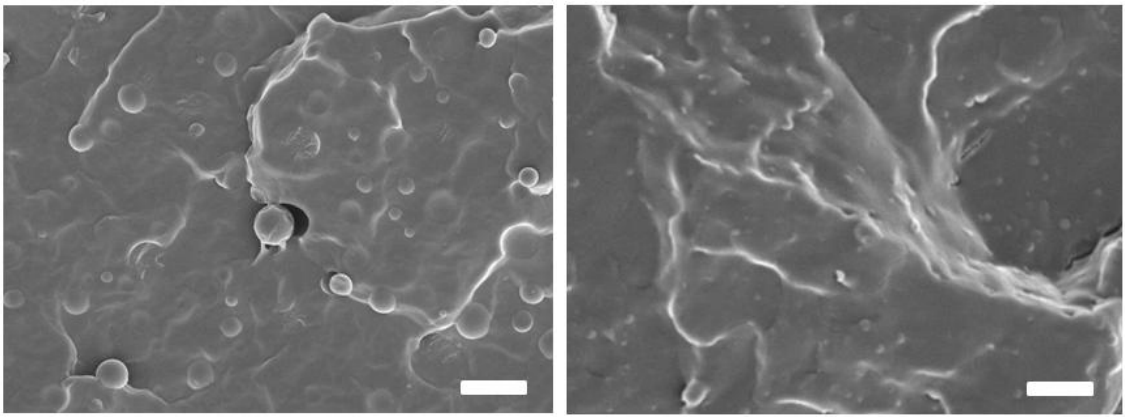

(a) PPE/ PMMA-2 (90/10) (b) PPE-NHR/ PMMA-2 (90/10)

Figure 6.9 SEM micro-photographs of cryogenically fractured surfaces. (a) Blends of (a) PPE/ PMMA-2 (90/10); (b) Blends of PPE-NHR/ PMMA-2 (90/10). Scale bar represents 5 μm.

6.4.3 Blend morphology

For PPE-X/ PMMA blends, the 90/10 and 10/90 compositions are of most interest because both morphologies are simply droplets of one phase dispersed in another. Figure 6.8 and 6.9 present the morphology of blends at 90/10 and 10/90 compositions. Figure 6.9 has the morphology of blends when low molecular weight PMMA-2 was used. Average particle size analysis was provided in Table 6.5 to facilitate quantitative comparisons. The number average diameter $<d_n>$, surface average diameter $<d_s>$, volume average diameter $<d_v>$ and the values of $<d_s>/<d_n>$ and $<d_v>/<d_s>$, which are reflections of particle size distribution, all dropped following the order of PPE, PPE-MA, PPE-OH and PPE-NHR.

Compared with non-modified PPE, although PPE-NHR showed dramatically improved dispersion and scratch resistance, the average particle size still remained at about 5 μm. Once low molecular weight PMMA-2 was added, particle size decreased dramatically as shown in Table 6.5. However, the scratch resistance was not better because the molecular weight of PMMA-2 was lower than PMMA's entanglement

molecular weight and its mechanical property was deteriorated. Results on studies conducted on the blends using PMMA of different molecular weights indicate that the blends with PMMA of high molecular weights exhibit better scratch resistance although with more coarse morphology in terms of particle size in the blends.

Table 6.5 Average particle size for different blends.

Blend	$\langle d_n \rangle^a$ (μm)	$\langle d_s \rangle^b$ (μm)	$\langle d_s \rangle / \langle d_n \rangle$	$\langle d_v \rangle^c$ (μm)	$\langle d_v \rangle / \langle d_s \rangle$
PPE/ PMMA-1 (10/90)	1.22	1.93	1.58	2.33	1.21
PPE-MA/ PMMA-1 (10/90)	0.86	1.27	1.48	1.51	1.19
PPE-OH/ PMMA-1 (10/90)	0.63	0.91	1.45	1.06	1.16
PPE-NHR/ PMMA-1 (10/90)	0.50	0.69	1.37	0.78	1.14
PPE/PMMA-1 (90/10)	12.4	20.3	1.64	28.5	1.40
PPE-MA/ PMMA-1 (90/10)	7.40	10.6	1.43	12.6	1.19
PPE-OH/ PMMA-1 (90/10)	6.50	8.97	1.38	10.1	1.13
PPE-NHR/ PMMA-1 (90/10)	4.92	6.69	1.36	7.49	1.12
PPE/ PMMA-2 (90/10)	1.45	1.94	1.34	2.13	1.10
PPE-NHR/ PMMA-2 (90/10)	0.45	0.51	1.13	0.53	1.04

a: $< d_i >$: Number average particle size; $< d_i >= \sum n_i d_i / \sum n_i$

b: $< d_S >$: Surface area average diameter; $< d_S >= \sum d_i^3 / \sum d_i^2$

c: $< d_V >$: Volume average diameter; $< d_V >= \sum d_i^4 / \sum d_i^3$

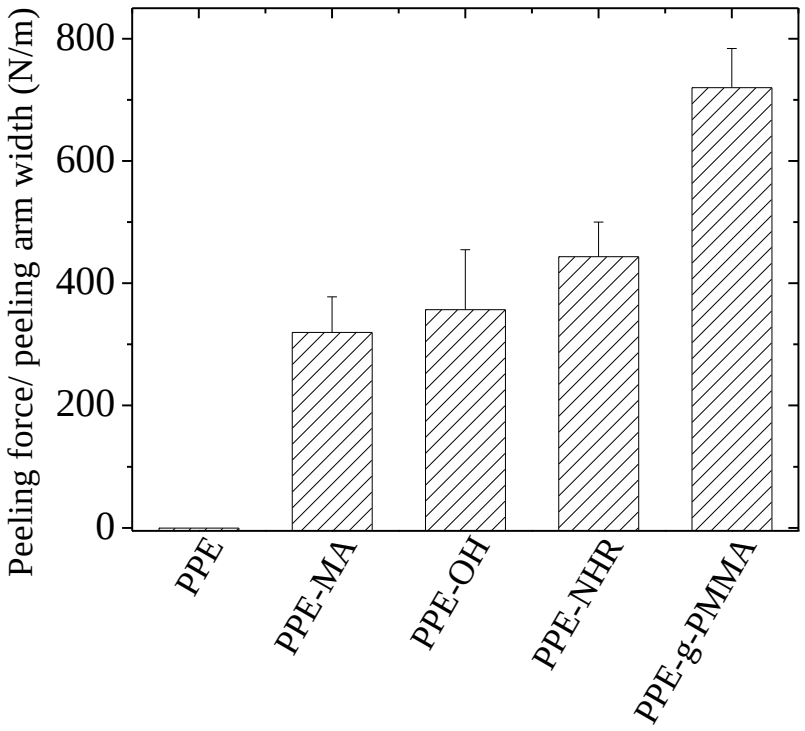

Figure 6.10 Peeling force/peeling arm width for adhesion between PPE and PMMA with various functional PPEs coated in between.

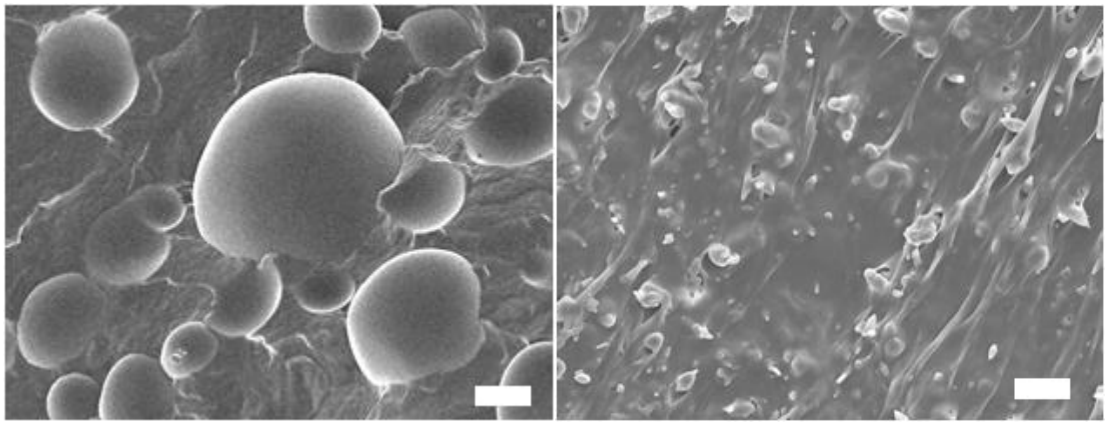

(a) PPE/ PMMA-1 (70/30) (b) PPE/ PMMA-1/ PPE-*g*-PMMA (67/28/5)

Figure 6.11 SEM micro-photographs of cryogenically fractured surfaces. (a) Blend of PPE/ PMMA-1 (70/30); (b) Blend of PPE/ PMMA-1/ PPE-*g*-PMMA (67/28/5). Scale bar represents 10 micrometers.

6.4.4 The application of PPE-*g*-PMMA

Starting from PPE-OH, we were able to graft PMMA onto PPE backbones to obtain PMMA grafted PPE (PPE-*g*-PMMA). As shown in Table 6.1, the molecular weights of those graft copolymers increased significantly compared with the starting PPE-OH.

Figure 6.10 illustrates how the adhesion between PPE and PMMA could be promoted by coating various types of functional PPEs in between. The adhesion between non-modified PPE and PMMA was almost zero as expected. Due to the immiscibility of these two polymers, there is very limited amount of entanglement achieved between them leading to very weak adhesion. Nonetheless, when PPE-MA, PPE-OH and PPE-NHR were coated and lied at the interface, adhesion between PPE and PMMA increased significantly to around 400 N/m. PPE-NHR, again, gave the best improvement among the three functional groups suggesting the best reactivity. It is remarkable that he PPE-*g*-

PMMA copolymer generated at least 700 N/m peel strength between PPE and PMMA in contrast with other functional PPEs.

Due to of the immiscibility between polyolefin and PMMA and the high viscosity of PMMA-1, PPE/PMMA-1 blend had number average particle size above 18 μm in Figure 6.11 (a). Nevertheless, when PPE-*g*-PMMA was blended into PPE/PMMA-1, the particle size dropped significantly as shown in Figure 6.11 (b). We attribute the particle size reduction of the dispersed phase to the stabilization of blend morphology by the PPE-*g*-PMMA copolymer at the interface during melt blending. The graft copolymer is expected to stabilize the small particle size by reducing the interfacial tension and thus giving rise to reduced coalescence rate. Morphological studies indicate polyolefin and PMMA to form a heterogeneous blend system with little or no adhesion between the phases. Addition of PMMA grafted polyolefin leads to a significant reduction in size of the dispersed domains along with narrowing down of the domain size distribution.

6.5 CONCLUSION

Compatibility of a polyolefin, PPE and three functional PPEs with PMMA is ranked in a decreasing order as follows: PPE-NHR > PPE-OH > PPE-MA > PPE. This ranking was proved consistently by using mechanical (nano-indentation, nano-scratch and tensile tests), rheological (dynamic temperature ramp), morphological (scanning electron microscopy with image analysis, particle size analysis) and adhesion tests. Secondary amine gave the best improvement suggestive of highest reactivity with ester group on PMMA. Although polyolefin and PMMA are conventionally highly incompatible, we improved compatibility and adhesion between them drastically by blending a synthesized PMMA grated PPE copolymer and reactive compatibilization.

Chapter 7
Adhesion between Polyethylene with Different Types of Polypropylenes

7.1 OVERVIEW

An investigation was performed to measure and understand the interfacial adhesion of a polyethylene to various polypropylenes. Adhesion levels were quantified for the same polyolefin pairs using bilayer coextrusion and lamination processes. We tested adhesion between a medium density polyethylene (MDPE) with different types of polypropylenes (PP), including impact modified PP (with various amount of ethylene), isotactic PP and ethylene-propylene random copolymers. The study aimed to examine the effect of polypropylene copolymer type, random versus impact modified, concentration of ethylene and concentration of ethylene-propylene rubber (EPR), and also cooling rates on bond strength.

Both material composition and processing parameters determine the interfacial adhesion strength. Increasing the concentration of ethylene or EPR gave rise to increased adhesion. The impact modified PP with 20% E content exhibit almost two orders of magnitude higher adhesion with MDPE compared with other PPs we used. In terms of processes, while lamination and coextrusion processes showed excellent agreement, the operation parameters are critical for adhesion control. In particular, we found that for all the laminated polymer pairs, ice water cooling generated stronger adhesion compared to that with air cooling. Faster cooling rates in coextrusion also gave rise to stronger adhesion and more roughened interface. By simply increasing the take up speed of chill rollers we increased interface adhesion strength at least by a factor of 2. Increased crystallinity induced by drawing down of chill rollers is believed to cause the stronger adhesion.

This research attempted to correlate bond strength with interface structure through AFM and TEM characterization. Both AFM and TEM characterization proved to be

valuable techniques to reveal the interfacial structure and morphologies of the polyolefins near the interface. AFM and TEM images exhibit roughened interfaces for samples with stronger adhesion.

7.2 INTRODUCTION

Polyethylene (PE) and isotactic polypropylene (iPP) are the first and second highest volume thermoplastics based on worldwide consumption.[143] The advent of catalysis chemistry, new applications, and an expanded user base are projected to fuel the growth of these polyolefins. PE and iPP are low-cost materials providing good mechanical properties for moderate temperature applications.

Melt blending is frequently used to extend the property range of polymers. It is also an attractive approach for recycling mixed polymer waste streams. Despite the fact that PP and PE are simple chemical isomers, these two polymers are thermodynamically immiscible. The incompatibility of PP and PE results in blends that have extremely low fracture strain and poor toughness. For instance, when PP and PE blends are cooled from molten state, each phase "solidifies by chain-folding into extended crystalline lamellae sandwiched between amorphous regions composed of disorganized looping sections of polymer".[144] In order to improve the compatibility of these two polymers, compatibilizers are usually required. To be effective, the compatibilizer needs to concentrate at the interface where it can reduce interfacial tension and improve adhesion.

Interfacial adhesion is not easily examined in the dispersed domain morphology of conventional melt blends. An alternative approach takes advantage of coextrusion to fabricate a one-dimensional model of the melt blend. While there is a considerable body of literature on the use of interfacial coupling reactions to form covalent bonding between different phases leading to increased adhesion, there has been very little study of the adhesion between polyolefins without any chemical reactions occurring at the interface. The mechanism of adhesion at semicrystalline polyolefin interfaces and relevant parameters that affect adhesion will be studied in this chapter. The adhesion between medium density polyethylene (MDPE) with different types of polypropylenes (PPs),

including impact modified PP (with various amount of ethylene), isotactic PP and ethylene-propylene random copolymers will be tested. We aim to examine the effect of polypropylene copolymer type, random versus impact modified, concentration of ethylene and concentration of ethylene-propylene rubber (EPR), and also processing variables on bond strength.

7.3 EXPERIMENTAL

7.3.1 Materials

Linear medium density polyethylene (MDPE) was provided by The Dow Chemical Company with trade name DHDA-8864 NT. This polymer has a density of 0.932 g/cm^3, melt index of 0.65g/10 min. The propylene/ ethylene random copolymer, referred as PPE in this study, was provided by INEOS with trade name R12C-00. This polymer has a melt flow rate of 12 g/ 10 min (2.16 kg at 230 ℃). The isotactic polypropylene, referred as iPP in this study, was provided by INEOS with trade name H03G-00. This polymer has a melt flow rate of 3.5 g/ 10 min (2.16 kg at 230 ℃).

Impact modified polypropylene, PP (20%), with a trade name of INEOS T10G-02 has a MFR of 10 g/ 10 min (2.16 kg at 230 ℃). Impact modified polypropylene, PP (9%), with a trade name of INEOS N05U-00 has a MFR of 5 g/ 10 min (2.16 kg at 230 ℃). The molecular characteristics of polyolefins are summarized in Table 1. In the PP (20%), there is about 50% of the total polymer that is EPR. PP (20%) contains ethylene monomers. About 50% of the entire ethylene monomers exist in EPR and the other half in polymer matrix. In the PP (9 %), there is about 20% of the total polymer that is EPR. Ethylene and EPR concentration in Table 7.1 represent the percentage of ethylene segments and EPR in total in the entire polymer respectively.

Differential scanning calorimetry (DSC) measurements were performed with TA Instruments DSC Q1000. Approximately 10 mg of dry polymers were loaded into non-hermetic aluminum pans. DSC scans were performed at the rate of 10 ^{o}C/min from -100 to 250 ^{o}C. Melting temperature was determined from the second scanning cycle using TA Instruments Universal Analysis 2000 software.

Table 7.1 Molecular characteristics of polyolefins used.

	Ethylene concentration (wt %)	Propylene concentration (wt %)	EPR concentration (wt %)	Melting Point (℃)	Heat of Fusion (J/g)
iPP	0	100	0	162.8	67.9
PPE	3.4	96.6	0	148.8	58.7
PP (9%)	9.1	90.9	20.0	167.4	72.4
PP (20%)	19.9	80.1	52.0	146.3	20.5
MDPE	100	0	0	123.4	102.5
HDPE	100	0	0	125.0	

7.3.2 Lamination

All the polyolefin films (80mm×7.5mm×0.4mm) were prepared by compression molding from pellets at 210 ℃ under 2 MPa between two polytetrafluoroethylene (PTFE) coated aluminum foils (Saint-Gobain Performance Plastics). All the polyolefin films were dried in vacuum oven at room temperature overnight. After drying under vacuum, MDPE was pressed into intimate contact with various PP films then sandwiched between two PTFE coated aluminum foils and annealed for various times at 210 ℃ under 0.1 MPa within a rectangular mold (80mm×7.5mm×0.75mm).

Immediately after annealing, these bilayer samples were quenched by plunging into ice water or left in the air at room temperature. The edges of bilayer samples were trimmed with a razor blade and adhesion tests were conducted 24 hours after lamination. ADCB tests were applied to test interfacial adhesion as described in Chapter 4.

7.3.3 Coextrusion

Bilayer samples of MDPE with different PPs were prepared by coextrusion at 210 ℃ through the dies depicted in Figure 3.2. Gear pumps (Zenith PEP-II) were used to

control the flow rate to the feedblock. The MDPE and different PPs were extruded at equal flow and also unbalanced flow rates by varying the speed of the gear pumps. A detailed description of the coextrusion line can be found in the literature.[18,39,52,53] Based on the continuity equation, melt velocity in the coextrusion dies can be deduced from the chill roll speed and film thickness. At a total flow rate of 38.4 cm^3/min as determined from gear pump rotation rate, the average linear velocity of the polymer melt in the die land was about 10 mm/sec. Thus, the residence time in the sheeting die and die land was less than 10 sec. Upon exiting the die land, bilayer films were drawn by stainless steel rolls chilled at 4 ℃. The temperature of molten polymer was measured by an infrared pyrometer (Omega Engineering, Inc.). The die exit has dimension of 50 mm×1.2 mm. The thickness of bilayer samples varied from 0.4 mm to 1 mm depending on take-up velocities of the chill rolls. ADCB tests on coextruded films were conducted by using the same procedure as described in Chapter 4.

7.3.4 Characterization

Atomic force microscopy (AFM)

The cryo-microtomed cross-sections of coextruded bilayers were examined using AFM with a Nanoscope III Multimode system (Digital Instruments) in tapping mode within the repulsive regime. All the data were acquired in height and phase mode with scan rate of 1 Hz.

Transmission electron microscopy (TEM)

A JEOL 1200 EXII transmission electron microscope was used to study the interface and also morphologies near the interface of the cryo-microtomed cross-section of coextruded bilayers. An accelerating voltage of 120 kV was used. A side mounted, SIS MegaView III high resolution CCD camera and a Gatan 651N liquid nitrogen anti-contaminator were used.

7.4 RESULTS AND DISCUSSION

7.4.1 Lamination

The isotactic polypropylene (iPP), propylene ethylene random copolymer (PPE), impact modified PP with 9% and 20% of ethylene, i.e., PP (9%) and PP (20%) were laminatated with medium density polyethylene (MDPE) and high density polyethylene (HDPE) by hot pressing. The adhesion strength between MDPE with various PPs was examined with two different cooling rates, air cooling (~5 ℃/s) vs. ice water cooling (~50 ℃/s). Figure 7.1 and 7.2 show: (1) for all the polymer pairs, ice water cooling generated stronger adhesion compared to that with air cooling; (2)PP (20%) gave rise to two orders of magnitude higher adhesion than the rest of the other PP materials. We examine these two findings in the following paragraphs.

Narasimhan et al.[145] conducted elegant experiments to determine how temperature change will affect the interfacial width between immiscible polymers. They found that when iPP and PE were annealed at 160 ℃, the equilibrium interfacial width was approximately 28 nm. When the annealing temperature was changed to140 ℃, the equilibrium interfacial width decreased to 11 nm. If the laminates were annealed at 160 ℃, then quenched to140 ℃, the interfacial width was approximately 21 nm, between the values observed in the two previous experiments.

The ethylene–propylene segmental interaction parameter χ follows an inverse dependence on temperature [145]

$$\chi = A + \frac{B}{T} \qquad \text{(Equation 7.1)}$$

where A is a negative constant and B is a positive constant. Apparently lower temperature leads to larger χ indicating poor compatibility. From Narasimhan's findings and the dependence χ of on temperature, we can tell that although lower annealing temperature generates thinner interface due to bigger χ, quenching can help to retain the entangled structure from high temperature, where the polymer pairs are more compatible due to smaller χ at high temperature. Interfacial entanglements established in the molten state are anchored in chain-folded lamellae upon quenching. Therefore, faster cooling rate

facilitates preservation of the entanglement structure created at high temperature. In contrast, slower cooling helps the interface to reach equilibrium state at low temperature with less entanglement and thinner interface.

Regarding the dramatic adhesion improvement by using PP (20%), we propose that interfacial adhesion is dominated by compatibility. Increasing the concentration of ethylene raises the compatibility of PP (20%) with MDPE and HDPE. Zhu et al. [146] also observed that increasing the ethylene content of an ethylene propylene copolymer at the PE/iPP interface enhanced the mechanical property of the blends indicating stronger interfacial bonding. Therefore the co-crystallization of the ethylene segments in ethylene-propylene copolymer component of PP (20%) and the PE chain in HDPE was proposed to explain the high strength welding. It could be more entanglement although it is difficult to differentiate co-crystallization or entanglement with the current data. It should be noted that MDPE showed stronger adhesion with each one of the PPs compared to HDPE. We attribute this to the better compatibility of MDPE with PPs since HDPE and iPP are highly immiscible.

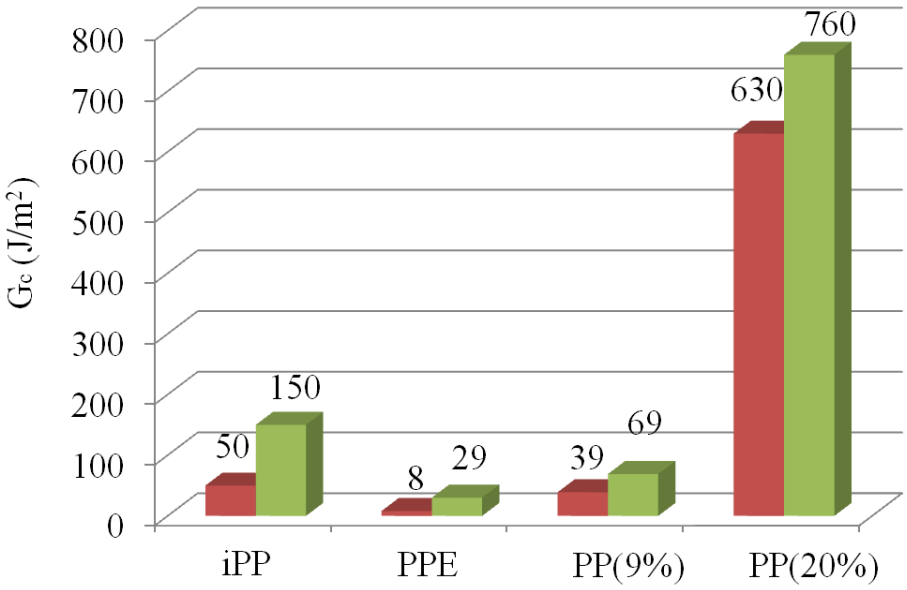

Figure 7.1 Adhesion between MDPE with various PPs under different cooling conditions. For each PP, the left column represents air cooling; the right column represents ice water cooling.

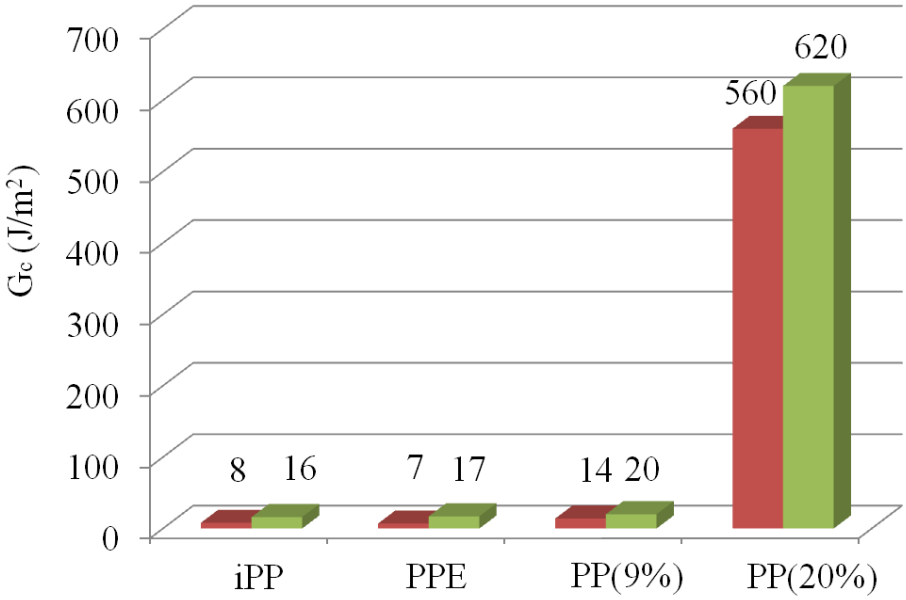

Figure 7.2 Adhesion between HDPE with various PPs under different cooling conditions. For each PP, the left column represents air cooling; the right column represents ice water cooling.

Table 7.2 Adhesion strength of coextruded bilayers with different processing variables.

Sample	Material 1	Material 2	Q1/Q2	Q_{total} (cm^3/min)	Take up speed (cm/min)	Adhesion strength (N/m)
1	MDPE	iPP	1/1	33.6	64.7	55 ±12
2	MDPE	iPP	1/1	33.6	108.3	77 ±21
3	MDPE	iPP	1/1	33.6	146.4	251 ±67
4	MDPE	iPP	1/6.25	34.8	64.7	588 ±108
5	MDPE	PPE	6.25/1	34.8	64.7	279 ±47
6	MDPE	PPE	6.25/1	34.8	108.3	187 ±39
7	MDPE	PPE	6.25/1	34.8	146.4	152 ±45
8	MDPE	PPE	6.25/1	34.8	185.2	120 ±25
9	MDPE	PPE	1/1	33.6	64.7	79 ±21
10	MDPE	PPE	1/1	33.6	108.3	62 ±16
11	MDPE	PPE	1/1	33.6	146.4	54 ±14
12	MDPE	PPE	1/1	33.6	185.2	42 ±12
13	MDPE	PP (9%)	12.5/1	32.4	64.7	224 ±38
14	MDPE	PP (9%)	12.5/1	32.4	108.3	294 ±58
15	MDPE	PP (9%)	12.5/1	32.4	146.4	485 ±75
16	MDPE	PP (20%)	1/1	33.6	64.7	1437 ±308
17	MDPE	PP (20%)	1/1	33.6	108.3	1976 ±462
18	MDPE	PP (20%)	1/1	33.6	146.4	2310 ±508
19	MDPE	PP (20%)	6.25/1	34.8	64.7	1524 ±377
20	MDPE	PP (20%)	1/6.25	34.8	64.7	1918 ±515

7.4.2 Coextrusion

The flow rate ratio, total flow rate, take up speed and adhesion strength are summarized in Table 7.2. We intentionally controlled the total flow rate to be almost identical, so that the residence time of the bilayers will not contribute to the change of adhesion. We varied the flow rate ratio to apply different levels of shear stress to the interface for the same pair of materials. When the flow rate of one layer is identical to that of the other layer, i.e., with an equal proportion of PE and PP, the interface between the two materials within the extrusion tooling is located at the center of the flow and thus experiences zero shear stress. However when the ratio between the PP and MDPE thickness is changed, the interface between the two materials within the tooling moves to a region of non-zero shear stress.

We found that for the same polymer pair, unbalanced flow rate exhibit stronger adhesion compared with equal flow rate. For instance, as shown in Table 7.2, coextrusion sample 5-8 generally demonstrated stronger adhesion compared to sample 9-12 while all the other parameters are the same. Similarly sample 4 exhibited stronger adhesion than sample . As discussed above, with unequal flow rates the interface between the two materials within the tooling moves to a region of non-zero shear stress. However, we[147] have shown that shear plays a role of disentangling the interface and lowering the adhesion. Therefore we attribute this adhesion difference to different cooling rates at the interface.

To estimate the cooling rates at the interface when the bilayer went through the nip point of the chill rolls, the unsteady state heat conduction model was used as described by the equation below: [62]

$$\frac{T_b - T}{T_b - T_0} = 2\sum \frac{(-1)^n}{(n+\frac{1}{2})\pi} e^{-(n+\frac{1}{2})^2 \pi^2 \frac{\alpha t}{l^2}} \cos(n+\frac{1}{2})\frac{\pi z}{l_0}$$

(Equation 7.2)

where T_b is temperature of chill roll, T_0 is temperature of the polymer melt at time zero, T is temperature of position z at time t, α is thermal diffusivity, l_0 is half of the gap between the two rolls, and z is distance from the center of the polymer melt to surface. It was

determined that the cooling rate at the interface of sample 5 is almost five times of that of sample 9 due to thickness difference. As shown in the lamination tests, faster cooling generated stronger adhesion between the immiscible polyolefins.

7.4.3 Morphologies near interface and interface characterization

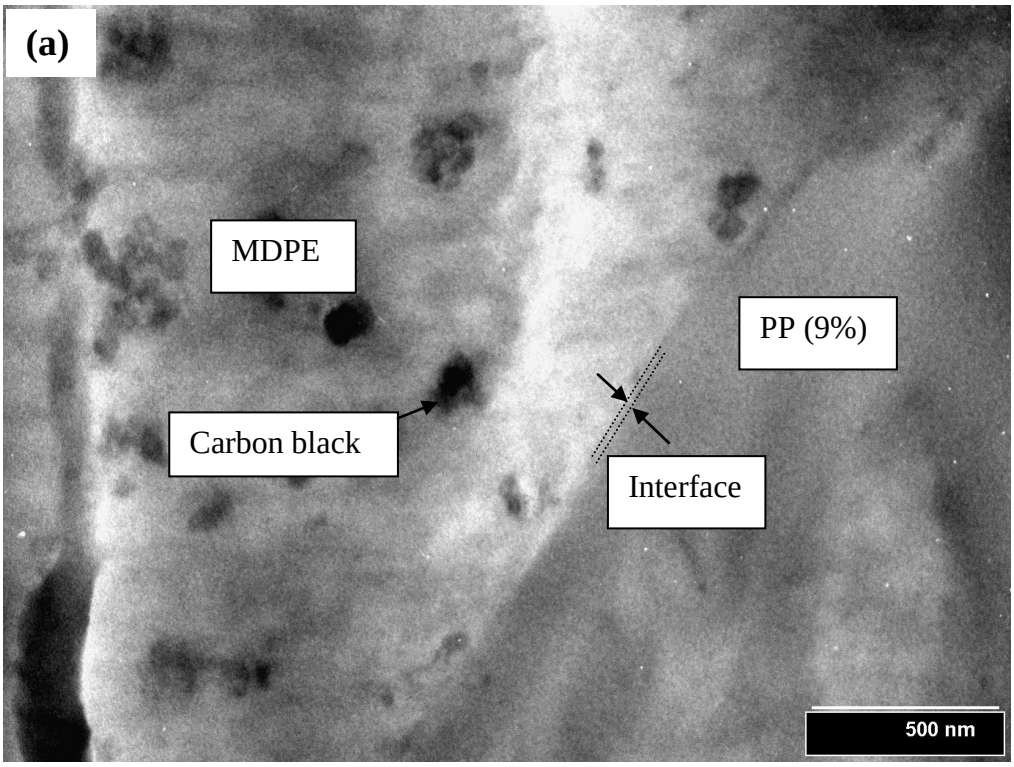

Figure 7.3(a) Interfacial morphology as observed with TEM for coextrusion sample 13. The top left phase is MDPE with carbon black; the bottom right phase is PP (9%).

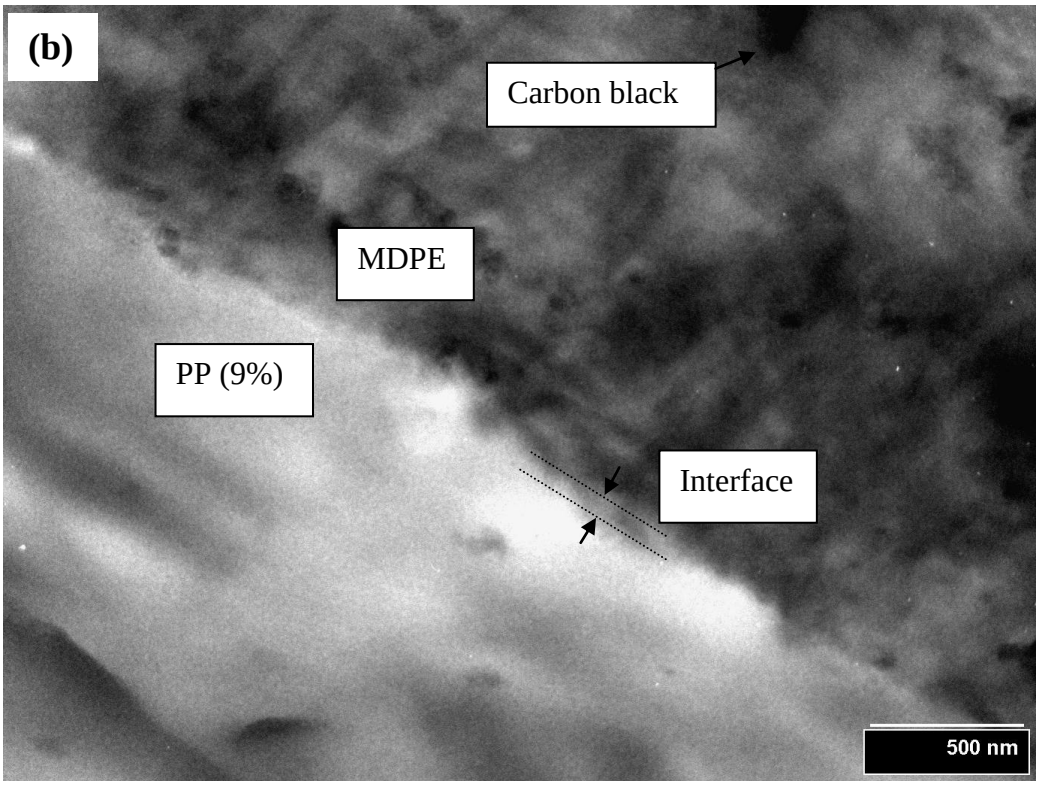

Figure 7.3 (b) Interfacial morphology as observed with TEM for coextrusion sample 15. The top right phase is MDPE with carbon black; the bottom left phase is PP (9%).

χ plays an important role in terms of determining the interfacial width and adhesion.[148] Chaturvedi et al.[149] used mean field theory to propose a χ dependent interfacial width (w) for incompatible polymers:

$$w = \frac{b\sqrt{2}}{3\chi_c^{0.5}}\left(\frac{\chi}{\chi_c} - 1\right)^{-1/2} \qquad \text{(Equation 7.3)}$$

where b is the average segment length and χ_c is the interaction parameter at the critical point. χ_c can be obtained by the equation from Krause et al.:[150]

$$\chi_c = \frac{1}{2}\left[x_1^{0.5} + x_2^{0.5} \right]^2 \qquad \text{(Equation 7.4)}$$

where the x_i is the degree of polymerization of the polymers. For our system, χ_c was determined to be 2×10^{-3}.

The average segment length *b* can be calculated as follows:

$$b = \left(\frac{b_{iPP}^2 + b_{PE}^2}{2} \right)^{1/2} \qquad \text{(Equation 7.5)}$$

The segment lengths of PE and iPP are 2.55 and 6.5 Å, respectively.[151] Therefore, the average segment length *b* was determined to be 4.93 Å. By using the χ value determined by Narasimhan et al.[145] from SAXS data, we were able to calculate the interfacial width.

Table 7.3 compares the interfacial width obtained from TEM with the value calculated with Equation 7.3. Obviously the observed interfacial width, as shown in Figure 7.3, is wider than the calculated one. The observed interfacial width of coextrusion sample 15 is almost twice that of coextrusion sample 13. As discussed previously in the lamination session, the fast quenching induced by higher take up speed helps retain the more compatible structure at high temperature, where the interface should be broader.

Table 7.2 also showed that increasing take up speed leads to stronger interfacial bonding. For instance, from coextrusion sample 1 to 3, adhesion strength increased by almost five times when the take up speed increased. Other polymer pairs also showed similar trend. Note that before the bilayer streams exited the die, the flow conditions were all the same for sample 1 to 3. The difference was upon exiting the die, polymer chains were extended to different degrees. Increasing take up speed resulted in increased crystallinity, as shown in Table 7.4. It is not surprising that increased crystallinity leads to stronger interfacial adhesion, as proved by other researchers as well.[90,94] Faster take up speeds also lead to smaller thickness giving rise to faster cooling rate as Equation 7.2 suggested. Faster cooling rate will also result in stronger adhesion as discussed above.

Table 7.3 Comparison of the interfacial widths obtained from TEM and calculated with Equation 7.1.

Sample	Interfacial width obtained from TEM	Interfacial width calculated from Equation 7.3
13	20.6	10.9
15	48.5	10.9

Table 7.4 The effect of take up speed on adhesion correlated with crystallinity.

Sample	Take up speed (cm/min)	Adhesion strength (N/m)	Crystallinity of iPP (%)
1	64.7	55	33.5
2	108.3	77	40.9
3	146.4	251	43.4

Figure 7.4 gave us more insights to the microstructure of the impact modified PP (9%) polymer. As the AFM tested was conducted in repulsive regime, the dark phase indicates softer region while the brighter one represents harder one. The dark inclusions (soft) with hard inclusions in them, probably crystallizable ethylene propylene rubber (EPR), are classic signature for Zeigler Natta iPP with some EPR in it. We took several AFM images for the same coextrudate and found that there was no EPR from the PP (9%) contacting the MDPE phase, indicating that the impact modifier does not contribute the interfacial adhesion. Figure 7.5 showed that iPP/MDPE has more roughened interface for coextrusion sample 4 compared to sample 1 with a clear, sharp interface. It is not surprising that sample 4 with more roughened interface has much stronger adhesion compared with sample 1 with a sharp interface. There are numerous examples in literature[152,153] showing that strong interfacial adhesion between immiscible polymers

usually comes with roughened interface. Figure 7.6 showed the morphologies of PP (20%) near the interface. For image (a) where the interfacial shear stress was more than zero, the EPR rubbers were distorted and ruptured, whereas for image (b) the interfacial shear stress was zero, the EPR rubber maintained their droplet structure. Both images also displayed that it was mostly the EPR rubber that was contacting the MDPE phase providing the interfacial adhesion, while for PP (9%) as shown earlier in Figure 7.4 almost no EPR rubber was contacting the MDPE phase. Figure 7.1, 7.2 and Table 7.2 show that PP (20%) showed dramatic adhesion improvement with MDPE and HDPE. Therefore EPR rubber showed remarkable compatibility with MDPE and HDPE. Considering that fact that there was more than 50% of ethylene in the EPR phase, clearly the large amount of ethylene gave rise to the much better compatibility with the PE phase hence strong interfacial adhesion.

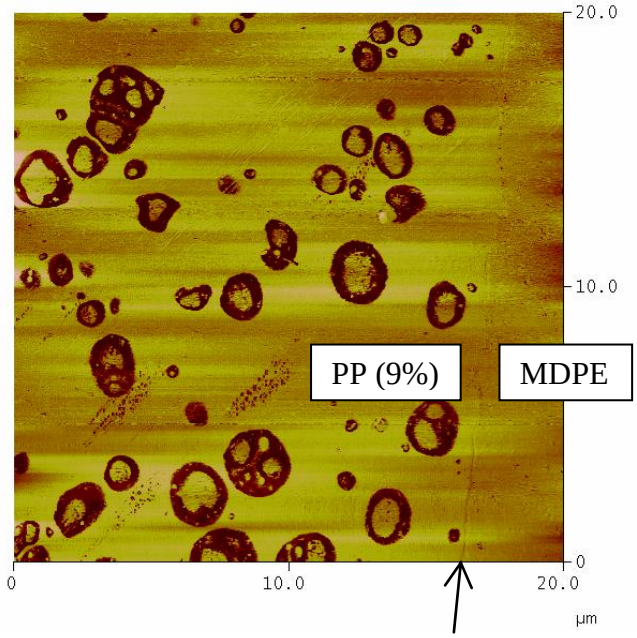

(a)

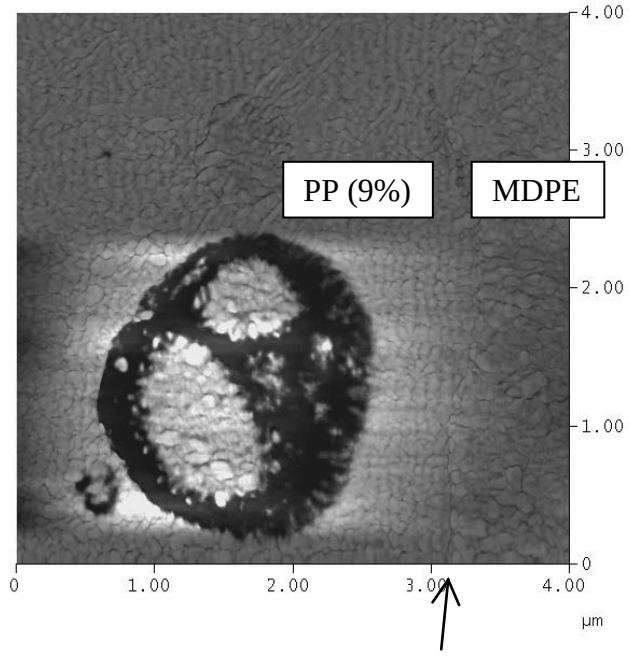

(b)

Figure 7.4 Morphology of cross-section of coextruded bilayers. (a) MDPE vs. PP (9%) with flow rate ratio 1:1 (b) Magnified image of (a). The left phase is PP (9%) and the right is MDPE. The arrows indicate interface.

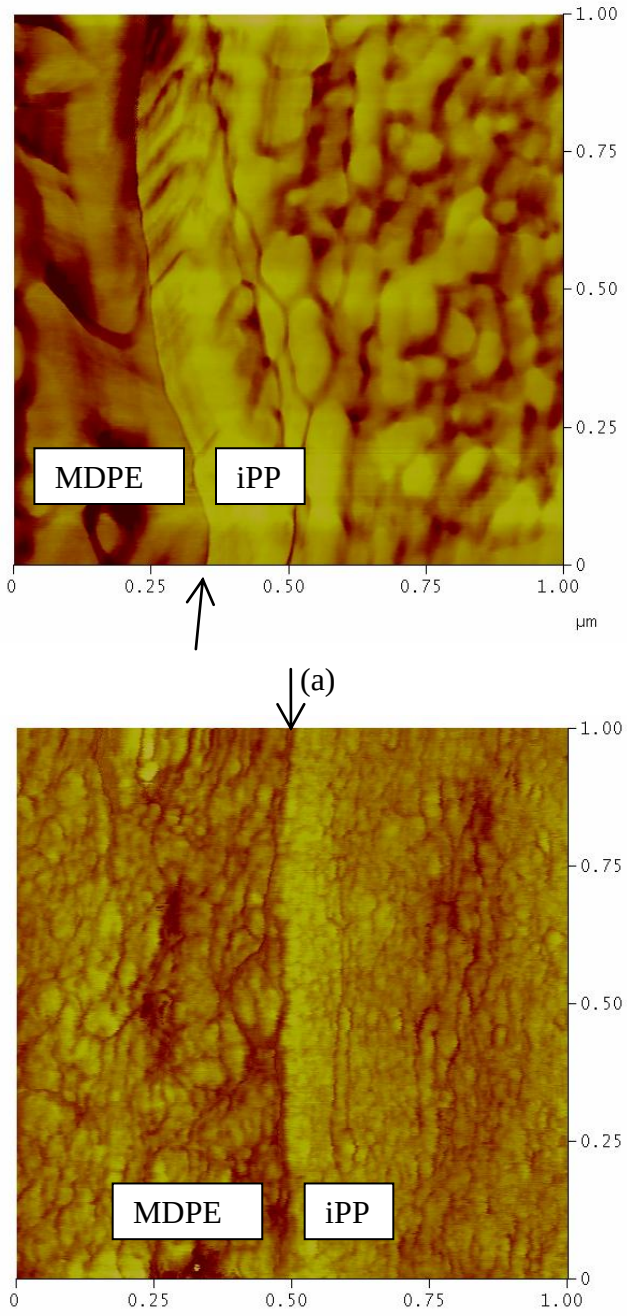

(b)

Figure 7.5 Morphology of cross-section of coextruded bilayers. (a) Coextrusion sample 1 (b) Coextrusion sample 4. For both images, the left side is MDPE and the right is iPP. Faster cooling for sample 4 generated smaller crystalline domains than sample 1. The arrows indicate interface.

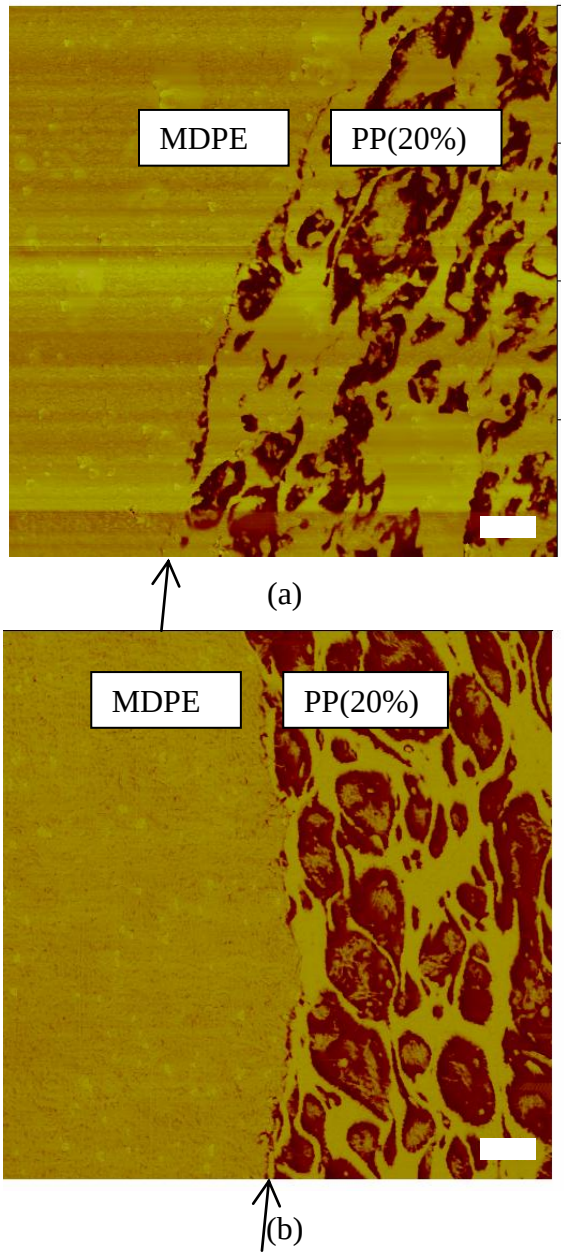

Figure 7.6 Morphology of cross-section of coextruded bilayers. (a) Coextrusion sample 19 (b) Coextrusion sample 16. The left side is MDPE and the right is PP(20%). The scale bar represents 1 μm. The arrows indicate interface.

7.5 CONCLUSIONS

Adhesion between PE and various PP were investigated both through lamination and coextrusion processes; both showed similar results. Cooling rate is critical in terms of determining interfacial adhesion between polyolefins. For all the laminated polymer pairs, ice water cooling generated stronger adhesion compared to that with air cooling. Faster cooling rates in coextrusion also gave rise to stronger adhesion and more roughened interfaces, as verified by utilizing unbalanced flow rates of the bilayers. By simply increasing the take up speed of chill rollers we increased interface adhesion strength at least by a factor of 2. Increased crystallinity induced by drawing down of chill rollers is believed to cause stronger adhesion. Materials composition, specifically percentage of ethylene, determines the compatibility of the PP materials with PE hence interfacial adhesion. Impact modified PP with 20% of ethylene gave rise to almost two orders of magnitude higher adhesion than the rest of the other PP materials. Both AFM and TEM characterization proved to be valuable techniques to reveal the interfacial structure and morphologies of the polyolefins near the interface. AFM and TEM images exhibit roughened interfaces for samples with stronger adhesion.

CHAPTER 8

Recommended Future Work

The area of interfacial coupling reactions is still ripe with opportunities for exciting research. The following list is just some of the areas that would be worthwhile for future research.

(1) Future studies can be designed to test the effect of compressive flow normal to the interface in contrast with compressive/extensional flow in the plane of the interface. This can be accomplished by modifying the current die design (Figure 4.2) in order to decouple these effects. Compressive flow normal to the interface can be generated by changing the height $H(x)$ while keeping width W=constant, in contrast to compression/extension in the plane of the interface caused by varying the width $W(x)$ while keeping height H = constant. Such tests would reveal the dependency of the reaction rate ν on the strength of the compressive flow $\dot{\varepsilon}$, and these results would be a guide to developing a more specific molecular theory to explain the increase in reaction rate observed in this study.

(2) In Chapter 3 and 4, we had to apply gentle pressure on the top of laminated bilayers in order to achieve good contact between the two layers. However, it would be desirable if we could eliminate the force normal to the interface during annealing. This can be accomplished by using spin coating to make thin films of the two polymers and stacking them to anneal. The reaction conversion can be simply measured by following the same procedure as described in Chapter 4.

(3) Our preliminary study has shown that secondary amine gave the largest improvement on compatibility, modulus and hardness enhancement when blended with PMMA. We can further facilitate the reaction between functional polyolefins and PMMA by exploring appropriate catalysts. The nucleophilic acyl substitution of PMMA with

functional polyolefins can be studied in 1,2,4-trichlorobenzene solution and in the melt with addition of catalysts.

(4) The chemistries developed for modification of the ester functionality of PMMA may also be successfully applied to various poly(ethylene-co-acrylate) copolymers as well. These materials are typically prepared on an industrial scale by a radical initiated, high pressure polymerization process. In principle, one could tune the adhesive and hydrophilic properties of this class of polyolefin materials by reactive melt chemistry on the pendant ester functionality, which might broaden the application space for these materials. Also we will explore use of these copolymers as adhesion promoters; they may vector to the interface between polyolefin and polyacrylate in their blends.

Bibliography

(1) Chung, T. C. *Functionalization of Polyolefins* Academic Press, 2000.

(2) E. Albizzati; Galimberti, M. *Catal. Today* **1998**, *41*, 159.

(3) Sha, Y.; Hui, C. Y. *Macromolecules* **1996**, *29*, 4728-4736.

(4) Cole, P. J.; Cook, R. F.; Macosko, C. W. *Macromolecules* **2003**, *36*, 2808-2815.

(5) Zhang, J.; Lodge, T. P.; Macosko, C. W. *Macromolecules* **2005**, *38*, 6586-6591.

(6) J. Duvall; C. Sellitti; C. Myers; Hiltner, A. *J. Appl. Polym. Sci.* **1994**, *52*, 207.

(7) Jeon, H. K.; Macosko, C. W.; Moon, B.; Hoye, T. R.; Yin, Z. *Macromolecules* **2004**, *37*, 2563-2671.

(8) Boaen, N. K.; Hillmyer, M. A. *Chem. Soc. Rev.* **2005**, *34*, 267-275.

(9) Dong, J. Y.; Hu, Y. L. *Coord. Chem. Rev.* **2006**, *250*, 47.

(10) Padwa, A. R. *Prog. Polym. Sci.* **1989**, *14*, 811.

(11) Sun, Y. J.; Hu, G. H.; Lambla, M.; Kotlar, H. K. *Polymer* **1996**, *37*, 4119-4127.

(12) Kim, S. J.; Shin, B. S.; Hong, J. L.; Cho, W. J.; Ha, C. S. *Polymer* **2001**, *42*, 4073-4080.

(13) Kelar, K.; Jurkowski, B. *Polymer* **2000**, *41*, 1055-1062.

(14) Carlson, D.; Nie, L.; Narayan, R.; Dubois, P. *J. Appl. Polym. Sci.* **1999**, *72*, 477-485.

(15) Boaen, N. K.; Hillmyer, M. A. *Macromolecules* **2003**, *36*, 7027-7034.

(16) Creton, C.; Kramer, E. J.; Hui, C.-Y.; Brown, H. R. *Macromolecules* **1992**, *25*, 3075-3088.

(17) Boucher, E.; Folker, J. P.; Creton, C.; Hervet, H.; Leger, L. *Macromolecules* **1997**, *30*, 2102-2109.

(18) Zhang, J.; Ji, S.; Song, J.; Lodge, T. P.; Macosko, C. W. *Macromolecules* **2010**, *43*, 7617-7624.

(19) Brown, H. R. *Annu. Rev. Mater. Sci.* **1991**, *21*, 463.

(20) Brown, H. R. *Macromolecules* **1991**, *24*, 2752-2756.

(21) Brown, H. R. *Mater. Res. Soc. Symp. Proc.* **1992**, *264*, 183.

(22) Benkoski, J. J.; Flores, P.; Kramer, E. J. *Macromolecules* **2003**, *36*, 3289.

(23) Creton, C.; Kramer, E. J.; Hui, C. Y.; Brown, H. R. *Macromolecules* **1992**, *25*, 3075-3088.

(24) Norton, L. J.; Smigolova, V.; Pralle, M. U.; Hubenko, A.; Dai, K. H.; Kramer, E. J.; Hahn, S. F.; Berglund, C.; DeKoven, B. *Macromolecules* **1995**, *28*, 1999.

(25) Zhang, J.; Cole, P. J.; Nagpal, U.; Lodge, T. P.; Macosko, C. W. *J. Adhesion* **2006**, *82*, 887.

(26) Zhang, J.; Lodge, T. P.; Macosko, C. W. *Macromolecules* **2005**, *38*, 6583.

(27) Oyama, H. T.; Ougizawa, T.; Inoue, T.; Weber, M.; Tamaru, K. *Macromolecules* **2001**, *34*, 7017.

(28) Oyama, H. T.; Ougizawa, T. *Macromolecules* **2001**, *34*, 7017-7024.

(29) Oyama, H. T.; Inoue, T. *Macromolecules* **2001**, *34*, 3331-3338.

(30) Kramer, E. J.; Berger, L. L. *Adv. Polym. Sci.* **1990**, *91*, 1.

(31) Benkoski, J. J.; Fredrickson, G. H.; Kramer, E. J. *J. Polym. Sci., Part B: Polym. Phys.* **2001**, *39*, 2363.

(32) H. Kim; K. Lee; Seo, Y. *Macromolecules* **2002**, *35*, 1267.

(33) Orr, C. A.; Cernohous, J. J.; Guegan, P.; Hirao, A.; Jeon, H. K.; Macosko, C. W. *Polymer* **2001**, *42*, 8171-8178.

(34) Macosko, C. W.; Jeon, H. K.; Hoye, T. R. *Prog. Polym. Sci.* **2005**, *30*, 939-947.

(35) Schulze, J. S.; Cernohous, J. J.; Hirao, A.; Lodge, T. P.; Macosko, C. W. *Macromolecules* **2000**, *33*, 1191.

(36) Lee, P.; Macosko, C. W. In *Soc. Plast. Eng. Annu. Tech Conf.* Chicago, IL, 2009.

(37) Lee, P.; Park, H. E.; Morse, D. C.; Macosko, C. W. *J. Rheol.* **2009**, *53*, 893.

(38) Park, H. E.; Lee, P. C.; Macosko, C. W. *J. Rheol.* **2010**, *54*, 1207-1218.

(39) Zhao, R.; Macosko, C. W. *J. Rheol.* **2002**, *46*, 145-167.

(40) Moad, G. *Prog. Polym. Sci.* **1999**, *24*, 81-142.

(41) Wang, X. C.; Tzoganakis, C.; Rempel, G. L. *J. Appl. Polym. Sci.* **1996**, *61*, 1395-1404.

(42) Silvis, C. H.; Hahn, S. F.; Pawlowski, D. F.; Ansems, P.; Mergenhagen, L. K.; Lakrout, H. 2008/080081.

(43) Lu, Q.; Macosko, C. W.; Horrion, J. *J. Polym. Sci.: Part A: Polym. Chem.* **2005**, *43*, 4217-4232.

(44) Jackson, C.; Chen, Y. J.; Mays, J. W. *J. Appl. Polym. Sci.* **1996**, *61*, 865-874.

(45) Kobayashi, S.; Song, J.; Silvis, H. C.; Macosko, C. W.; Hillmyer, M. A. *Ind. Eng. Chem. Res.* **2011**, *50*, 3274-3279.

(46) Kaiser, E.; Colescott, R. L.; Bossinger, C. D.; Cook, P. I. *Anal. Biochem.* **1970**, *34*, 595-598.

(47) Lee, I.; Wool, R. P. *Macromolecules* **2000**, *33*, 2680.

(48) Lu, Q.; Hoye, T. R.; Macosko, C. W. *J. Polym. Sci.: Part A: Polym. Chem.* **2002**, *40*, 2310-2328.

(49) Ghasemi, M.; Minier, M.; Tatoulian, M.; Arefi-Khonsari, F. *Langmuir* **2007**, *23*, 11554-11561.

(50) Lu, Q.; Macosko, C. W. *Polym. Mater. Sci. Eng.* **2003**, *89*, 844-847.

(51) Spitael, P.; Macosko, C. W. *Polym. Engn. Sci.* **2004**, *44*, 2090-2100.

(52) Lee, P. C.; Park, H. E.; Morse, D. C.; Macosko, C. W. *J. Rheol.* **2009**, *53*, 893-915.

(53) Dolgovskij, M., Ph. D. Thesis, University of Minnesota, 2007.

(54) Kinloch, A. J.; Lau, C. C.; Williams, J. G. *Inter. J. of Frac.* **1994**, *66*, 45-70.

(55) Kinloch, A. J. *Proc. Instn. Mech. Engrs.* **1997**, *211*, 307-335.

(56) Georgiou, I.; Hadavinia, H.; Ivankovic, A.; Kinloch, A. J.; Tropsa, V.; Williams, J. G. *J. Adhesion* **2003**, *79*, 239-265.

(57) Dai, C.; Kramer, E. J.; Washiyama, J.; Hui, C. *Macromolecules* **1996**, *29*, 7536-7543.

(58) Wei, Y.; Hutchinson, J. W. *Intl. J. Frac.* **1998**, *93*, 315-333.

(59) Hadavinia, H.; Kawashita, L.; Kinloch, A. J.; Moore, D. R.; Williams, J. G. *Engn. Fract. Mech.* **2006**, *73*, 2324-2335.

(60) Fredrickson, G. H.; Milner, S. T. *Macromolecules* **1996**, *29*, 7386-7390.

(61) Morris, B. A. *J. Plast. Film Sheeting* **2008**, *24*, 53-88.

(62) Bird, R. B.; Stewart, W. E.; Lightfoot, E. N. *Transport Phenomena*; John Wiley & Sons, 2007.

(63) Morris, B. A. *SPE-ANTEC Tech. Papers* **1996**, 116-120.

(64) Macosko, C. W. *Rheology-Principles, Measurements, and Applications*; Wiley: New York, 1994.

(65) Seo, Y.; Ninh, T. H. *Polymer* **2004**, *45*, 8573-8581.

(66) Seo, Y.; Kang, T. *Compos. Interface* **2006**, *13*, 605-621.

(67) Zheng, X.; Rafailovich, M. H.; Sokolov, J.; Strzhemechny, Y.; Schwarz, S. A.; Sauer, B.; Rubinstein, M. *Phys. Rev. Lett.* **1997**, *79*, 241-244.

(68) O'Shaughnessy, B.; Vavylonis, D. *Macromolecules* **1999**, *32*, 1785-1796.

(69) Schulze, J. S.; Cernohous, J. J.; Hirao, A.; Lodge, T. P.; Macosko, C. W. *Macromolecules* **2000**, *33*, 1191-1198.

(70) Welp, K. A.; Wool, R. P.; Agrawal, G.; Satija, K.; Pispas, S.; Mays, J. *Macromolecules* **1999**, *32*, 5127-5138.

(71) Panajotova, B. V.; Herman, M. F. *J. Chem. Phys.* **1998**, *108*, 5122-5129.

(72) Anturkar, N. R.; Wilkes, J. O.; Papanastasiou, T. C. *Polym. Engn. Sci.* **1993**, *33*, 1532.

(73) Matos, M.; Favis, B. D.; Lomellini, P. *Polymer* **1995**, *36*, 3899.

(74) Bartels, C. R.; Crist, B.; Graessley, W. W. *Macromolecules* **1984**, *17*, 2702-2708.

(75) Mori, M.; Uyama, Y.; Ikada, Y. *J. Polym. Sci.: Part A: Polym. Chem.* **1994**, *32*, 1683-1690.

(76) Liston, E. M.; Martinu, L.; Wertheimer, M. R. *J. Adhes. Sci. Technol.* **1993**, *7*, 1091-1127

(77) Goddard, J. M.; Hotchkiss, J. H. *J. Appl. Polym. Sci.* **2008**, *108*, 2940-2949.

(78) Jia, S.; Xu, D.; Mai, B.; Zhang, M.; Rong, M. *J. Appl. Polym. Sci.* **2007**, *105*, 1309-1315.

(79) De Gennes, P. G. *J. Chem. Phys.* **1982**, *76*, 3316-3321.

(80) Noolandi, J.; Hong, K. M. *Macromolecules* **1982**, *15*, 482.

(81) Sundararaj, U.; Macosko, C. W. *Macromolecules* **1995**, *28*, 2647.

(82) Feng, L.; Hu, G. *AIChE J.* **2004**, *50*, 2604-2612.

(83) Song, J.; Ewoldt, R. H.; Hu, W.; Silvis, C. H.; Macosko, C. W. *AIChE J.* **2011**, In Press.

(84) Kim, H. Y.; Jeong, U.; Kim, J. K. *Macromolecules* **2003**, *36*, 1594.

(85) Kim, H. Y.; Joo, W.; Kim, J. K. *Macromol. Chem. Phys.* **2008**, *209*, 746.

(86) Kim, H. Y.; Joo, W.; Kim, J. K. *Polymer J.* **2008**, *38*, 1165.

(87) Kim, H. Y.; Lee, D. H.; Kim, J. K. *Polymer* **2006**, *47*, 5108.

(88) Yang, I. K.; Lin, J. D. *Polym. Eng. Sci,* **2002**, *42*, 753-759.

(89) Kanninen, M. F. *Intl. J. Frac.* **1973**, *9*, 83-92.

(90) Boucher, E.; Folkers, J. P.; Hervet, H.; Leger, L.; Creton, C. *Macromolecules* **1996**, *29*, 774-782.

(91) Wagner, C. D.; Davis, L. E.; Zeller, M. W.; Taylor, J. A.; Raymond, R. H.; Gale, L. H. *Surf. Interface Anal.* **1981**, *3*, 211.

(92) Plummer, C. J. G.; Kausch, H. H.; Creton, C.; Kalb, F.; Leger, L. *Macromolecules* **1998**, *31*, 6164-6176.

(93) Jang, B. Z. U., D. R.; Vander Sande, J. B. *Polym. Eng. Sci.* **1985**, *25*, 98-104.

(94) Boucher, E.; Folkers, J. P.; Creton, C.; Hervet, H.; Leger, L. *Macromolecules* **1997**, *30*, 2102-2109.

(95) Sha, Y.; Hui, C. Y.; Ruina, A.; Kramer, E. J. *Macromolecules* **1995**, *28*, 2450-2459.

(96) Larson, R. G.; Magda, J. J. *Macromolecules* **1989**, *22*, 3004-3010.

(97) Perkins, T. T.; Smith, D. E.; Chu, S. *Science* **1997**, *276*, 2016-2021.

(98) Smith, D. E.; Chu, S. *Science* **1998**, *281*, 1335-1340.

(99) Smith, D. E.; Babcock, H. P.; Chu, S. *Science* **1999**, *283*, 1724-1727.

(100) Huang, Z.; Boulatov, R. *Chemical Society Reviews*, *40*, 2359-2384.

(101) Kucharski, T. J.; Boulatov, R. *J. Mater. Chem.* **2011**, *21*, 8237-8255.

(102) Hashidzume, A.; Kawaguchi, A.; Tagawa, A.; Hyoda, K.; Sato, T. *Macromolecules* **2006**, *39*, 1135-1143.

(103) Khalatur, P. G.; Khokhlov, A. R.; Nyrkova, I. A.; Semenov, A. N. *Macromol. Theo. Simul.* **1996**, *5*, 713-747.

(104) Sintes, T.; Toral, R.; Chakrabarti, A. *Phys. Rev. E* **1994**, *50*, 2967-2976.

(105) Burnett, D. J.; Thielmann, F.; Ryntz, R. A. *J. Coat. Technol. Res.* **2007**, *4*, 211-215.

(106) Deng, K. Q.; Felorzabihi, N.; Winnik, M. A.; Jiang, Z.; Yin, Z.; Liu, Y.; Yaneff, P. V.; Ryntz, R. A. *Polymer* **2009**, *50*, 5084-5093.

(107) Liston, E. M.; Martinu, L.; Wertheimer, M. R. *J. Adhesion Sci. Technol.* **1993**, *7*, 1091.

(108) Tomasetti, E.; Daoust, D.; Legras, R.; Bertrand, P.; Rouxhet, P. *J. Adhesion Sci. Technol.* **2001**, *15*, 1589.

(109) Deng, K.; Winnik, M. A.; Yan, N.; Jiang, Z.; Yaneff, P. V.; Ryntz, R. A. *Polymer* **2009**, *50*, 3225-3233.

(110) Mirabella, F. M.; Dioh, N. *Polym. Eng. Sci.* **2000**, *40*, 2000-2006.

(111) Pogany, A.; Gao, D.; Wilkins, S. W. *Rev. Sci. Instrum.* **1997**, *68*, 2774.

(112) Wilhein, T.; Kaulich, B.; Di Fabrizio, E.; Romanato, F.; Cabrini, S.; Susini, J. *Appl. Phys. Lett.* **2001**, *78*, 2082.

(113) Kaulich, B.; Wilhein, T.; Di Fabrizio, E.; Romanato, F.; Altissimo, M.; Cabrini, S.; Fayard, B.; Susini, J. *J. Opt. Soc. Am.* **2002**, *19*, 797.

(114) Ryntz, R. A.; Xie, Q.; Ramamurthy, A. C. *J. Coat. Technol.* **195**, *67*, 35.

(115) Papirer, E.; Wu, D. Y.; Schultz, J. *J. Adhesion Sci. Technol.* **1993**, *7*, 343.

(116) Friedrich, J. F.; Geng, S.; Unger, W.; Lippitz, A.; Erdmann, J.; Gorsler, H.-V.; Wöll, C.; Schertel, A.; Bierbaum, K. *Surf. Coating Technol.* **1995**, *74*, 664-669.

(117) Ryntz, R. A. *Prog. Org. Coat.* **1994**, *25*, 73.

(118) Sharpe, L. H. *J. Adhesion* **1998**, *67*, 277.

(119) Wang, T.-L.; Huang, F.-J. *Macromol. Rapid Commun.* **1999**, *20*, 497-504.

(120) Yoon, S. C.; Ratner, B. D. *Macromolecules* **1986**, *19*, 1068.

(121) S.C. Yoon; B.D. Ratner *Macromolecules* **1988**, *21*, 2392.

(122) Nakamae, K.; Nishino, T.; Asaoka, S. *Int. J. Adhes. Adhes.* **1996**, *16*, 233.

(123) Trent, J. S.; Scheinbeim, J. I.; Couchman, P. R. *Macromolecules* **1983**, *16*, 589.

(124) Kimura, F.; Umemura, J.; Takenaka, T. *Languir* **1986**, *2*, 96-101.

(125) Elwell, M. J.; Ryan, A. J.; Grunbauer, H. J. M.; Van Lieshout, H. C. *Macromolecules* **1996**, *29*, 2960.

(126) Luo, N.; Wang, D. N.; Ying, S. K. *Macromolecules* **1997**, *30*, 4405.

(127) Yilgor, E.; Yilgor, I.; Yurtsever, E. *Polymer* **2002**, *43*, 6551.

(128) **Zhong, G. J.**; **Li, Z. M.** *Polym. Eng. Sci.* **2005**, *42*, 1655.

(129) Karger-Kocsis, J.; Csikai, I. *Polym. Eng. Sci.* **1987**, *27*, 241.

(130) B. Nysten; A. Ghanem; J. Costa; R. Legras *Polym. Int.* **1999**, *48*, 334.

(131) Batra, A.; Weaver, L.; Madenjian, L.; Lakrout, H.; Rego, J. M. *ANTEC* **2009**, 1012.

(132) McCafferty, E.; Wightman, J. P. *Surf. Interface Anal.* **1998**, *26*, 549-564

(133) Schneider, Y.; Azoulay, J. D.; Coffin, R. C.; Bazan, G. C. *J. A. C. S.* **2008**, *108*, 10464–10465.

(134) Inoue, Y.; Matsugi, T.; Kashiwa, N.; Matyjaszewski, K. *Macromolecules* **2004**, *37*, 3651 3658.

(135) Kaneyoshi, H.; Inoue, Y.; Matyjaszewski, K. *Macromolecules* **2005**, *38*, 5425-5435.

(136) Kaneko, H.; Kojoh, S.-I.; Kawahara, N.; Matsuo, S.; Matsugi, T.; Kashiwa, N. *J. Polym. Sci. Part A* **2005**, *43*, 5103-5118.

(137) Harrats, C. B., T.; Groeninckx, G.; Jerome, R. *J. Polym. Sci. Part B* **2005**, *43*, 22-34.

(138) Yoshihara, S.; Maekawa, K.; Uno, M.; Kuraray Co., Ltd., Japan 2001; Vol. JP 2001247723.

(139) Consiglio, R.; N.X. Randall; B. Bellaton; Stebut, J. v. *Thin Solid Films* **1998**, *332*, 151-156.

(140) Oliver, W. C.; Pharr, G. M. *J. Mater. Res.* **2004**, *19*, 3-20.

(141) Lee, C.; Wei, X.; Kysar, J. W.; Hone, J. *Science* **2008**, *321*, 385-388.

(142) Xiang, C.; Sue, H. J.; Chu, J.; Coleman, B. *J. Polym. Sci., Part B: Polym. Phys.* **2001**, *39*, 47-59.

(143) Maraschin, N. J.; Miller, R. C. *Modern Plastics* **1997**, *74*, 33.

(144) Chaffin, K. A.; Knutsen, J. S.; Brant, P.; Bates, F. S. *Science* **2000**, *288*, 2187-2190.

(145) Lo, C. T.; Laabs, F. C.; Narasimhan, B. *J. Polym. Sci.: Polym. Phys.* **2004**, *42*, 2667-2679.

(146) Zhu, W.; Zhang, X. Q.; Huang, B. T.; Feng, Z. L. *J. Appl. Polym. Sci.* **1995**, *58*, 515-521.

(147) Zhang, J.; Lodge, T. P.; Macosko, C. *J. Rheol.* **2006**, *50*, 41-57.

(148) Jablonski, E. L.; Gorga, R. E.; Narasimhan, B. *Polymer* **2003**, *44*, 729-741.

(149) Chaturvedi, U. K.; Steiner, U.; Zak, O.; Krausch, G.; Klein, J. *Phys. Rev. Lett.* **1989**, *63*, 616-619.

(150) McEvoy, R. L.; Krause, S. *Macromolecules* **1996**, *29*, 4258-4266.

(151) Lin, Y. J.; Poon, B. C.; Marchand, G. R.; Hiltner, A.; Baer, E. *Polym. Eng. Sci,* **2010**, *50*, 592-605.

(152) Lyu, S. P.; Cernohous, J. J.; Bates, F. S.; Macosko, C. W. *Macromolecules* **1999**, *32*, 106.

(153) Potschke, P.; Pionteck, J.; Stutz, H. *Polymer* **2002**, *43*, 6965-6972.

(154) Oyama, H. T.; Inoue, T. *Macromolecules* **2001**, *34*, 3331-3338.

Appendix

A. Copolymer Mass Conservation in the Two-Dimensional Interface

Here we derive the equations used to model the mass transport of copolymer compatibilizer chains created at the interfacial region during coextrusion. We assume that created copolymer chains remain at the interface but may diffuse or advect within the two-dimensional x-y plane at the interface. The mass conservation equation balances creation and transport, and in this two-dimensional plane it is given by

$$\nu = \nabla_{xy} \cdot (\mathbf{j}') . \qquad \text{(app.1)}$$

Here ν is the two-dimensional reaction rate (chains/s/m^2), ∇_{xy} is the gradient operator which operates only within the plane, $\nabla_{xy} \equiv d/dx + d/dy$, and $\mathbf{j}'$ is the rate of copolymer flux per unit length which occurs only within the x-y plane. The mass flux can be caused by advection or diffusion,

$$\mathbf{j}' = \mathbf{V}\Sigma - D\nabla_{xy}\Sigma \qquad \text{(app.2)}$$

where $\mathbf{V}$ is the velocity vector in the plane, $\mathbf{V} = (V_x, V_y)$, and D is the diffusivity. For our situation we can show that diffusion is negligible compared to advection by the flow.

The relative importance of advection to diffusion is determined by the Peclet number, which we estimate to be large, $\mathrm{Pe} = VL/D \approx 10^{13}$. This is estimated using a characteristic flow velocity $V \sim L/t$ with maximum contact time $t \sim 11.4$ s, process length $L \sim 14$ cm, and diffusivity $D \sim 10^{-12}$ cm^2/s .[71,74] Combining Equation (app.1) and (app.2) and neglecting diffusive flux gives the conservation expression,

$$\nu = V_x \frac{\partial \Sigma}{\partial x} + V_y \frac{\partial \Sigma}{\partial y} + \left(\frac{\partial V_x}{\partial x} + \frac{\partial V_y}{\partial y} \right) \Sigma \qquad \text{(app.3)}$$

which is a balance between creation and advection. Equation (app.3) is a first order partial differential equation with non-constant coefficients for the areal number density $\Sigma(x, y)$, which depends on the velocity field at the interface $\mathbf{V}(x, y)$ and the

reaction rate ν. We will derive a solution to Equation (app.3) under simplifying assumptions in order to calculate the number density Σ which results at the end of the coextrusion process.

For our estimate we assume plug flow (e.g. perfect slip at the bounding walls), for which the velocity in the flow direction is only a function of *x*, i.e. $V_x(x)$ throughout the entire volume. Consistent with plug flow, we further assume that copolymer density is also only a function of *x*, therefore $d\Sigma/dy = 0$. With the plug flow assumption we can relate the flow velocity V_x to the input flow rate Q by continuity,

$$V_x(x) = \frac{Q}{A(x)} \qquad \text{(app.4)}$$

where $A(x)$ is the local area. For our rectangular cross section $A(x) = H(x)W(x)$, where $H(x)$ is the bilayer thickness in the *z*-direction and $W(x)$ is the spanwise width in the *y*-direction. The parameters Q, $H(x)$, and $W(x)$ are known and therefore $V_x(x)$ and dV_x/dx can be calculated for use in Equation (app.3). As our final required input to Equation (app.3) we derive an expression for the stretching in the spanwise direction dV_y/dy. For plug flow, stretching in the *y*-direction is directly determined by the confinement in the *y*-direction $W(x)$. The interface length in the y-direction must always match $W(x)$, and is carried along by flow in the *x*-direction. Assuming a linear velocity profile of $V_y(y)$, with $V_y(y=0) = 0$, leads to the following expression

$$\frac{dV_y}{dy} = \frac{V_x}{W}\frac{dW}{dx} \qquad \text{(app.5)}$$

where each variable on the right hand side is a function of only *x*. Finally, we combine the plug flow velocity field results, Equation (aPPE.4) and (aPPE.5), with the conservation expression, Equation (aPPE.3), to yield a first order differential equation for the areal number density $\Sigma(x)$,

$$\frac{d\Sigma}{dx} - \frac{1}{H(x)}\frac{dH}{dx}\Sigma = \frac{v}{V_x(x)}. \qquad \text{(app.6)}$$

The coefficient in front of Σ results from dilation of interfacial area during coextrusion; this term equals zero when the interfacial area is kept constant, for which case the resulting number density $\Sigma(x)$ would be simply governed by the residence time $t_{res} = \int_0^x dx/V_x$. The full form of Equation (app.6), including the possibility of interfacial area dilation, can be solved analytically. The result is Equation (6) in the discussion section.

B. Damkohler Number Estimate

The Damkohler number, Da, effectively compares reaction rate to transport rate, defined here as

$$\text{Da} = \frac{\text{Reaction rate}}{\text{Diffusion rate}} = \frac{kC_\infty \lambda}{DC_\infty/\delta} = \frac{k\lambda\delta}{D}. \qquad \text{(app. 7)}$$

The reaction is diffusion limited for Da $\gg 1$ and reaction-limited for Da $\ll 1$. We estimate the range of Damkohler number from the range of possible parameter values. The reactive species are grafted onto polymer chains, and we therefore choose a diffusivity D which is representative of polymer-polymer diffusion, $D = 10^{-13} - 10^{-11}$ cm^2/s [71,74]. For the coexistence region thickness we consider the value $\lambda \approx 10$ nm. The reaction constant $k = 10^{-6}$ s^{-1} is taken from literature which measured the reaction between urethane and primary amine[48]. Our study involves secondary amine, which is observed to be a slower reaction[48], and therefore the value for k will be an upper bound (therefore an upper bound estimate of the Damkohler number). For the diffusion length we consider that the transient concentration boundary layer grows as $\delta(t) \sim \sqrt{Dt}$. Finally, for processing

time $t \approx 1-10$ s, and the range of diffusivity and $D = 10^{-13} - 10^{-11}$ cm^2/s, we calculate the range of diffusion lengthscale $\delta \approx 3-100$ nm.

For the given ranges of parameter values we calculate a minimum and maximum Damkohler number, with the result that $\mathrm{Da} \sim 10^{-9} - 10^{-4}$. Even the upper-bound estimate $\mathrm{Da} \sim 10^{-4}$ is very small, and we conclude that the process is reaction-rate limited. Reactive polymer interfaces have been shown to be reaction-limited for several other systems as well[68,69,154].

C. Calculation of deformation rates in coextrusion process

In Chapter 4, given extrusion die with changing rectangular cross section, with "slipping" plug flow (as in Song et al.[83]), we calculated

(a) Deformation rate tensor, **2D**, for the possible compression/extension in the coordinate directions;

(b) Deformation rate magnitude, $\dot{\gamma} = \left| II_{2D} \right|^{1/2}$, related to the second invariant of the deformation rate tensor.

Neglecting shear components, the deformation rate tensor takes the form

$$\mathbf{2D} = \begin{bmatrix} \dot{\varepsilon}_{xx} & 0 & 0 \\ 0 & \dot{\varepsilon}_{yy} & 0 \\ 0 & 0 & \dot{\varepsilon}_{zz} \end{bmatrix}.$$

Note that incompressible flow requires $\dot{\varepsilon}_{xx} + \dot{\varepsilon}_{yy} + \dot{\varepsilon}_{zz} = 0$, therefore we can re-write one of the components in terms of the others. It is most convenient to re-write the downstream component as $\dot{\varepsilon}_{xx} = -\dot{\varepsilon}_{yy} - \dot{\varepsilon}_{zz}$.

Therefore the deformation rate tensor can be rewritten as

$$\mathbf{2D} = \begin{bmatrix} -\dot{\varepsilon}_{yy} - \dot{\varepsilon}_{zz} & 0 & 0 \\ 0 & \dot{\varepsilon}_{yy} & 0 \\ 0 & 0 & \dot{\varepsilon}_{zz} \end{bmatrix}$$

and only two unknowns must be solved. The y- and z-direction deformation rates can be found following Song et al.[83] In the spanwise direction

$$\dot{\varepsilon}_{yy} = \frac{dV_y}{dy} = V_x\left(\frac{1}{W}\frac{dW}{dx}\right) = \frac{Q}{HW}\left(\frac{1}{W}\frac{dW}{dx}\right)$$

and in the direction normal to the interface

$$\dot{\varepsilon}_{zz} = \frac{dV_z}{dz} = V_x\left(\frac{1}{H}\frac{dH}{dx}\right) = \frac{Q}{HW}\left(\frac{1}{H}\frac{dH}{dx}\right).$$

To solve for the magnitude of the deformation rate tensor, $\dot{\gamma} = \left|II_{\mathbf{2D}}\right|^{1/2}$, we recall the definition of $II_{\mathbf{2D}}$ and

$$II_{\mathbf{2D}} = \frac{1}{2}\left[\left(tr\left[\mathbf{2D}\right]\right)^2 - tr\left(\left[\mathbf{2D}\right]^2\right)\right] = \dot{\varepsilon}_{xx}\dot{\varepsilon}_{yy} + \dot{\varepsilon}_{xx}\dot{\varepsilon}_{zz} + \dot{\varepsilon}_{yy}\dot{\varepsilon}_{zz}$$

Using the incompressibility result $\dot{\varepsilon}_{xx} = -\dot{\varepsilon}_{yy} - \dot{\varepsilon}_{zz}$ results in

$$II_{2D} = -\dot{\varepsilon}_{yy}^{\ 2} - \dot{\varepsilon}_{yy}\dot{\varepsilon}_{zz} - \dot{\varepsilon}_{zz}^{\ 2}$$

The results from above for $\dot{\varepsilon}_{yy}$ and $\dot{\varepsilon}_{zz}$ can be used to give the final result

$$\dot{\gamma} = \left|II_{2D}\right|^{1/2} = \frac{Q}{H(x)W(x)}\left|\left(\frac{1}{W(x)}\frac{dW}{dx}\right)^2 + \left(\frac{1}{H(x)}\frac{dH}{dx}\right)^2 + \left(\frac{1}{W(x)}\frac{dW}{dx}\right)\left(\frac{1}{H(x)}\frac{dH}{dx}\right)\right|^{1/2}$$

D. DSC and WAXS data for the cleaved surfaces of PE-MA and nylon 6

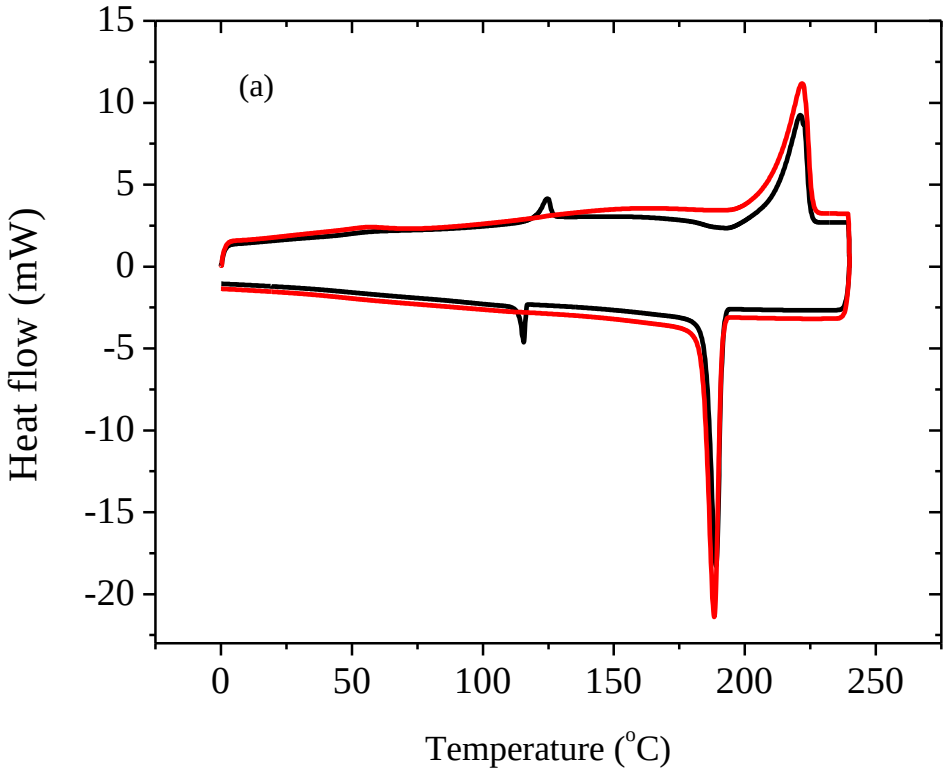

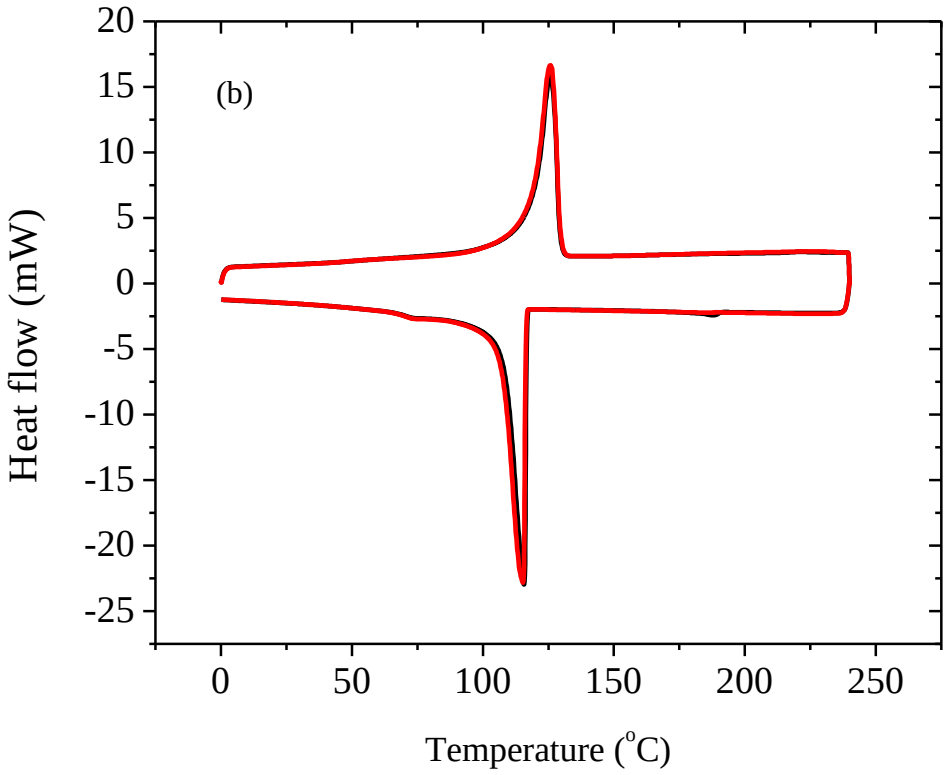

Figure app.1 DSC curves of cleaved bulk materials. (a) Nylon 6; (b) PE-MA. Black curves in each figure represents sample obtained from coextrusion at 230 ℃ using the compressive/stretching die with reaction time of 12 seconds. Red curves in each figure represents sample obtained from coextrusion at 230 ℃ using stretching die with reaction time of 12 seconds.

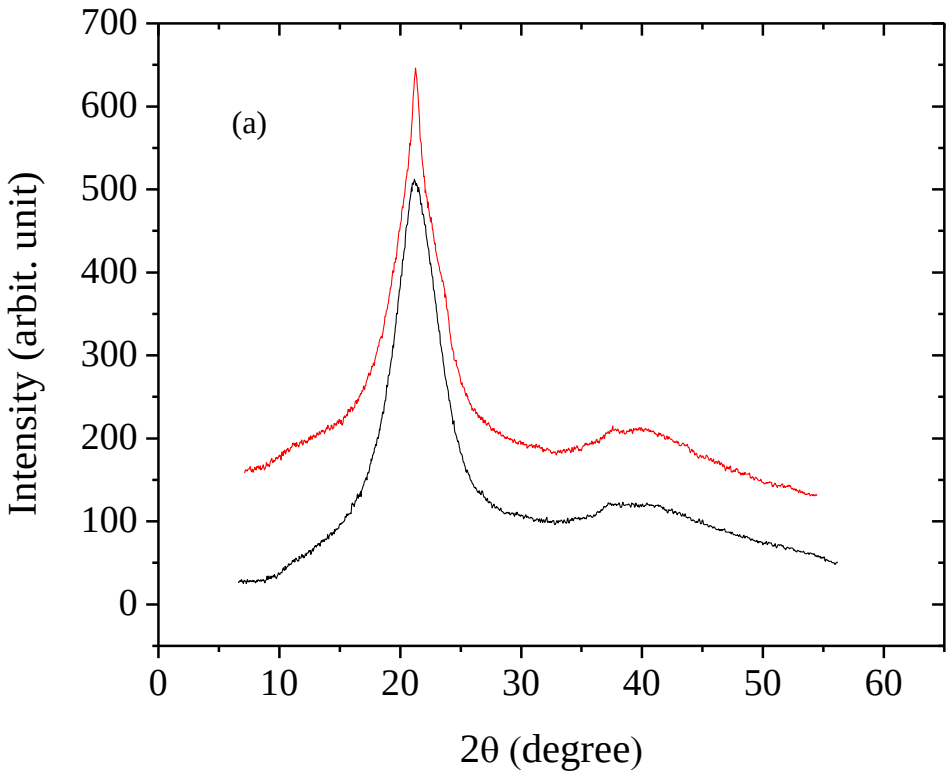
(a)
Intensity (arbit. unit)
2θ (degree)
0
100
200
300
400
500
600
700
0
10
20
30
40
50
60

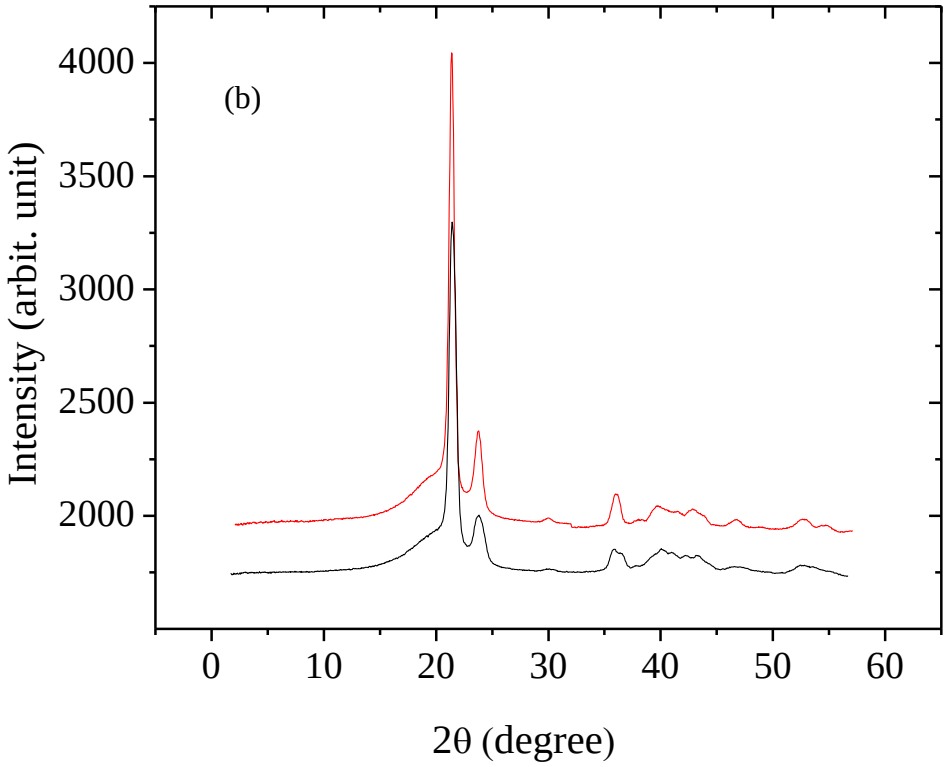

Figure app.2 Off-specular WAXS spectra with a 1 °incident angle. (a) Nylon 6; (b) PE-MA. Lower curves in each figure represent a sample obtained from coextrusion at 230 ℃ using the compressive/stretching die with reaction time of 12 seconds. Upper curves in each figure represent a sample obtained from coextrusion at 230 ℃ using stretching die with reaction time of 12 seconds.